Fall 10-2011

Self Assembly and Interface Chemistry of non-Metallated Tetraphenyl Porphyrin

Geoffrey Rojas

University of Nebraska-Lincoln, geoff.rojas@gmail.com

SELF ASSEMBLY AND INTERFACE CHEMISTRY OF NON-METALLATED
TETRAPHENYL PORPHYRIN

by

Geoffrey A. Rojas

A DISSERTATION

Presented to the Faculty of

The Graduate College at the University of Nebraska

In Partial Fulfilment of Requirements

For the Degree of Doctor of Philosophy

Major: Physics & Astronomy

Under the Supervision of Professor Axel Enders

Lincoln, Nebraska

October, 2011

SELF ASSEMBLY AND INTERFACE CHEMISTRY OF NON-METALLATED

TETRAPHENYL PORPHYRIN

Geoffrey A. Rojas, Ph. D.

University of Nebraska, 2011

Adviser: Professor Axel Enders

The study of the electronic properties and geometrical arrangement of 5, 10, 15, 20-tetraphenyl-21H, 23H-porphine on metal is presented. The systems were analyzed using both scanning tunneling microscopy and photoelectron spectroscopy and compared across surfaces to determine how the interface chemistry between the metal and molecule affect the self-assembly and band structure of the adsorbed species. The molecules are found to self-assemble and grow on the Ag(111) surface in a manner described by similar models to weakly bound metal/metal surface systems. The CH-π bonds between molecules are found to largely determine the relative inter-molecular arrangement, while the more isotropic van der Waals interactions drive the self-assembly. The 2H-TPP however remains isolated and equally dispersed despite any increases in coverage, observed motion, or annealing on the Cu(111) surface, indicating an electrostatic repulsion between adsorbates. Through calculation, spectroscopic observations of state shifts and mapping of the local work function, the limiting factor in the inter-molecular repulsion is found to be due to a combination of charge transfer between molecule and surface and perturbation of the surface electrons due to frontier orbital overlap. By comparing this molecule across surfaces and temperatures, the complex interplay between band structure matching, charge transfer, surface barriers, and self-assembly is described. Controlling the charge transferred to the adsorbed species by the underlying metal, these properties are tailored without changing the atomic constituents or general band structure of the adsorbed species.

ACKNOWLEDGMENTS

I would like to recognize the aid of my advisor, Professor Axel Enders. When I approached Axel three years ago about doing research with him, I was greeted with an excitement and enthusiasm I had never before seen regarding the subject of scientific investigation. Because of this, the following three years have been filled in both their frustrations and successes with the same love for science I had as child.

Many thanks to Professor Paul Bagus for his correspondance with regards to his coffee-cup model of adsorption and anti-symmetrization of closed-shell systems. Also, much thanks also to Hector Vázquez for his discussion regarding the weak chemisorption and gap states of the TPP/Cu hybrid system.

Also to Christian Binek for suggesting the collaboration which led to this work. I extend a great thanks to the many collaborators that helped in this study of surface adsorbate systems, Matthias Bode, Wonyoung Choe, Peter Dowben, Yi Gao, Scott Simpson, Eva Zurek, JiHyun Kim, JaeSung Kim and Sabrina Hennes (Hoffmann). In addition, to my coworkers and labmates Cameron Bravo, Donna Kunkel, Justin Nitz, Mark Plano-Clark and of course, Xumin Chen, for all the effort they put into the operations of our laboratory in the pursuit of these projects, I am indebted to you. Especially Xumin, thank you for the many late nights spent in the assembly, testing, and familiarization of our UHV system.

Contents

List of Figures

List of Tables

List of Symbols and Abbreviations

Abbreviation	Description	Definition
Ag(111)	Silver surface along the $\langle 111 \rangle$ direction	page 74
Au(111)	Gold surface along the $\langle 111 \rangle$ direction	page 74
COOH	carboxylic acid	page 41
Cu(111)	Copper surface along the $\langle 111 \rangle$ direction	page 74
DFT	Density Functional Theory	page 75
DOS	Density of States	page 30
E_A	Activation energy	page 48
E_{ad}	Adsorption energy	page 27
E_{CNL}	Charge Neutrality Level	page 30
E_F	Fermi energy	page 28
E_V	Vacuum energy level	page 28
HOMO	Highest Occupied Molecular Orbital	page 29
HOPG	Highly Ordered Pyrolitic Graphite	page 38
IDIS	Induced Density of Intereface States	page 35
IETS	Inelastic Tunneling Spectroscopy	page 17
IPES	Inverse Photoelectron Spectroscopy	page 25
I_T	Tunneling current	page 13
LN2	Liquid Nitrogen	page 7
LUMO	Lowest Unoccupied Molecular Orbital	page 29

Abbreviation	Description	Definition
LT-STM	Low-Temperature Scanning Tunneling Microscopy	page 7
MIGS	Metal Induced Gap States	page 35
MOCN	Metal-organic coordination network	page 44
PES	Photoelectron Spectroscopy	page 22
SAM	Self Assembled Monolayer	page 46
STM	Scanning Tunneling Microscopy	page 10
STS	Scanning Tunneling Spectroscopy	page 14
TBPP	5, 10, 15, 20-tetra(3,5-di-tert-butylphenyl) porphyrin	page 53
TCPP	5, 10, 15, 20-tetra carboxyphenyl porphyrin	page 38
TPP	*meso* 5, 10, 15, 20-tetraphenyl porphine	page 15
2H-TPP	5, 10, 15, 20-tetraphenyl-21 H, 23 H-porphyrin	page 74
M-TPP	metal (M) 5, 10, 15, 20-tetraphenyl porphyrin	page 52
TPyP	5, 10, 15, 20-tetrapyridyl porphyrin	page 53
UHV	Ultra High Vacuum	page 5
UPS	Ultraviolet Photoelectron Spectroscopy	page 22
vdW	van der Waals interaction	page 39
Φ	Work Function	page 29

Isolated material particles are abstractions, their properties being definable and observable only through their interaction with other systems.

Niels Bohr

Chapter 1

Introduction

The use of metal/organic systems has exploded over the past twenty years into a wide variety of applications including, organic diodes and OLEDs [1], photovoltaic cells [2, 3], field effect transistors [4], magnets [5, 6], and hydrogen storage [7]. This is because the discrete energy levels of organic molecules are similar to the band structure of semi-conductors [8]. However, unlike semi-conductors, the properties are inherent to the individual, closed-shell molecules, not the bulk material. This allows much more tailorability of semi-conductor properties through control of the structure and interactions of the molecules in question.

This tailorability is not limited to the molecule itself, but also to the underlying electrode surface. Improper band structure matching [9], surface dipoles [10], and hybridization of states [11] are key parameters affecting charge exchange at the interface. These can be used as additional control parameters to achieve the desired device design.

The degree of disorder in the organic system is commensurate with the semi-conductor-like charge transport properties of the device [12]. With greater disorder, the charge transport mechanism functions less according to a band structure model and more as charge hopping between molecules in a gas [13]. This allows tunable band structures through control of the supramolecular ordering.

It is for these reasons that so much work in surface science has been devoted to understanding how the metal/organic interface affects the band structure and self-assembly of organic thin films. Only by understanding these topics may techniques be designed to bypass or control them. One fact that has become clear during this study is that while the application of certain descriptions of metal/semiconductor interfaces can be applied to specific metal/organic interfaces [1], these models are not generally applicable to all systems [14]. There is at present a lack of understanding of the mechanics and chemistry of the weak metal/organic interface, and how this affects the aforementioned properties.

It is the goal of this dissertation to advance the understanding of this problem through the local probe analysis of the metal/organic interfaces of a specific key species of molecule, 5, 10, 15, 20-tetraphenyl porphyrin (TPP), and in so doing present unique techniques for the control of the dynamics of the organic adlayer. Using the unique capabilities of scanning tunneling microscopy (STM) over a varying set of metal surfaces, the basic interactions at the metal/organic interface and how these interfere with the self-assembly and electronic states of weakly bound molecules are illustrated and discussed.

As STM is a local probe measurement technique, this allows for the simultaneous measurement of the electronic properties in correlation with the geometric location on the adsorbed molecule and surrounding metal surface. This is the most direct comparison that can be made between experimental results and theoretical predictions. Through work function measurements not only can the shift in the work function of the adsorbed system be determined, but the direction of electron transfer within the different components of the molecule as well [15]. The use of local-probe spectroscopic techniques finds differences between the adsorbed molecules depending on surface, but through comparison with the integral probe techniques of photoemission spectroscopy, it is shown that none of these interactions are indicative of a covalent bond with the surfaces, and that the molecules may be considered in all cases weakly bound. Based on this, the heretofore debated mechanisms of the molecular phyisorption and how it affects self-assembly are described.

This dissertation is organized as follows. An outline of the experimental systems used to grow and evaluate the thin films studied is presented in chapter 2. Here, the theoretical basis underlying scanning tunneling microscopy (STM), ultraviolet photoemission spectroscopy (UPS), as well as the design and facilities of the equipment used are explained. Chapter 3 provides an introduction to the relevant physical interactions taking place at the metal/organic interface. This includes an overview of the both inter-molecular and molecule-surface bonds of similar organic molecules, along with a hierarchy of the energetic contributions of each bond.

In chapter 4 are three published and to-be-published articles discussing 2H-TPP self-assembly, and how it can be controlled through the molecule-surface interaction. This is presented along with a brief background to the recent advances made in the study of this, and similar molecules, on metal surfaces. Comparison of the mechanics of the self-assembly of 2H-TPP on Ag(111) to similar growth studies of metal/metal systems shows that the growth dynamics of organic adsorbates follow the same physical mechanisms as inorganic systems. These studies also provide an estimate for the inter-molecular bond for comparison with theoretical predictions. By then comparing the same molecule across metal surfaces, it is determined that the molecule strongly interacts with the Cu(111) surface in a manner not present on Ag(111). It is this interaction which limits self-assembly, and is explained through the local probe of individual molecules and application of Ag buffer layers to the more strongly binding Cu(111) surface. The interaction is found due to a combination of interface state and repulsion of surface electrons, in accordance with modern theory by certain authors.

Through this comprehensive analysis, it is shown that the factor limiting the self-assembly of these structures over free terraces is not only electron transfer between the molecule and the underlying metal, but restructuring of surface electrons. This is in accordance with the modern theory presented by certain authors for physisorption of organic species on metal surfaces: a combination of interface state and repulsion of surface electrons. Both create electrostatic barriers which prevent the molecule-molecule interactions driving self-assembly. By therefore controlling the charge

transfer, it is possible to prevent any electrostatic repulsion between adsorbates and control the self-organization of the adsorbed species.

Chapter 2

Experimental

2.1 Experimental setup and sample preparation

Sample preparation and experiments were performed in a two-chamber ultra high vacuum (UHV) system at base pressure $< 10^{-10}$ Torr. One chamber housing an Omicron LT-STM (Chapter 2.1.2), and one chamber containing the equipment for sample preparation (Chapter 2.1.1), Figure 2.1.

2.1.1 Molecular Evaporator

The sub-nanometer organic films used in this study were produced through controlled submonolayer deposition using a homebuilt evaporator. Due to the low partial pressure and sharp thermal range of evaporation for organic molecules, the construction of this heater was based on the contact heating of removable crucibles by wrapped filament wire as used in Knudsen cell based thermal evaporators.

The design is as follows. A copper cooling plate holds a group of four thermally isolated and individually heated crucible holders, Figure 2.2 (a) i. The holders rest atop stainless mountings electrically isolated from the cooling plate and are held in place by removable bolts. The holders
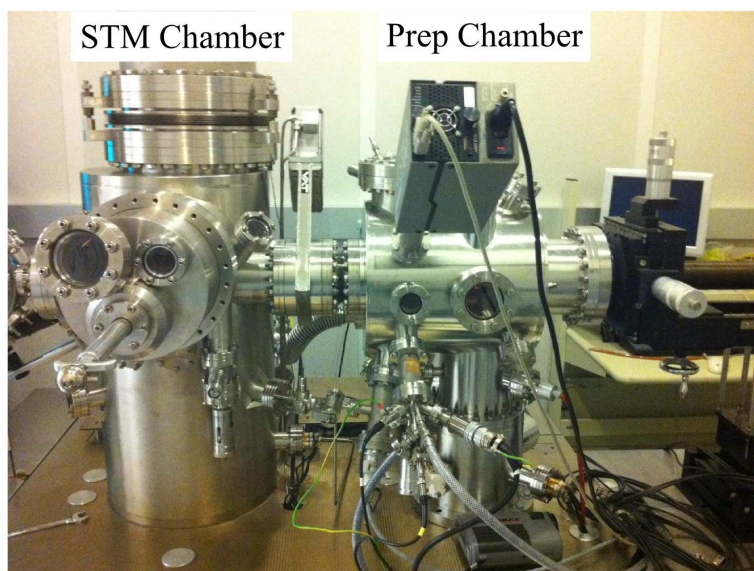
Figure 2.1: UHV chambers containing measurement systems: STM chamber and prep chamber

are each separated from one another by a copper curtain that is held in thermal contact with the copper base plate, ii. This curtain limits radiative heating between holders as well as evaporation of material from one crucible to the other. The holders are composed of two ceramic sheaths tightly binding a tantalum wire (red), iii. The tight wrapping distributes the heat from the wires evenly across the surface of the sheaths, within which a tightly fitting, removable quartz crucible (green) is inserted, iv. A hole is placed in the center of the stainless steel mountings and a small type-K thermocouple is left in contact with the bottom of the crucibles. By running a current through the wires, this heats the crucibles and allows a controlled evaporation of organic material.

The full set-up is illustrated in Figure 2.2 (b). The pressure of the heated matrial is controlled by running water through two cooling tubes, v, and cooling the plate upon which the evaporator head (a) is mounted. This allows for a stable, constant temperature to within ∼1 K of the evaporation temperature. The evaporation of the material from the crucibles onto the sample surface is then started/stopped using a simple stainless steel shutter, vi, over the holes in a copper sleeve that surrounds the evaporator head. The heating wires, thermocouples and shutter control are attached

to stainless steel feedthroughs.

The design provides surprising thermal isolation. Temperatures of individual crucibles not in use rarely grows by any more than 20 K during heating. Using this setup, the quartz crucibles are easily removed, cleaned, and replaced in a matter of minutes following removal of the evaporator. This ease of use combined with the fact that the crucibles can each hold ∼50 mg of porphyrin compounds provides a robust and flexible system for easy sample preparation.

Using this together with a quartz crystal microbalance, molecules of 5, 10, 15, 20-tetraphenyl-20, H 21, H-porphyrin (2H-TPP), various species of metallated TPP (M-TPP), and 5, 10, 15, 20-tetra carboxyphenyl-20, H 21, H-porphyrin (TCPP) were deposited on surfaces at controllable rates typically < 0.1 ML min^{-1}.

2.1.2   Scanning Tunneling Microscope

The STM used in these studies is a low-temperature scanning tunneling microscope (LT-STM) manufactured according to specifications by Omicron Nanotechnology. The machine operates in a temperature range from 2.6 K - 300 K within magnetic fields and is usable with z-stability in topographic images as low as 1 pm. The cooling of the system allows for temperature control of the scanning probe tip as well as the sample, thereby both lowering the thermal noise of the tip to below the electric noise expected in spectroscopic signals at very low temperature (< 10 K) and limiting thermal diffusion of tip atoms which creates more stable signals across measurements. The cryostat is able to hold temperatures without refilling for 50 hours to obtain these measurements, making the machine ideal for long-term sample measurements without perturbation of the sample in question.

The basic design of the machine is as follows. The STM sample stage sits under a large bath cryostat containing two separate dewars, Figure 2.3 (i). The outer dewar, the LN2 dewar, is filled with liquid nitrogen (LN2) for cooling both the system and the inner dewar, the LHe dewar, which
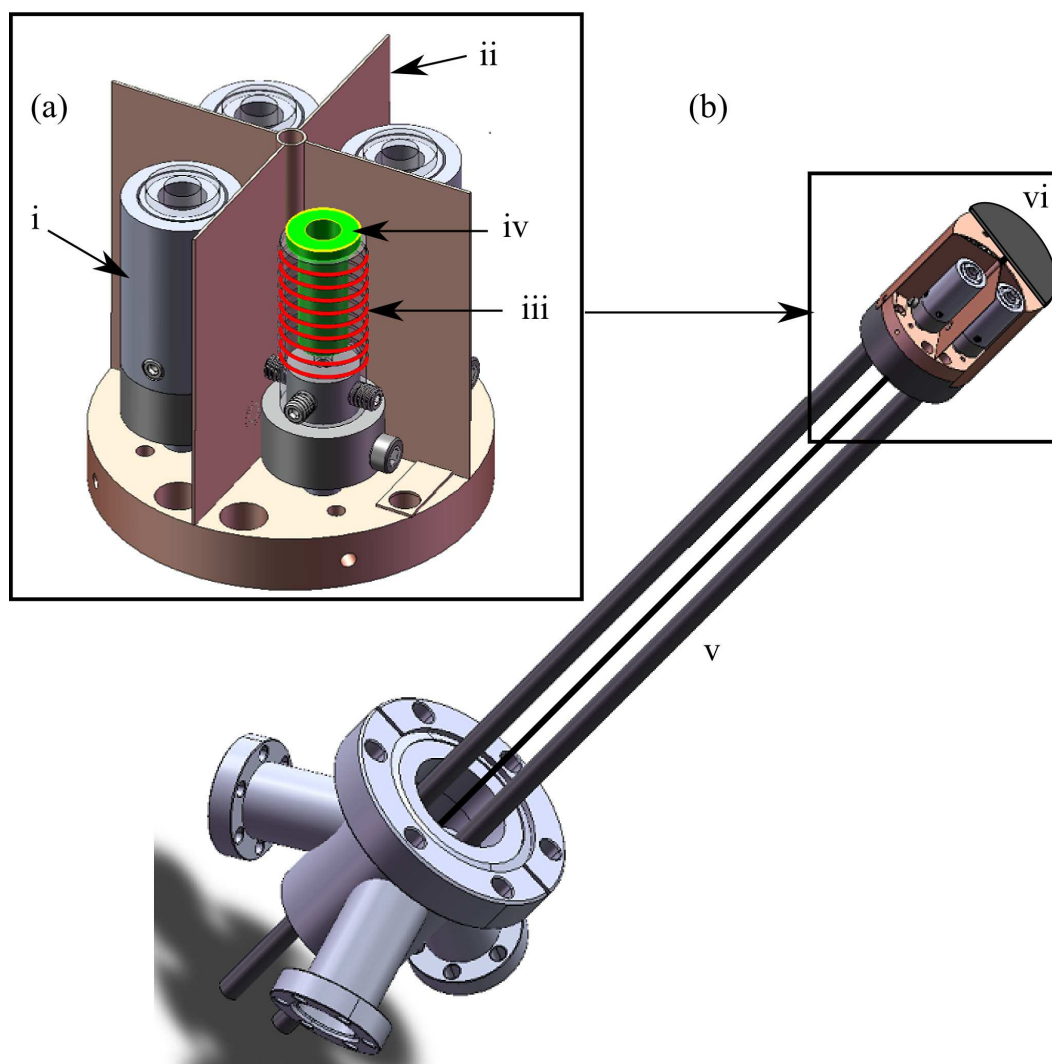
Figure 2.2: (a) Evaporation head includes crucibles and heating equipment: ceramic heating sheath (i), thermal isolation curtain (ii), heating wires (red) (iii), and replaceable quartz crucibles (iv). (b) Complete evaporator with water cooling lines (v) and shutter (vi).

can be filled with LN2 or liquid helium (LHe). The LHe cryostat is the dewar in direct thermal contact with the otherwise isolated sample stage. For purposes of this dissertation, temperatures on the order of 5 K were generally unnecessary and measurements were therefore conducted filling both cryostat dewars with LN2, resulting in temperatures of 80 K unless otherwise specified.

The sample stage is held in contact with the LHe cryostat by three suspension springs. These lower the stage, holding it in minimal contact with the cryostat and surrounding system, thereby

reducing thermal loss as well as noise due to mechanical vibrations Figure 2.3 (ii). The sample rests face-down in a sample holder, with the scanning probe tip underneath, (iii - iv). The tip is positioned laterally under the relevant area of interest of the sample by two $\hat{x}$ and $\hat{y}$ piezo crystals, (v). The piezos both have a range of ~ 5 mm. Noise due to vibrations of the UHV systems are further reduced using an eddy current dampening system between the sample stage, shown in Figure 2.3 (vi), and the surrounding shield (not shown).
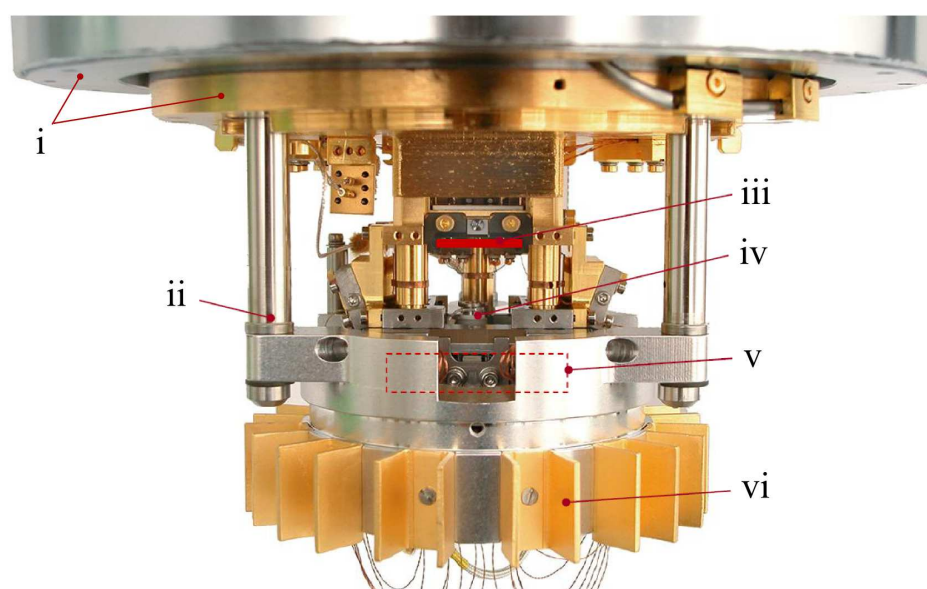
Figure 2.3: Side-view of the Omicron LT-STM sample stage. (i) LN2 bath cryostat (silver) and LHe bath cryostat (gold) (ii) suspension springs holding up (iii) side-view of sample holder (iv) tip mounting (v) $\hat{x}$, $\hat{y}$ piezo coarse motion drive (vi) eddy current dampeners.

The sample stage is illustrated in further detail in Figure 2.4 (a). It rests face-down with the tip underneath. This helps prevent the tip from crashing into the surface due to slippage or sudden shifts. A small aperture is positioned right below the sample plate to allow for the *in situ* deposition of sample materials onto the surface of the plate. The tip rests on a cylindrical piezo crystal which moves the tip normal to the sample in $\hat{z}$ with a range of motion of 10 mm, (b). The lateral coarse motion piezos are shown below.

(a)

(b)

Sample

Tip

Optical
Window

Tip

Z Piezo
Drive

XY Piezo Drive

Viewing
Lens

Evaporator
Window
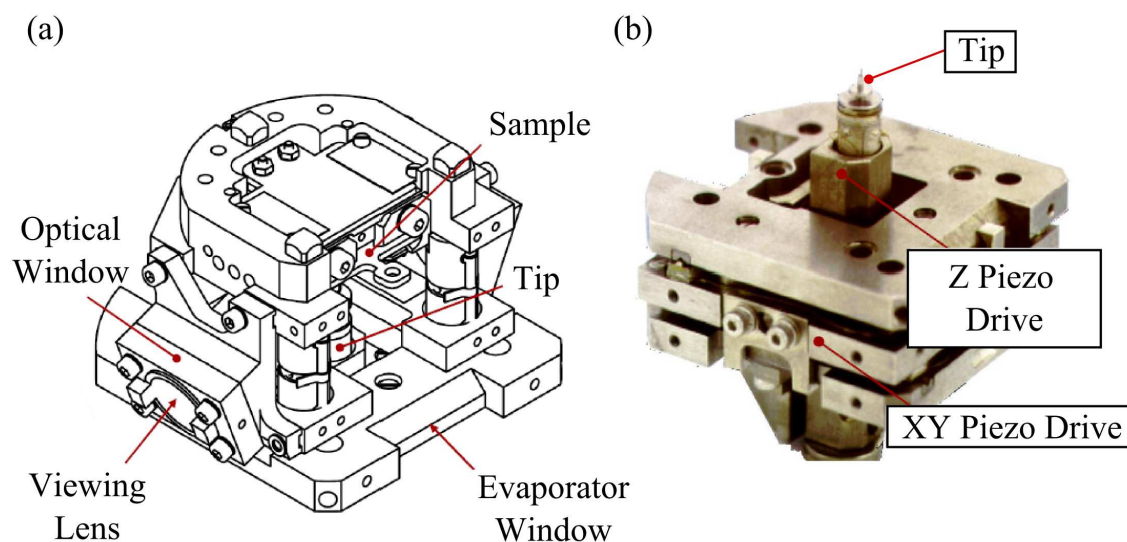
Figure 2.4: (a) A schematic of the sample stage. (b) Tip component showing the two sets of coarse motion piezo drives along with tunneling tip.

2.2   Scanning Tunneling Microscopy

Scanning tunneling microscopy (STM), the techniques upon which most of the following work is based, is an extraordinarily powerful tool for measurement of the electronic structure of conducting, semi-conducting and even insulating [16] surfaces near the Fermi energy. The beauty of the technique is not simply in the ability to measure such systems, it is in the ability to measure them *locally*, on length scales < 1 Å. This allows for the relation of morphological features with spectroscopic states [17, 18], surface states [19], the vibrational states of molecular adsorbates [20], surface potential [21, 22, 23], as well as electron spin [24]. These measurement techniques will be reviewed to provide a more detailed understanding of the STM and the measurements performed for the clarity of the reader.

2.2.1 Scanning tunneling microscopy/spectroscopy

The fundamental principle underlying this technique is quantum tunneling: the passage of a particle, such as an electron, through a barrier of larger energy than that of the particle [25]. This is used by moving a sharp metal tip close to a conducting surface through the use of a well-controlled coarse motion drive, using a piezo crystal. The tip is initially approached using a current measuring feedback loop. Wherein, a bias potential is applied between the tip and metal surface and the the tip is then approached in a step-wise fashion as the current is measured at each small decrease in the distance between the tip and the sample. When a noticeable increase is observed, the motion is halted and the tip is at scanning position with the surface. The tip is then retracted or approached in $\hat{z}$ using this same feedback loop on a nanometer scale by a second set of piezos which are used for the control of the normal motion during measurement [26, 27].

As the tip is then scanned across the surface encountering defects, adsorbates, step-edges and other surface features, it is moved up and down in $\hat{z}$ in order that the measured current is kept constant. As the changes in the z-signal of the piezo (Δz) are measured, this creates a topological map of the surface of interest, Figure 2.5. With appropriately sharp tips, atomic-scale images are obtainable, such as this sample image of a 9 nm $\times$ 9 nm Ag(111) surface, Figure 2.6.
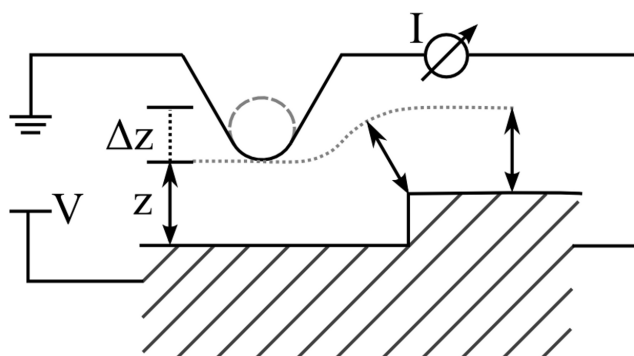
Figure 2.5: The tip is brought some distance z away from the surface, producing a current I for a given potential V applied across the sample. As the tip is scanned across the surface, the tip must approach or retract by Δz to keep I constant.
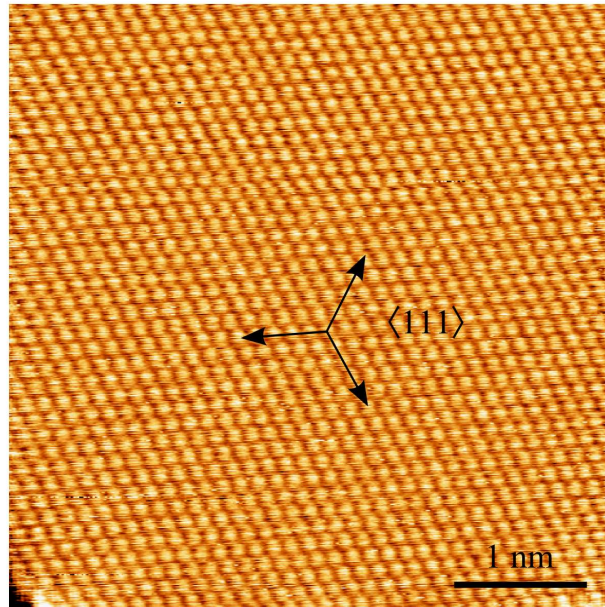
Figure 2.6: 9 nm × 9 nm STM image of Ag surface taken in our lab showing atomic structure along the ⟨111⟩ surface.

2.2.2 Scanning tunneling spectroscopy

The key difference between scanning tunneling microscopy and other low-dimensional microscopy techniques such as atomic force microscopy or transmission electron microscopy is the potential for spatially resolved spectroscopy. In STM, the measured quantity is the electronic states of the system being examined. The tip is neither interacting through direct electrostatic forces as with AFM, nor measuring the passage of wavelengths around geometric barriers such as electron microscopy. Rather, the current passing between sample and tip is composed of electrons in one bound energy state (sample) tunneling into other available energy states (tip). As the probe measures the local enviornments, these currents change can be related to these environments. Through examining specific changes in the currents between the tip and sample, spectroscopic information of the electronic states of the sample can be gained.

For two systems separated by vacuum, bound electrons tunnel from occupied states of one

material into unoccupied states of the other. Here, the potential barrier the electrons are tunneling through is the binding energy of the electrons to material, the workfunction Φ. Due to the Pauli exclusion principle, they may only tunnel from occupied states of one electrode (tip or sample) into unoccupied states of the other. For conductors, these occupied states are energy states of $E < E_F$. For closed-shell molecules, these are occupied molecular orbitals.

With no bias voltage V applied across the tip-sample junction, the fermi energies align, and there is no net current, Figure 2.7 (a). Upon the activation of an electric potential over the tip however, the energy levels of (b) are shifted by eV, (b). This creates a change in the relative Fermi distributions and allows electrons of energy $E > E_F - eV$ to tunnel into the unoccupied states of the tip. In the case of organic molecules on the other hand, the energy levels are not continuous, but discrete, Figure 2.7 (c). This means tunneling is allowed only at energies equal to the discrete energy levels of the system.

The tunneling of electrons between the electrodes constitutes the tunneling current, I_T. This current is expressed simply as the integral of the distribution of electronic states over the energy range $E_F - eV \leq E \leq E_F$, Equation 2.1 [28].
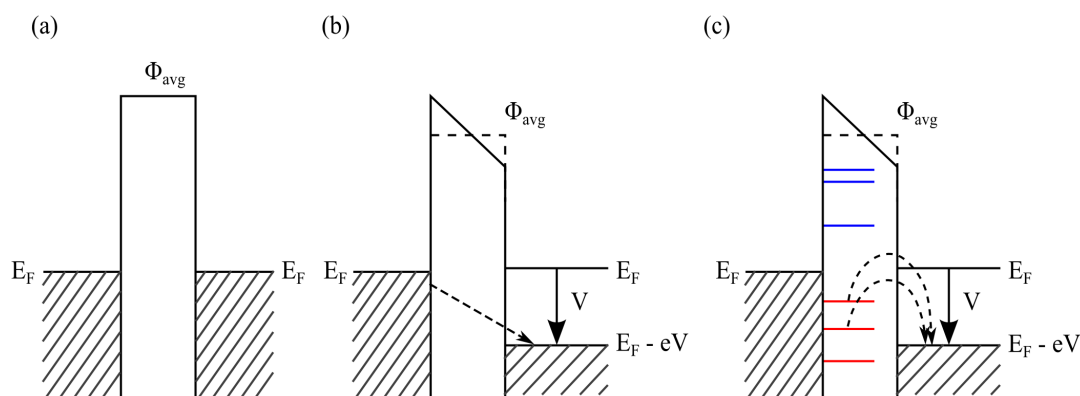
Figure 2.7: (a) E_F of the metal surface (left hand side) and the metal tip (right hand side) are at equal level with no potential. (b) With V applied across the gap, the apparent Fermi level of the tip is lowered to $E_F - eV$, allowing tunneling from sample to tip. (c) Organic adsorbate or semiconductor with the unoccupied (blue) and occupied (red) orbitals allow tunneling from discrete occupied states into tip. See text for explanation.

$$I_T = \frac{2\pi}{m^2} \int_{E_F}^{eV} d\varepsilon |M|^2 \rho_1(\varepsilon)\rho_2(\varepsilon - eV)[f_1(\varepsilon) - f_2(\varepsilon - eV)], \tag{2.1}$$

where here, we are taking the two workfunctions to a be the same between materials, Φ_{avg}. $|M|^2$, $\rho(\varepsilon)$, and $f(\varepsilon)$ are the tunneling matrix, the densities of states (DOS), and the Fermi-Dirac distributions respectively [28]. $\rho(\varepsilon)$ provides a description of the available energies of electronic states, while $f(\varepsilon)$ is the occupation of those states. The tunneling matrix is the overlap of the wavefunctions of the sample and the tip in the tunneling regime ($E_F > E > E_F - eV$) [29]. This remains generally stable over energies near E_F, and as such is taken as a constant of integration in energy [30].

Then, for relatively low temperatures the Fermi distribution can be approximated as a step function, and Equation 2.1 becomes,

$$I \propto \int_{E_F}^{eV} d\varepsilon \rho_1(\varepsilon)\rho_2(\varepsilon - eV) \tag{2.2}$$

This is the well known known Tersoff-Hamann approximation [31] for the tunneling current. In this description, the tunneling current is proportional simply to the integration over energy of the convolution of the DOS of tip and sample. The key here is that the current is dependent *only* on the DOS of the tip and the sample. Therefore, through the derivative of I_T in V we have a direct measure of the DOS [32, 33],

$$\frac{\partial I_T}{\partial V} \propto \rho_1(\varepsilon)\rho_2(\varepsilon - eV) \tag{2.3}$$

In the case where the tip DOS is approximately constant across the energy range of interest, a quite common phenomenon, any variations in dI_T/dV can be attributed to the sample DOS [30, 31, 34]. This is accomplished through conditioning of the tip to provide a flat DOS near E_F [35]. This provides the amazing tool of STM: scanning tunneling spectroscopy (STS) [32, 36, 18, 17].

By properly measuring the variation of V in I_T, we can achieve a measurement of the sample DOS on an local, atomic scale!

This is achieved through two methods: a differential analysis of an $I_T(V)$ curve or, more commonly, a direct measurement of dI_T/dV. For the latter, the current I_T is measured at a given bias voltage V, the bias voltage is modulated by a small AC current resulting in a change in V (ΔV, typically on the order of 20 meV at a few kHz). The responding variation in I_T (ΔI_T) is the derivative of the $I(V)$ signal and measured as the bias voltage is scanned across the energy range of interest. The energetic states of the sample are then measured, as seen in Figure 2.8. Here a dI_T/dV curve is taken over a Ag(111) surface in the energy range of -600 meV to +200 meV below and above E_F respectively. The surface state of the Ag(111) surface is clearly distinguished at -80 meV.
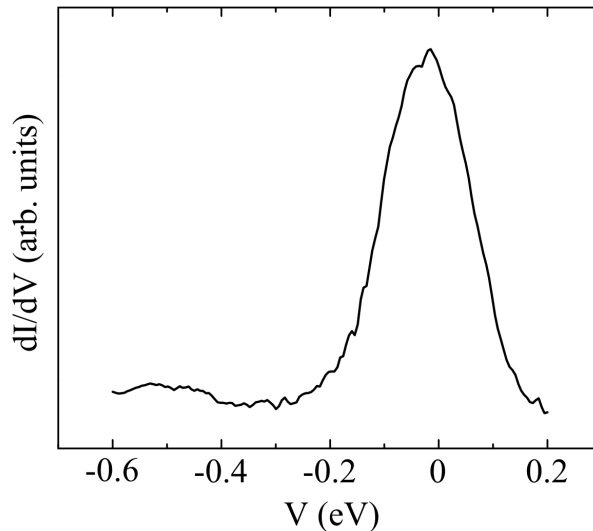
Figure 2.8: Example of voltage dependent point spectra of the Ag(111) surface. Ag(111) surface state is clearly visible near -0.08 eV below E_F.

By taking these measurements at a given bias voltage while scanning over the sample, it is possible to map the DOS at a given energy and compare between different features or adsorbates. An example is provided in Figure 2.9. A molecule of *meso*-tetraphenyl porphine (TPP) is adsorbed on the surface of a Cu(111) single crystal and the dI_T/dV map is shown over a range of voltages

between -400 meV and 400 meV relative to E_F. The symmetry of the DOS of the molecules changes between energy levels as well as the wavelength of the surface state of the Cu(111) (seen scattering around the adsorbed molecule).
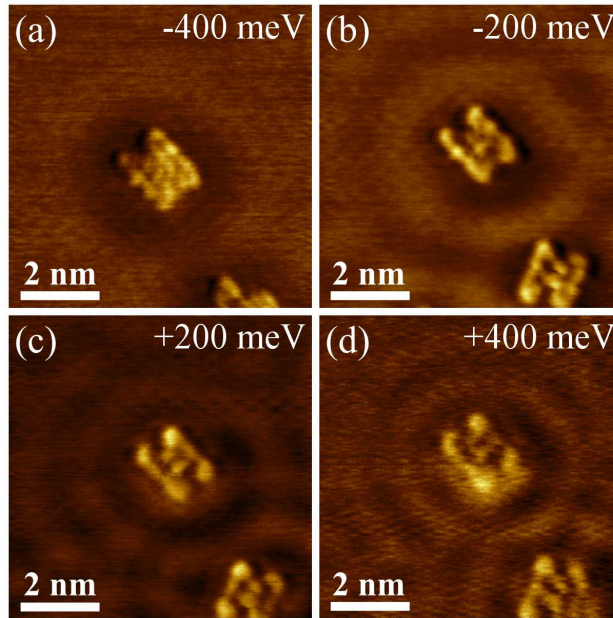
Figure 2.9: dI_T/dV map of 2H-TPP/Cu(111) taken at (a) -400 meV, (b) -200 meV, (c) +200 meV, and (d) +400 meV relative to E_F showing the different molecular DOS and surface state wavevector of the Cu(111) surface.

Exciting as this is, there are a number of limitations to this measurement technique that need be kept in mind. Most obvious here is the peak broadening observed in the spectra. This is due first to the previous approximation of the fermi distribution being flat in temperature. In reality, it is not and the thermal excitation creates a weak broadening of $I_T(V)$ in temperature of approximately 3.5 $k_B T$ [37]. Here, this would be 24 meV as the measurement temperature was 80 K. The second broadening effect, is due to the modulation of ΔV by the lock-in amplifier and is given as approximately 1.7 times the modulation voltage of the amplifier [38]. So the overall energy resolution at 80 K is typically on the order of 50 meV. Furthermore, while the above estimations assume a relatively flat tip DOS, simple tip irregularities can create DOS peaks relatively close to

E_F due to adsorption of surface molecules, geometric reconstructions, electronic resonance states and more [39, 35]. Many of these in fact overlap known states, changing the appearance of the spectra. By intentionally transferring single adatoms or molecules such as CO to the STM tip however, this creates a significant overlap in DOS with those same adsorbed species, allowing increased contrast and image resolution between the species of interest in scans over multiple adsorbates [40, 41].

This is all general enough that it extends to any measured sample: metal, semiconductor or organic. However, it was discovered by Hansma in 1966 that this spectroscopic mapping extended not only to the electronic states of the sample, but to the *vibrational modes* of adsorbed molecules as well [42]. The tunneling electrons can excite vibrational modes of energy $h\nu$ in molecules situated within the tunneling gap, thereby losing energy and tunneling into states of reduced energy $E = eV - h\nu$, Figure 2.9 [42].

This is what is known as inelastic tunneling spectroscopy (IETS) Electrons at energy $eV > h\nu$ therefore can tunnel into two states

$$E = \begin{cases} eV \\ eV - h\nu \end{cases} \tag{2.4}$$

What results is a greater net tunneling at higher energies and an increase in the conductance of the sample represented by a sharp peak in the $d^2 I_T / dV^2$ slopes [43, 44].

This measurement technique had previously been used with tunneling bridge systems to measure the vibrational modes of molecules [20]. When done using STM, the Å scale lateral resolution allows the probing of vibrational modes and what effects the surrounding environment has on them [43].
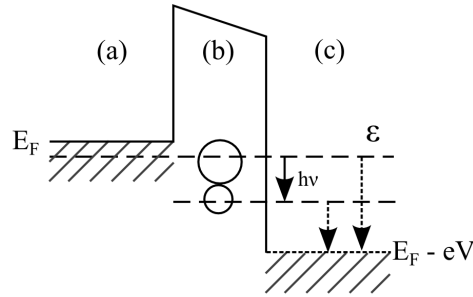
Figure 2.10: As with a typical tunneling setup, electrons tunnel from the conductor (a) into molecule adsorbed on the surface (b). The tunneling excites a vibrational mode of energy $h\nu$, resulting in an energy loss as the electrons tunnel into the underlying metal surface with a lowered energy (c).

2.2.3 Workfunction/Barrier Height

While Equation 2.3 provides an excellent approximate description to the variation of I_T in energy, the dependence of the current on the tip-sample separation is entirely determined by the prefactor $|M|^2$, which is generally taken to be constant over small eV near E_F. Then for a constant V and assuming a simple one-dimensional model of tunneling, the current was initially estimated by Binnig and Rohrer to vary with separation z as [26, 27],

$$I_T \propto e^{-2kz} \tag{2.5}$$

$$k = \sqrt{\frac{2m(\Phi)}{\hbar^2}}$$

This was done by extending Frenkel's model (Equation 2.1) to the approximation of two identical conductors at very low bias with no geometric variation. While the expansion of $|M|^2$ and its constancy in z is still a matter of discussion, a model taking the geometry of the tip and DOS of the system into account generally finds the very same dependency [31]. In fact, in the energy range near E_F, geometric considerations can be somewhat ignored in z and all models can be generally

written as [28, 29, 45, 34],

$$I = \frac{\hbar e}{2m} D_{tip}(E_F) V G(R) e^{-2kz} \tag{2.6}$$

Here D_{tip} and $G(R)$ are the DOS per unit volume of the tip and the geometrical factor over the surface describing the tip. Both of these are considered constant in ε and z only in the low energy range where $I_T \propto V$.

$$ln(I_T) = ln(C_0) - 2kz, \tag{2.7}$$

$$C_0 = \frac{\hbar e}{2m} D_{tip}(E_F) V G(R),$$

and from this, by taking the differential of I in z,

$$\frac{\partial ln(I_T)}{\partial z} = -2 \frac{\sqrt{2m}}{\hbar} (\phi)^{-1/2} \tag{2.8}$$

The key is that this provides an approximation for the workfunction Φ. An example is shown in Figure 2.11. In (a) we see a measurement of the current over both the clean Cu(111) surface (black) and TPP molecule (red). By taking $\ln I_T$, as in Equation 2.8, we find estimates for Φ showing a decrease in the workfunction over the molecule.

Though this is an approximation in the low-energy regime, the benefit to Equation 2.8 is the linearity of I in V. The energetic bounds of the approximation are determined by the linearity of a simple $I_T(V)$ curve, as shown for an $I_T(V)$ curve over Ag(111) in Figure 2.12. Outside the highlighted region, $I_T(V)$ does not have linear shape. This is because the approximations used above all assume very low energy of tunneling electrons, near E_F [28, 31]. As E increases significantly, the DOS of the same no longer remains constant and the approximations made in Equation 2.6 are no longer valid. This causes relationship between I_T and V becomes nonlinear

(a)
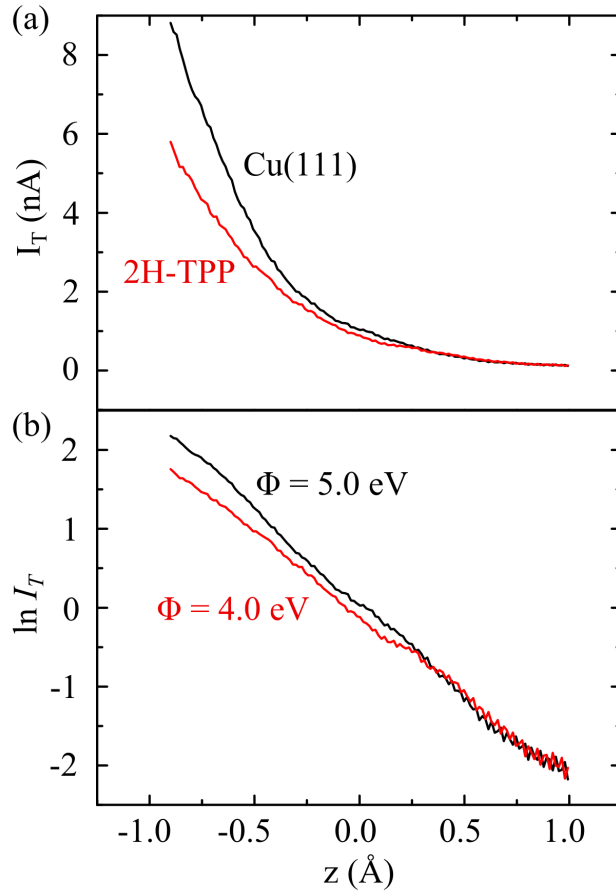
Figure 2.11: (a) I(z) curves of Cu(111) surface and adsorbed 2H-TPP molecule. (b) ln I_T curves show linear relationship in z with respective workfunctions of 5.0 eV and 4.0 eV.

and is reflected in the $I_T(V)$ signal at increased energies [46]. By keeping the voltage during any measurements of $I_T(z)$ to within 350 meV of E_F, one can therefore gain an accurate measure of Φ.

From this we see that by varying tip-sample distance under a constant potential V, an approximation for Φ is obtained [23]. Together with the ability of STM to map local structures, the variations in the surface workfunction can be related to local structures such as defects, step edges or adsorbates [23, 47, 15].

A spatially resolved map of the work function can be obtained by taking $I_T(z)$ curves at a single
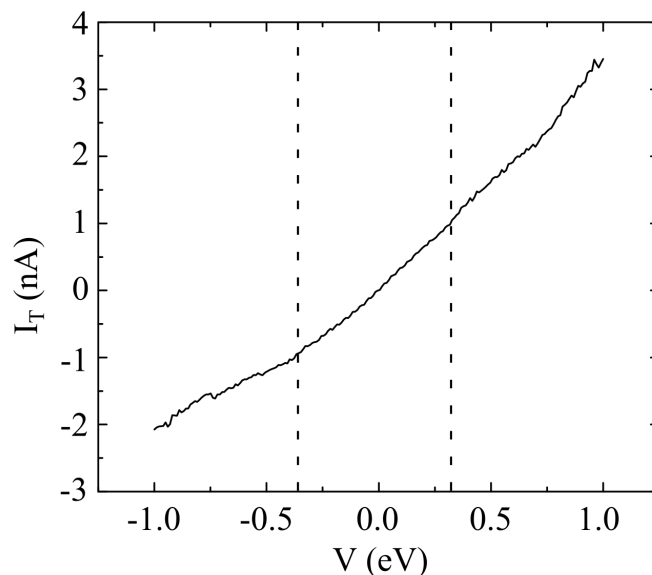
Figure 2.12: $I_T(V)$ curve of Ag(111) surface showing linear relation between I_T and V in the energy range of ± 0.35 eV. It is in this range that Equation 2.8 provides an accurate description of the LBH.

bias voltage over a grid of specific points and then determining Φ by the observed variations. A second method is very similar to the spectroscopic mode. The height z is varied over a small *pm* range at high frequency as the tip is scanned across the surface. As described in Chapter 2.2.2 for the measuring of dI_T/dV, by measuring the changes of $ln\ I_T$ in z ($dln\ I_T/dz$), measurements of Φ are obtained. The results using both methods provides great insight into the nature of the local electronic interactions on surfaces, as in the example below, Figure 2.13 (c). The first method, while much more costly in time, provides raw data of the $I(z)$ curves over a larger range in z. It is therefore much easier to establish the ranges of the simple exponential behavior in Equation 2.8, allowing a more accurate choice of the data range to use for each point. With the latter method, the variation is small and the accuracy of the range not varying over the sample is assumed.

In either case, the measurements of Φ provide a direct method to confirm the *local* changes in surface potential with adsorbed species. As with Figure 2.13 (c), local increases and decreases of Φ shows a great dependence with the sub-molecular characteristics of the adsorbed 2H-TPP as
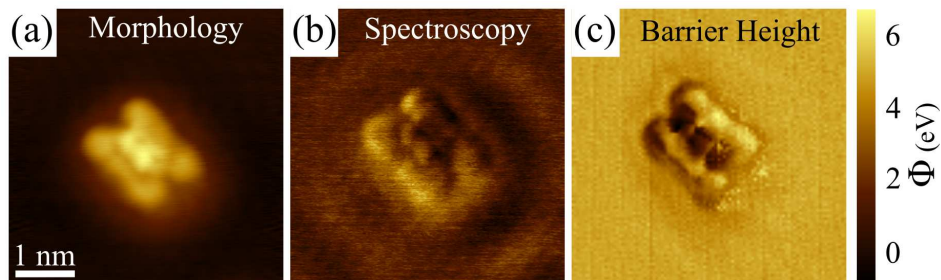
Figure 2.13: Example of three topological maps taken simultaneously over the same sample, a single 2H-TPP molecule adsorbed on a Cu(111) single crystal surface. The z-dependent surface features (a), the DOS at $V = +0.4eV$ (b) and the variation in the surface workfunction (Chapter 2.2.3) (c).

well as the immediately surrounding Cu(111) surface. Differences in the local Φ are seen here to vary by as much as ~ 6 eV. From this measurement, the observed behavior of the molecules and the integral measurements of the DOS are able to be described by existing theories using this map of changes in local barrier potential.

2.3 Photoelectron Spectroscopy

The second method of measurement used in this study is that of photoelectron spectroscopy (PES), specifically in the energy range of ultraviolet light or ultraviolet photoelectron spectroscopy (UPS). Photons are impinged on a surface at a frequency ν being absorbed by the sample on the surface, Figure 2.14 (i). The absorption excites electrons from bound states into the vacuum with some kinetic energy E_k. The sample is placed below a narrow aperature and a series of electron lenses which focus the beam of outgoing electrons (ii). After passing through the lenses, the electrons reach a small aperature into a hemispherical chamber, (iii). The width of the aperature and strength of the lenses limit the kinetic energy of the electrons examined to the range desired. After passing through the aperature, electrons then reach a hemispherical energy analyzer (iv). Voltages are applied across the walls of the hemispheres, forming an electrostatic lens that focuses electrons of a given energy on a micro channel path detector (v) [48].
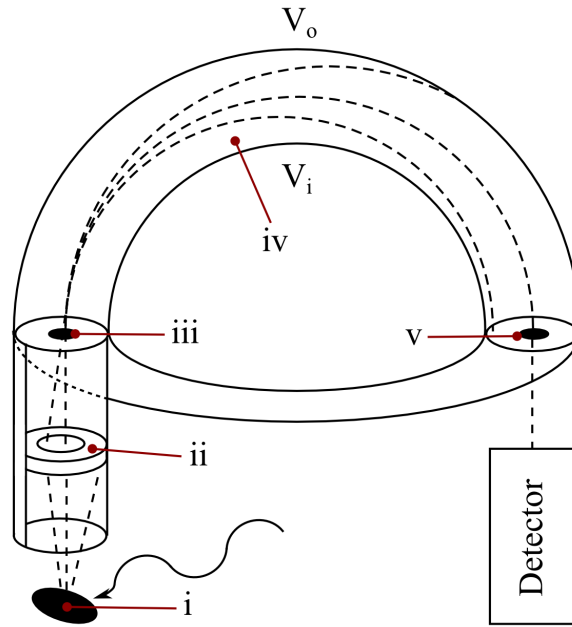
Figure 2.14: (i) Photons impinge on a sample surface, freeing electrons from bound states. (ii) The electron beam is focused through a series of electron lenses, and (iii) the electrons pass through a small aperture into a hemispherical chamber allowing only electrons of a given trajectory into the apparatus. (iv) The biases applied across the hemispheres cause electrons outside the desired kinetic energy range to hit the walls of the hemispheres. (v) Those electrons of the desired kinetic energy then pass through a second aperature and onto a microchannel path detector for measurement.

The kinetic energy of the outgoing electrons is given by,

$$E_k = h\nu - \Phi - E_B \tag{2.9}$$

where ν is the frequency of the photons, Φ is the workfunction of the sample, and E_B is the binding energy of excited electrons. As the photons are absorbed by the sample, the electrons of a given energetic state, E_B, are excited to higher energies thereby ionizing the sample Figure 2.15. The detector is scanned across E_k comparing the ionizing energy of the electrons across energy and a spectroscopic map of the energy levels is constructed. An example is shown in Figure 2.16 of Zn-TPP gas in vacuum [49]. The peaks observed in the spectra correspond to the energy levels

of the free molecule.
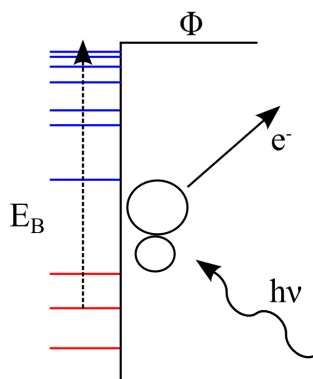
Figure 2.15: Photons of some energy $h\nu$ bombard a molecule, exciting electrons from occupied states to energies above Φ, thereby freeing the electrons and ionizing the molecule.
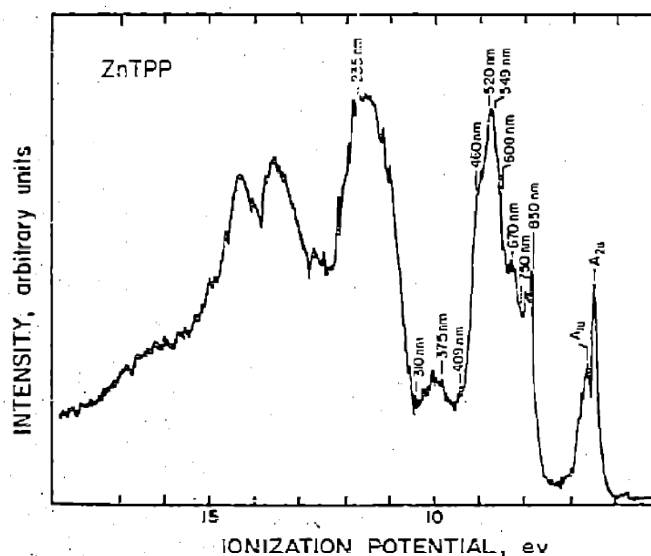
Figure 2.16: UPS spectra of Zn-TPP in vacuum [49]. The energy states of the molecule are observed as peaks of specific energies (here written in wavelength), and the highest occupied orbitals assigned symmetries.

In the case of organic materials, the situation is further complicated by the fact that, as discussed earlier, inelastic vibrational states exist at energies in between the electric states of $E_{tot}(N-1)$ and

$E_{tot}(N)$ [50]. Considering the vibrational modes of the molecule as a quantum harmonic oscillator, these energies correspond then to the energies of the modes of the harmonic oscillator and also require energetic consideration along with the orbitals of the molecule [51, 52]. The vibrational modes of molecules are not limited to a single frequency, but, like the classic harmonic oscillator, exist also in multiples of the vibrational modes $nh\nu_{vib}$.

The peaks due to the vibrational modes therefore overlap with the orbitals of the molecules and create further broadening of the measured energy levels. An example is shown for N_2, CO, and O_2 on a Xe buffer layer in UHV, Figure 2.17 [51]. The sharp bands beneath the broad peaks represent the vibrational spectra of the relevant molecules and are discernable for the N_2/Xe sample.
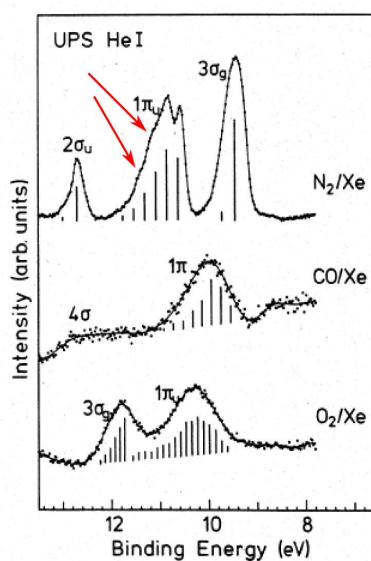
Figure 2.17: Spectra of molecule dimers of N_2, CO, and O_2 on Xe buffer layers on Ni(111) [51]

The unoccupied electronic states are measured using the same principles but the inverse methodology, inverse photoemission spectroscopy (IPES). Electrons of some kinetic energy E_k are bombarded onto the sample. In hitting the sample, the electrons bind to unoccupied states E_B, eventually decaying to lower energetic states of energy $E_{B'}$. In the decay, a photon is relesead of energy $h\nu = E_k + \Phi + E_B - E_{B'}$. Through continuous bombardment and simultaneous measure-

ment of the outgoing photons, the differences in electronic states can be constructed and a map of the energy levels of the system.

Chapter 3

Organic chemistry on metal surfaces

In this chapter, a brief explanation of the self-assembly of organic materials on metal surfaces is presented. Basic principles are reviewed, followed by a more in-depth discussion of the binding mechanisms differentiating organic molecules from metal adatoms. Finally, the existing theories of electron exchange and surface dipoles are included as they play a key role in limitations of this process, as shown in this thesis.

3.1 Interface energetics

Adsorption is the process where a gas-phase particle (any atom, cluster, molecule, etc.), the adsorbate, interacts with an exposed surface, forming a bond strong enough to prevent it from releasing back into the gas phase, desorption. The chance of desorption increases with ambient temperature due to thermal motion of the adsorbate. Therefore, the adsorption energy (E_{ad}) must be large enough to compensate for this at the temperature the device is intended for use (typically room temperature or above). This is typically on the order of 1 eV [53]. Current research has observed binding energies for noble gases and organic molecules ranging between 100 meV and 6 eV, depending on the surface of adsorption [54].

Molecules have a similar wide range of binding energies, with those attributed to chemical bonds (chemisorption) tend to be on the order of several eV [55, 56, 57] and that physically bound (physisorbed) systems on the scale of 10^{-2} eV [57, 58]. It was previously the energy scales themselves which previously defined the nature (physisorption vs. chemisorption) of the interaction. However, as binding energies vary in a continuum between these scales, this has since been found to be a rather arbitrary boundary [58]. Most frequently now physisorption is defined where the binding is due mainly to weak van der Waals forces, the molecule retains its chemical uniqueness, any shifts in energy are uniform throughout the band structure, and any charge exchange is "minimal" [57, 58, 14]. Chemisorption is then defined where the energy levels of the surface/molecule system are unique, the energy levels of the molecule may be shifted relative to one another, and there is "significant" electronic exchange [59, 57, 58]. Even these definitions however are somewhat arbitrary. What constitutes "significant" and "minimal" are not properly defined and, due to energy level broadening and deformation of geometry, the energy levels of adsorbed molecules are different from the free molecule. While some authors refer to interactions of intermediary energy with some charge exchange as strong physisorption [58, 60], others refer to them as weak chemisorption [57, 61].

A schematic of the metal/molecule energy interface is shown in Figure 3.1. Here, the metal surface is on the left, in region (i) and the free molecule is represented by discrete occupied (red) and unoccupied (blue) energy levels (orbitals) on the right (iii). The region between (i) and (iii) represents the interface: the molecule adsorbed on the metal surface (ii).

On the metal, E_F represents the Fermi energy, the highest occupied energy of electrons in the metal. All energy states below E_F are therefore occupied by electrons in a continuum, represented by the black striped lines. The vacuum energy E_v^∞, is the energy level of a free electron far from the surface of the metal. E_v is the energy of a free electron, near to the surface. The potential energy at E_v is raised, as the electron is close enough to interact with the dipole created on the surface by surface electrons tailing into the vacuum. Φ, the workfunction, is simply the energy necessary to
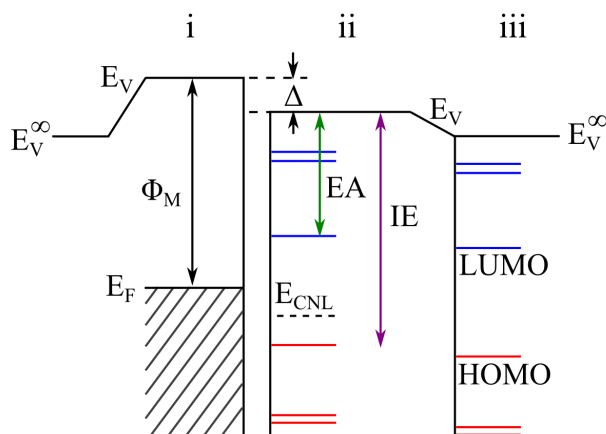
Figure 3.1: The energy levels of a metal surface (i): The vacuum energy far from the surface (E_V^∞) and near the surface (E_v), workfunction (Φ), and Fermi energy (E_F). The occupied states are represented by striped lines. The energy levels of a molecule near the surface (ii): The electron affinity (EA), ionization energy (IE), charge neutrality level (E_{CNL}), and surface dipole energy (Δ). The energy levels of the molecule far from the surface (iii): highest occupied molecular orbital (HOMO), lowest unoccupied molecular orbital (LUMO), and vacuum energy (E_v^∞).

free an electron from the highest occupied energy of the metal.

As the free molecule is isolated (iii), the orbitals exist at discrete energies, indicated by the horizontal lines. Here the highest occupied molecular orbital (HOMO) is and the lowest unoccupied molecular orbital (LUMO) are labelled to indicate the gap between occupied and unoccupied orbitals. As the molecule is different from the metal, the vacuum energy of the free molecule is not necessarily the same as the metal. The purple line labelled IE, is the ionization energy, the energy required to remove an electron from the HOMO to the vacuum. This is similar to the workfunction of the metal. The green is what is referred to as the electron affinity, EA, or the energy difference between vacuum and the LUMO. The larger EA, the more energetically favorable it is to gain charge, and the easier it is for electrons to bind to the molecule. Whereas the larger IE, the more difficult it is to remove electrons from the system. E_V^∞ for the free molecule is simply the energy of a free electron, as there is no dipole of the molecule tailing into the vacuum. For this reason E_v^∞ for the molecule is aligned with E_v^∞ for the metal.

Upon adsorption to the surface (ii), a bond is formed between the metal and the molecule. The

close proximity of the molecule to metal surface forces the molecule to interact with the dipole created by the metal surface electrons. With no rearrangement of surface charges, this potential increases or decreases the apparent vacuum level of the molecule. This shift in E_v is indicated by Δ, the interface dipole of the adsorbed system. The larger Δ, the more difficult it is for electrons to be absorbed. Depending on the nature of the bond, the energy levels of the metal/molecule system may shift. Upon adsorption, there is a broadening of energy levels, depending on the strength of the interaction. For strong interactions, this can lead to a continuous density of states (DOS) between the discrete orbitals, the interface states or metal induced gap states. The charge neutrality level (E_{CNL}) is the energy level where charge occupancy up to this energy results in a neutral molecule. If the electron occupancy of the metal/molecule system is above (below) E_{CNL}, the system is negatively (positively) charged. E_{CNL} does not occur halfway between the HOMO and LUMO, instead it is dependent on the relative DOS of the unoccupied and occupied energy states, and is therefore closer to the HOMO (LUMO) where the density of unoccupied (occupied) levels is higher than occupied (unoccupied) levels [62].

3.1.1   Physisorption

The most common metal/organic systems studied over the last decade or so have been organic molecules with very weak interaction with the metal surface, physisorbed molecules. The diagram shown in Figure 3.1 represents one such case: a simple van der Waals interaction between the molecule and the metal surface. Here, the energy levels of the molecule weakly shift and there is no overall alignment between the molecular orbitals and energy levels E_F or E_v of the metal. The orbitals remain discrete, and there is a vanishingly small DOS between orbitals, therefore charge can only be exchanged between the metal and discrete orbitals of the molecule. The HOMO remains at energies lower than E_F, so there is no exchange of charge from the molecule to the metal and the LUMO remains at energies above E_F, so there can be no charge exchange from the
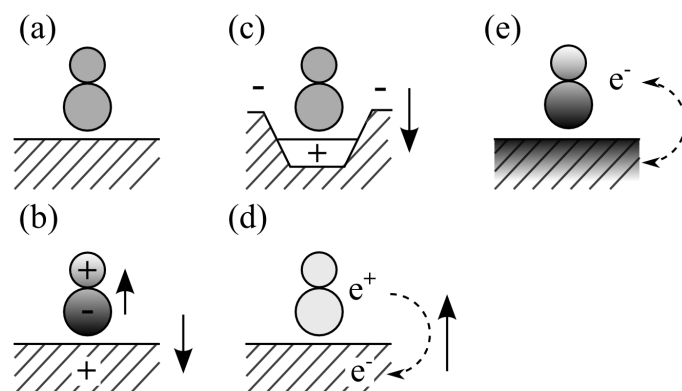
Figure 3.2: A single molecule weakly adsorbed on a metal surface illustrating a variety of interactions. (a) weak pysisorption with no rearrangement of charge, (b) dipole formation due to mirror charges, (c) shift of surface DOS due to pillow effect, (d) charge transfer due to Schottky-Mott interaction, and (e) charge transfer due to interface states.

metal into the molecule. In this case, the molecule remains simply weakly bound to the surface with little or no change in energy levels. This is illustrated in Figure 3.2 (a).

This weak interaction results in a decrease in the workfunction over the adsorbed molecule. The electronic orbitals of the metal surface atoms spill from the bulk into the vacuum, creating the increased electron density responsible for Φ. This increased negative charge density outside of the metal induces an image charge within. For those neutral adsorbates weakly bond to the surface, the positive mirror charge creates an electrostatic gradient, inducing a dipole in the adsorbate, as seen in the positive (light) to negative (dark) gradient in Figure 3.2 (b). This results in two dipoles: the intra-adsorbate dipole and the adsorbate-surface dipole, the latter generally being large than the former due to increased distance. This dipole acts in the direction opposite that of the surface electron dipole, thereby lowering the workfunction [63].

3.1.2 Reordering of surface charge

This model is incomplete however as it assumes little or no geometric change in electron orbitals. Upon adsorption, the orbitals of the adsorbate overlap with the tails of the orbitals of the

surface electrons of the metal which spill into the vacuum. Pauli repulsion between the metal and adsorbate forces rearrangement of these orbitals to minimize overlap [64]. In the case of closed-shell systems such as noble gases and simple organics, the electron cloud of the adsorbate is not easily deformed and as a result, the surface electrons of the metal are instead strongly reordered [65, 66]. The density of surface electrons under the molecule decreases, while the density surrounding of the molecule increases.

As a result, the electron density sinking into the vacuum is pushed further into the metal and outward to the sides of the adsorbate, as in Figure 3.2 (c), the so-called "pillow effect" [65, 67, 68]. While there is no exchange of charge between the isolated molecule and the surface, the decrease of the electron density under (around) the molecule lowers (increases) the surface dipole in the region where orbitals have receded (advanced), just as with a molecule with a permanent dipole (Figure 3.2 (b)). This therefore creates a change in the dipole in addition to Δ. This dipole change is frequently considered parallel with any changes in work function, described as

$$\Delta\Phi_{PE} = \frac{4\pi D}{A} \tag{3.1}$$

with D the surface-molecule dipole and A the area of the adsorbed species. However, such changes are only accounted for in the case of metals whose spill-over electrons, typically d orbitals, are most important to the work function of the metal [69]. The dipole created by the rearranged charge then weakly contributes to new electrostatic forces, aiding in inter-adsorbate repulsion and limiting the self-assembly of the adsorbate [70]. In the cases of other metal systems and those with significant hybridization of the metal-organic states, more complex methodology is required for description [68].

3.1.3   Schottky-Mött semi-conductor model

The model applied to many metal/semi-conductor interfaces has been applied to some metal/organic interfaces as well. This is the Schotkky-Mött model, which assumes energy level alignment at the interface between between E_V of the molecule and the metal, such that $\Delta = 0$ [71], Figure 3.3 (a). Here, the energy levels of the adsorbate do not shift relative to one another, but rather they all shift by the same change in energy given by $E_v - E_v^\infty$. This weak interaction is dependent only on the initial differences in E_V, so long as $\Delta = 0$ and $IE < \Phi < EA$. With $\Delta = 0$, the surface dipole under the molecule disappears.

Upon adsorption however, the interaction between the adsorbate and the metal surface induces a hybridization between metal and adsorbate states, resulting in resonance of the adsorbate states into broadened levels with Gaussian shape [72]. While the DOS between the energy levels remains small enough to be ignored, when the Φ approaches the same magnitude as EA or IA (as shown in the figure), the Fermi energy overlaps with the tail of the orbital [73]. This overlap then results in charge exchange, causing the molecule to lose (gain) charge as the shoulder of the HOMO (LUMO) overlaps with E_F [74], creating a surface dipole in the region of the molecule, as shown in Figure 3.2 (d). Here, the overlap results in a loss of charge from the molecule. This typically occurs at energies on the order 0.3 eV from the band edge of the state [1].

3.1.4   Energy level pinning

While the Schottky-Mött model accurately describes the interaction between noble surfaces and some weakly interacting molecules, studies over most molecules have found that $\Delta \neq 0$ [14]. A recently proposed model by Rusu [66] maintains the same description of electron transfer from the tail of the energy level into the metal as the Schottky-Mött model. In this model however, the Fermi energy is pinned to the nearest molecular orbital, rather than E_v of the systems aligning, Figure 3.3 (b). This pinning results in electron transfer between the molecule and the metal surface,
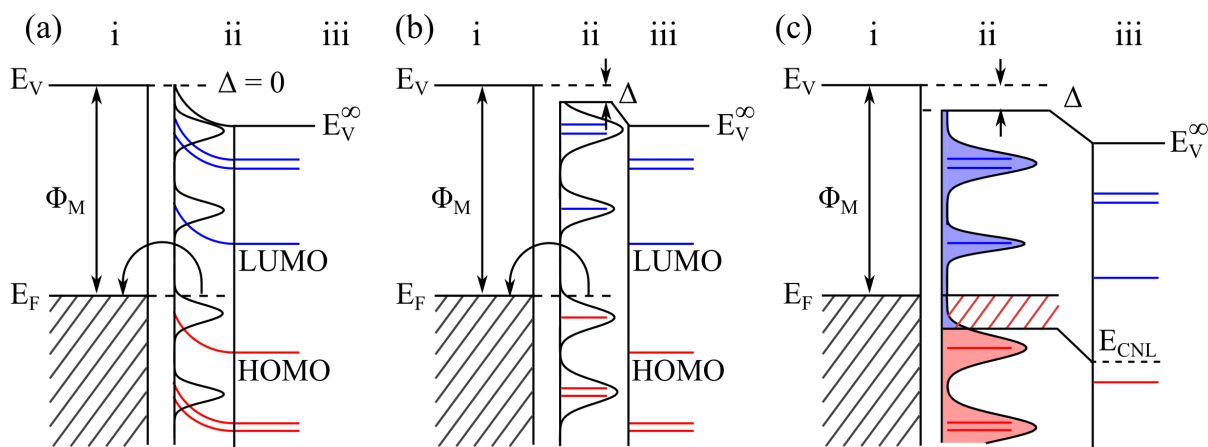
Figure 3.3: (a) the Schottky-Mött model results in alignment between E_v and $\Delta = 0$. All states shift by the same amount and create widened DOS due to the interaction at the interface. (b) E_F alignment shows E_F pinning to the orbitals of the adsorbed molecule. (c) the IDIS model results in E_F pinning closely to E_{CNL}, resulting in charge transfer between the adsorbate and surface depending on whether $E_F > E_{CNL}$ or $E_F < E_{CNL}$.

creating a dipole on the surface dependent on the relative energies of E_F and the nearest molecular orbitals. As E_v^{∞} is equal between the free molecule and the surface, and E_F aligns with the nearest molecular orbitals, any shift in E_F and Φ of the metal results in pinning of E_F to different orbitals. While the workfunction of the free metal surface may decrease, the higher E_F aligns with more unoccupied orbitals and creates an exchange of more charge which results in an increase of the surface dipole. This change in dipole then matches the change in workfunction between metals, making the observed workfunction of the metal/molecule sample remain constant [66].

While this has been observed for some systems, such as PTCDA [66] and C_{60} [75], other molecules such as benzene have shown no such interaction. Rather, the observed Φ of benzene is seen to vary linearly with the workfunction of the metal, consistent with the pillow-effect model proposed by Paul Bagus [66].

3.1.5   Induced density of interface states

Another explanation for systems where $\Delta \neq 0$ is a model borrowing heavily from models of semiconductors with noticeable DOS between the discrete energy levels, the induced density of interface states (IDIS) model. In this model the energy level broadening induces a small, continuous set of energetic states between the energy levels Figure 3.3 (c), these are the interface states or metal induced gap states (MIGS) [76, 77, 78].

Further, the energy level alignment is between the states of neutral charge in the metal (E_F) and the molecule (E_{CNL}), and not between E_v of the metal and adsorbate as in Figure 3.3 (a). Similar to above interfaces, E_F and E_{CNL} align through electron transfer, the only difference here being the the transfer is due to the creation of interface states between the orbitals of the molecule. Electrons are passed between the two systems until the electron occupancy of the organic is such that $E_{CNL} \simeq E_F$. This is indicated in Figure 3.3 (c) by the red stripes between E_F and E_{CNL}, indicating continuous electron occupancy, as with the underlying metal. In so doing, the gain/loss of charge creates a dipole on the metal surface and the various adsorbates repel one another through long-range interactions depending on the net charge exchanged Figure 3.2 (e).

In the ideal model, charge uptake occurs just as easily as between two metals and therefore this can be thought of as two interacting metal systems rather than a metal/semiconductor interaction [62, 60]. The parameter currently used to predict which model (IDIS, Schottky-Mött, or E_F pinning) applies to what is known as the screening parameter,

$$S = \frac{dE_{CNL}}{d\Phi} = \frac{1}{1 + 4\pi e^2 DOS(E_F)\delta/A} \tag{3.2}$$

where $DOS(E_F)$ is the local density of interface states, δ the molecule-surface separation, and A the molecule surface area. In the Schottky-Mött model, it is assumed that the molecular structure remains generally unchanged except for weak, expected broadening. In this case, there should be little or no change in the DOS between orbitals and DOS should be near 0, $S \sim 1$. In the IDIS

model, the induced continuous states between orbitals is large enough that the $4\pi e^2 DOS(E_F)\delta \gg 1$, and $S \sim 1$. This parameter varies significantly between molecular species with many falling about half-way between the two models [79]. Specifically, the the screening parameter of TPyP is S_{TPyP} = 0.44 [80], indicating that there is some form of interaction with the surface stronger than then Schottky-Mött model but weaker than the IDIS model.

These charge transfer interactions (Schottky-Mött, E_F pinning, and IDIS) result in adsorption energies on the order of 2.0 eV for weakly bound systems [81, 82], providing the binding energy necessary to hold adsorbates at the temperatures of interest. Furthermore, these three models are independent of the surface dipole created by surface state reconstruction and mirror charges, which have even been included most recently in IDIS models [83]. In all these cases, the adsorption results in surface dipoles determined by a) the amount of charge transferred, b) the surface reconstruction, and c) mirror images. These large dipoles and adsorbate charges result in inter-molecular repulsion, which, if of large enough magnitude, prevents inter-molecular bonding and self-assembly [10]. It is not the adsorption energy which prevents the motion of the molecules and inter-molecular binding. This is seen by both the inter-molecular binding of the physisorbed PTCDA [82] and the the inter-molecular binding of the chemically adsorbed (chemisorbed) HtBDC on Cu(110) [84]. What then limits the inter-molecular bonding and self-assembly is the relation between the dipole strength of the adsorbates and the magnitude of the bonds formed between adsorbed molecules.

3.2   Hierarchy of chemical bonds

As the molecules physisorbed on the metal surfaces considered in this dissertation are carbon-based organic molecules, the inter-adsorbate interaction is different from that of metal adsorbates. Adsorbed metal atoms are single particles which interact through covalent bonds between their respective unfilled atomic orbitals. Adsorbed organic species are instead closed-shell molecules, several Å to nm larger than adsorbed atoms, which lack d orbitals.
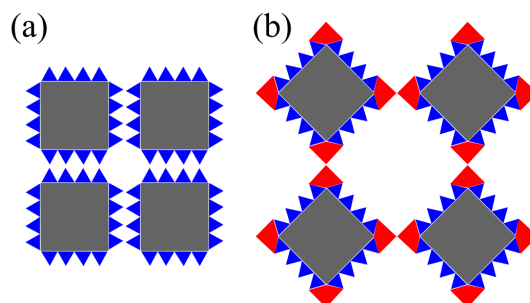
Figure 3.4: (a) Molecules bonding through weak interactions along the edges orient in a close-packed square array. (b) Molecules bonding through a larger interaction on the corner of the squares orient in a less close-packed checker board array.

The inter-molecular interactions which counter act the repulsion felt by the surface dipoles created upon adsorption are therefore different than those between adsorbed adatoms. With this said, the chemical bonds between adsorbed molecules are that which act against the repulsive interactions and determines the stability and symmetry of the molecular structures. The key importance is twofold. The first is that there are a wide variety of these interactions and a distinct hierarchy to their ranges and strengths. The second is that due to the spherical asymmetry of organic molecules, these chemical bonds are anisotropic and therefore force the molecules to orient along the axes of the interactions [85]. This combination allows for flexible engineering of the supermolecular structure while keeping the molecule largely unaffected.

This is illustrated in Figure 3.4. Square molecules where the strongest inter-molecular bond is along the edges of the molecule will align so as to maximize the bonds along this direction. This results in a supermolecular ordering with compact, square symmetry (a). If, however, a second set of intermolecular bonds are of greater strength and are located on the corners of the molecules, the molecules align to maximize this bond, resulting in a much less compact, checker-board like supermolecular ordering (b).

We can then engineer the supermolecular structure by controlling the geometry and make up of the molecule, as we control which interactions take place and where. It is this flexibility which gives organic molecules such amazing potential for application: by simply replacing a single com-
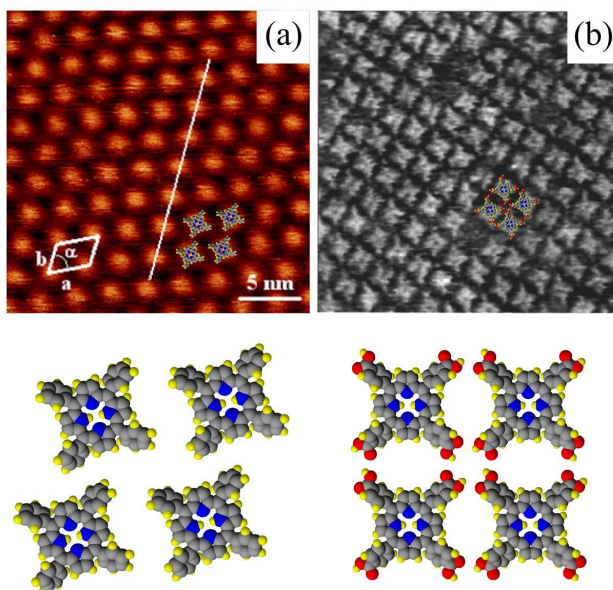
Figure 3.5: (a) STM image of tetraphenyl porphyrin (TPP) on HOPG surface bound by van der Waals and CH-π bonds [86] and (b) STM image of tetra carboxyphenyl porphyrin (TCPP) on HOPG surface bound by hydrogen bonds [87]

ponent of the molecule, we can keep the overall electronic properties of the system constant while controlling the geometry of the final system!

This is shown in Figure 3.5 for tetra phenyl porphyrin on the surface of highly ordered pyrolitic graphite (HOPG). A layer of 2H-TPP bound to the substrate interact with one another through weak bonds, forming an ordered rhombohedral pattern with 3.2 nm spacing [86], Figure 3.5 (a). As described in Chapter 3.2.2, a hydrogen bond between two craboxylic acids are of the order of ten times as large as a van der Waals interaction. This is seen in Figure 3.5 (b) where a layer of tetra carboxyphenyl porphryin (TCPP) interact through the much stronger hydrogen bonds of the carboxylic acid end groups on the ligand, resulting in a slightly more compact spacing of 1.8 nm in a square-symmetric positions with the molecules oriented parallel to the direction of ordering [87]. Simply by replacing the H bound to the tip of the phenyl ligands with a carboxylic acid, the ordering of the molecules and the inter-molecular spacing are customized.

The key importance to the inter-molecular bonds formed between organic adsorbates is the fact that the most common are not covalent, but are rather complex dipole interactions between organic components. Due to the dipole nature of these bonds, this allows the bonds between the molecular systems to be broken and reformed again with no change to the chemical nature of the component molecules. This reversibility is ideal for self-assembled structures, allowing customization and control of the super-molecular ordering desired. In order to customize the interactions and understand the relationship between the various organic bonds however, the interaction ranges and bond strengths must also be understood. For this reason, a quick review is presented below of the five most common reversible inter-molecular interactions as well as a comparison to the use of covalent bonds in inter-molecular surface super structures.

3.2.1   van der Waals bonds

For many molecules, the primary molecule-molecule interaction is the dispersive component of the van der Waals (vdW) potential. This is an electrostatic interaction with no fundamental, underlying directionality. Where there is no permanent asymmetry in the charge distribution (non dipolar molecules/atoms), the only component of the electrostatic potential is the dispersion effect [88]. The charged electrons on the surface of the molecular or atomic electron shell interact with those electrons on the surface of the neighboring particles. This very weak electrostatic interaction is only strong enough to effect the shell electron itself, and not the shielded charges in the lower orbitals or the nucleus. The electron-electron repulsion creates a momentary dipole forcing the neighboring charge to move away, before shifting back into position. This is best described as the tendency of shell electrons of neighboring material to oscillate in phase with one another. This oscillation, creates a very weak dipole at any given moment and the molecules remain weakly attracted to one another, Figure 3.3 (a). Both the interaction energy ($0.02 \sim 0.1$ eV) and the range over which it takes place are fairly weak compared with other chemical bonds, Table 3.1.
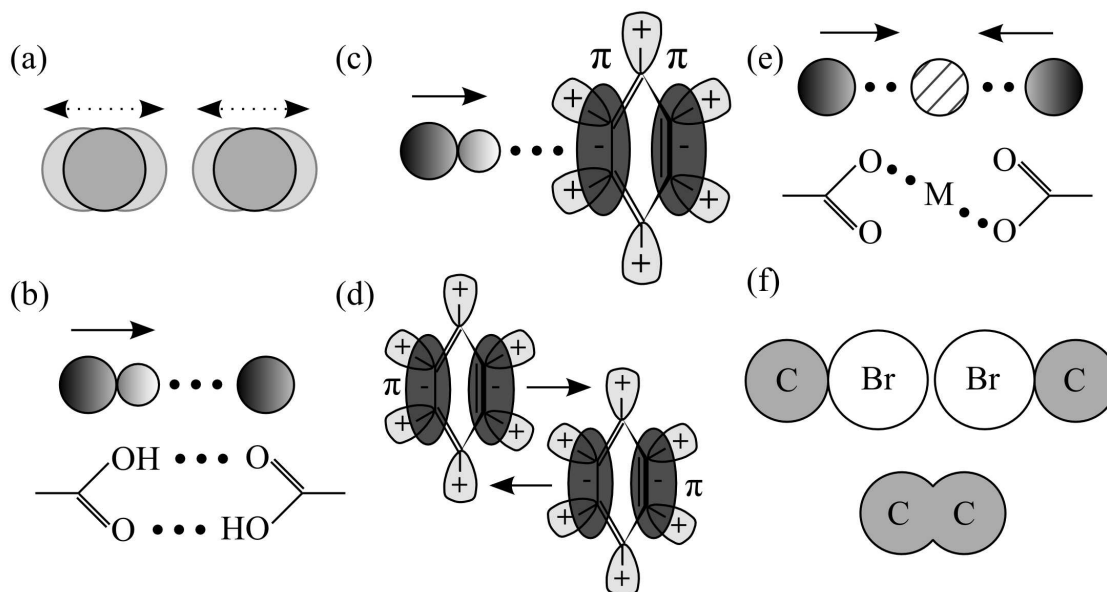
Figure 3.6: Examples of the most common intermolecular bonds, dark is negative charge and light positive. (a) van der Waals interaction between oscillating atoms. (b) hydrogen bond between charged dipoles, (c) CH-π bond, (d) metal-ligand coordination, (e) $\pi - \pi$ stacking, and (f) covalent chemical bond.

Table 3.1: Inter-molecular bond types, energies, and interaction ranges

Bond	Energy Range (eV)	Interaction Range (Å)
van der Waal	$0.02 \sim 0.1$	~ 1
CH-π	$0.06 \sim 0.1$	$1 \sim 2$
$\pi - \pi$	0.1	$3.2 \sim 3.8$
Hydrogen bond	$0.05 \sim 0.7$	$1.5 \sim 3.5$
Metal-ligand	$0.5 \sim 2$	$1.5 \sim 2.5$

For the case of spherically symmetric adatoms, this interaction is non-directional and as such does nothing to order the bonding adsorbates relative to one another. Organic molecules however, lack the spherical symmetry of such noble gas atoms. So, while the local dispersion force between oscillating electron clouds creates a generally isotropic attractive force, the asymmetry of the organic molecules forces the net interaction between molecules to become anisotropic [85]. Such forces result in the alignment of all molecules based on geometry of the molecules themselves, Figure 3.7 (a).
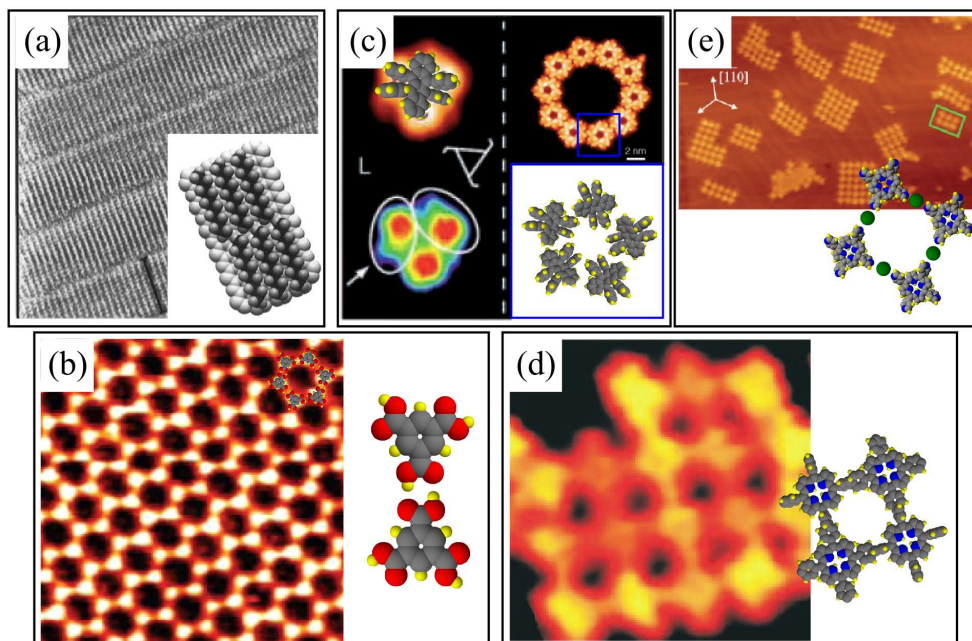
Figure 3.7: (a) Polymers exhibit close packed structures reflecting the chirality of individual molecules [89] (b) TMA network formed by hydrogen bonds [90] (c) rubrene/Au(111) forms chiral networks due to $\pi - \pi$ stacking of ligands [91] (d) Br$_4$-TPP/Au(111) form covalent bonds through bromine substitution [92] and (e) two-dimensional Cu-TPyP MOCN formed on Au(111) [93]

3.2.2 Hydrogen bonds and π orbitals

The key interaction however between many organic molecules is a dipole interaction dependent on the hydrogen atoms along the edge of the various oxygen, carbon, and nitrogen atoms. Upon forming a covalent bond, the charge distribution of the X-H dimer (where X is either C, N, or O) becomes uneven, with the X atom negative and the H atom positive. The relative electronegativity of the component atoms creates an uneven charge along the axis of the covalent bond, resulting in a dipole facing from the X atom to the H. This dipole then attracts lone oxygen, nitrogen, or carbon atoms, and a weak electrostatic bond takes place with a bond length between 1.5 Å to 3.5 Å, Figure 3.3 (b). In the case where a carboxylic acid (COOH) is located on the ends of molecules, the alignment is such that the O-H of one molecule bonds to the O of the other and vice versa, as in Figure 3.3 (b). This is what is referred to as a hydrogen bond. As the interaction is directional and

highly adaptable, both the bond distance and the strength depend strongly on the dipole magnitude of X-H and electronegativity of the free atom to which they bind [94, 95, 96]. Due to the anistropy of the dipole moment, any hydrogen bonds formed between adsorbed molecules exhibit the same anisotropy. This can result in networks with directional bonds that do not exhibit the same close packed nature as the vdW interactions, as shown in Figure 3.7 (b).

It can be difficult to form these bonds in the exact single dipole-dipole interaction pictured in Figure 3.7 (b) however as this requires directly aligned axes of the COOH - COOH bonds. As shown in Figure 3.5 (b), carboxylic acid end groups may instead align off-axis. While this weakens the magnitude of the individual hydrogen bonds, it provides more room for a third or fourth COOH end group to form similar weaker bonds, thereby increasing the net magnitude of the bond. This is the difference seen between the TMA bonds in Figure 3.7 (b) and the TCPP bonds in Figure 3.5 (b).

This same dipole interaction extends to interactions between such X-H dimers and the much more disperse π orbitals of organic molecules. The π orbital is a molecular orbital formed by the overlap of the out-of-plane p orbitals in neighboring C atoms, as shown in Figure 3.8 (a). As an example, in benzene, the p orbitals of the carbon extend normal to the plane of the molecule. The resulting overlap creates a ring-like shape above the plane of the molecule. With the six C-H dimers laying on the six corners, the resulting C-H dipole creates a series of positive charges along the rim of the molecule confining the negative charge of the ring-like π orbitals above and below the plane of the molecule, creating a quadrupole [97], Figure 3.8 (b).

When near to C-H dipoles, the C-H dimer forms a weak bond with the quadrupole of the π orbitals, facing normal to the plane of the aromatic ring, Figure 3.6 (c). Due to the increased dispersity of the π orbital compared to carbon, oxygen, or nitrogen atoms, the interaction distances are much more confined but slightly larger than the vdW interaction, typically between $1 \sim 2$ Å[98]. Furthermore, while larger than the vdW interaction, the CH-π interaction is noticeably weaker than the hydrogen bond at $0.06 \sim 0.1$ eV [99], placing this interaction somewhere between the vdW and
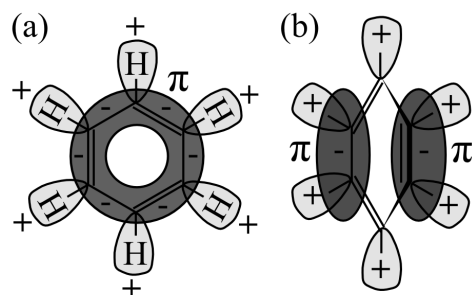
Figure 3.8: (a) Top-down view of benzene molecule showing π orbital (dark) along the rim of the molecule and σ orbitals (light) of the C-H bonds. Here the dark color represents negative charge and the light negative charge. (b) 45° side view of molecule shows π orbitals extending above and below the plane of the molecule.

hydrogen bonds.

This intermediary placement of the bond energy and interaction distance is explained appropriately enough by a combined bond of the vdW and hydrogen bonds. The geometry of the aromatic ring results in the positively polarized hydrogens lying on the outer edge, and the negatively charged π orbitals above and below the plane of the molecule, Figure 3.6 (c). This creates a weak quadrupole arrangement of electrons [100]. While the resulting dipole-quadrupole interaction is significantly weaker in electrostatic polarizability than a dipole-dipole interactions of the hydrogen bond [98], it provides directionality not present in the vdW interaction [99]. This weak interaction with bonding anisotropy results in closely packed structures, ordered according to the relative geometry of the π orbitals, Figure 3.7 (c).

Another directional interaction between aromatic species is the more complex π stacking. In this interaction, the aromatic rings arrange themselves in such a manner that the π orbitals are parallel and shifted to one another, with the C-H dimers of the rims above the π orbitals forming two CH-π bonds, Figure 3.6 (d). The interaction is of the same energy as the CH-π interaction despite the dual CH-π bonds for the following reasons.

The interacting π orbitals have the same negative charge while the σ orbitals of the C-H instead has a positive charge and is concentrated in the center plane of the molecule. The neutrality of

the molecule then requires that the total charge of the two π orbitals must be equal to the positive charge of the σ orbital. Given that the π orbital is much more diffuse and split in two, this then means that the attraction of the $\pi - \sigma$ interaction is larger than the $\pi - \pi$ interaction and there is a net attractive force [97]. The interaction then causes the aromatic rings to align such that the center of the ring usually stacks above the edge of the other, as in (d). As the π orbitals do not overlap and are significantly diffuse, this results is significantly large separation distances as noted in Table 3.1.

As a significant part of this interaction involves repulsion between the π orbitals, typically the predominant interactions of the molecule-molecule bonds for the currently studied organic systems involve hydrogen bonding and CH-π interactions. This is especially true given the fact that surface studied systems are two-dimensional, and the $\pi - \pi$ bonds require significant rearrangement of the geometric orientation of the molecule.

3.2.3 Metal-ligand coordination and covalent bonds

The available N, C, O end groups of such organic molecules can also be used to form coordination bonds between the adsorbed molecules and co-adsorbed metal ions (linkers), unlike the ionic binding discussed above. The increased number of electron shell vacancies in the transition metal linkers typically used (Ni, Fe, Co, Cu, Ag, Au, etc.) versus the organic end groups, allows the linkers to form bonds with virtually any number of neighboring organic end group [101]. This results in the linkers acting as bridging sites between coadsorbed organic molecules which are then linked together in extended arrays called metal-organic coordination networks (MOCN).

The individual metal-carbon coordination bond is on the order of $0.5 \sim 2$ eV in magnitude, much stronger than the various ionic bonds discussed above, Table 3.1. This bond strength, creates very stable inter-molecular architectures which further act to limit dissociation of individual component molecules at room temperature or above [53]. Furthermore, as the available electron vacancies in the linkers are greater than the available end group bonds within the small area sur-
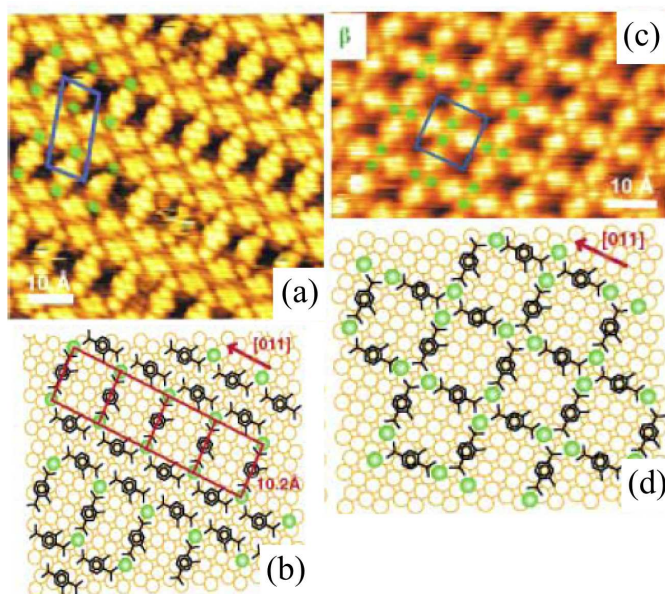
Figure 3.9: (a) TMLA/Cu(100) with deposition of 0.66 Fe/TMLA stoichiometric ratio. (b) Model of predicted molecule/linker MOCN in (a). (c) TMLA/Cu(100) with deposition of 2 Fe/TMLA ratio. (d) Model of predicted molecule/linker MOCN in (c) [102]

rounding the linker, a second component limiting the architecture of the MOCN is the ratio of linkers to molecules.

By increasing the linker/molecule ratio, this increases the availability of linkers to bind to the active end groups of the adsorbed molecules [102]. such changes not only affect the geometry of the enclosed MOCN, but they can be used to create boundaries on the MOCN as desired. As an example, for TMLA/Cu(100) with Fe adatom linkers, a Fe/TMLA ratio of 1:1.51 leaves fewer than one linker for every active molecule, resulting in closed MOCNs bound to each other through weak vdW and hydrogen interactions, Figure 3.9 (a). Upon increasing the ratio to 2:1, there are enough linkers for every component molecule, and the MOCN extends indefinately. This stoichiometric varying allows for the same general control well known in solution-based metal-organic chemistry [103, 104, 105, 106].

Recently, surface studies have begun using this same technique for the construction of single

carbon-carbon covalent bonds in the same manner as the oxygen-metal covalent bonds. Molecules are deposited on surfaces with weakly bound ligand endgroups such as bromine or iodine. Following heating, the endgroup dissociates and the molecules form covalent bonds with one another, Figure 3.6 (f) [92], as shown in Figure 3.7 (e). While these bond energies are much stronger than any of the others, being $\sim$ 3.5 eV, this bond type does not form self-assembled structures like all others heretofore listed, these are not self-assembled structures as the system is not reversible. Once the bonds are formed, the molecules cannot be dissociated without breaking the other carbon bonds holding the molecule together [107].

3.3   Growth dynamics and self-assembly

These inter-molecular bonds are the interactions which drive the well known structural ordering of organic adlayers [108]. Adsorbed molecules distributed across the surface in a disorderd arrangement interact and bind, thereby forming well-ordered supramolecular architectures: self-assembly. The final structure of which is an organized lattice of organic material covering surface, a self-assembled monolayer (SAM). The adsorbed molecules cover all available surface area in a single, compact island. An example is shown below, Figure 3.10 (a). Here, a 300 nm $\times$ 300 nm STM images shows a heterogeneous mixture of 5% 2H-TPP and 95% Ag-TPP on a Ag(111) single crystal surface with three step edges. The molecules cover the entire upper terrace and a large portion of the center terrace, leaving a wide area of unoccupied space rather than remaining statistically distributed across the surface in a disordered arrangement.

A small, 10 nm $\times$ 10 nm section of the island is highlighted along the edge to show the regular ordering of the self-assembled structure (b). The individual component molecules can be discerned, with the 2H-TPP molecules the brighter molecules and the Ag-TPP molecules the darker colored molecules represented by the molecular model with the green center atom. The ordering is easily discerned due to the unoccupied position and edge of the island. Here, the 2H-TPP molecules,
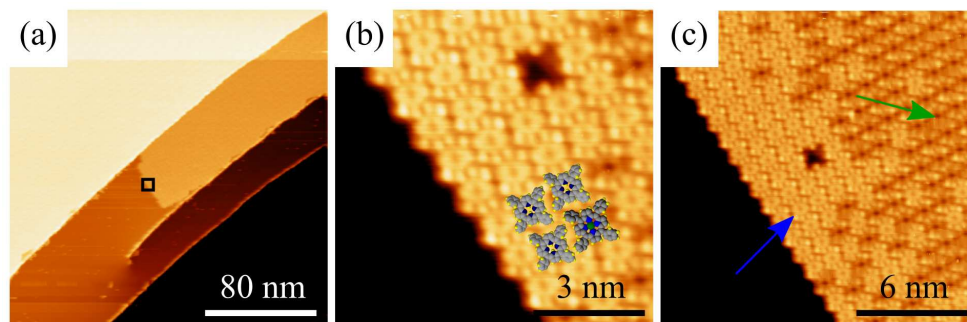
Figure 3.10: (a) 300 nm × 300 nm STM image of 0.5 ML coverage 2H-TPP and Ag-TPP mono-layer. Top terrace is completely covered, second terrace is half-covered in molecules. A 10 nm × 10 nm zoom of the highlighted region is shown in (b). The heterogeneous mixture of Ag-TPP (dark) and 2H-TPP (light) together with the vacancy highlight the ordering. (c) 20 nm × 20 nm scan of the same edge shows a much greater density of 2H-TPP molecules along the edge of the island (blue arrow) compared to the inner part, which is largely occupied by Ag-TPP (blue arrow).

despite only composing 5% of the mixture occupy a very large portion of the observed molecules.

A scan over larger area of the island however shows that further inside the edges, the percentage of 2H-TPP drops close to 5% closer to the center of the adisland (c). This curiosity raises an important point regarding the formation of these SAMs. The growth of the SAM is defined by the kinetics of the constituent molecules, not just the equilibrium between the adsorption and desorption pressures.

The molecules are deposited on the metal surface under UHV conditions from a heated crucible. Before adsorption, they begin in an evenly distributed heterogenous 2H-TPP/Ag-TPP gas phase. Following deposition, the adsorbates order into the observed final state according to the interactions outlined above, thereby forming the SAM. The SAM however shows an uneven distribution of component molecules not reflective of the gas-phase mixture, Figure 3.10 (c) [109, 110].

Now, following adsorption, the strong metal/molecule binding prevents the molecules from desorbing back into the gas phase and re-forming along the edge. The high concentration of 2H-TPP here must therefore come from adsorbed molecules diffusing along the surface onto the edge. As molecules can only diffuse along a free path, this prevents those within the island from diffusing

to the edges. Instead, the edge molecules must be composed of molecules which have diffused from some other edge or free point on the surface. The only explanation for such a strong gradient in population is due to the differences in kinetics between the component molecules [111]. Hence, the time evolution of the adsorbed molecules must be considered in like manner with the energies of the initial and final states [112].

The evolution is a three-step process dependent on the local energetic barriers: the diffusion of the adsorbates along the surface, the initial nucleation of adsorbate islands through inter-molecular bonding, and the exchange of molecules between islands and resulting growth. The first of these is described by the diffusivity, D, a temperature dependent measure of the rate of diffusion of particles between adsorbed sites [112].

It is expected that the barrier acting against this diffusion, the activation energy (E_A), is dependent on the number of bonds between adsorbed particles. This is proportional to both the change in energy as the adsorbate moves between surface sites (diffusion barrier) and the number of inter-molecular bonds (nearest neighbors).

In the case of highly scattered monomers, there are no bonds with neighboring molecules and E_A is only the diffusion barrier Figure 3.11 (i). This description of E_A also applies to any system of two bound molecules (dimer) diffusing together, as the number of nearest molecular neighbors does not change, ii.

As the coverage of particles on the surface increases, adsorbates begin to bond with one another and form adislands. The molecules diffusing away from neighbors must first break the inter-molecular bonds outlined in Chapter 3.2. The barrier acting against a molecule diffusing away from a single neighbor (dissociating) (Figure 3.11 (iii)) is then both the diffusion barrier and the inter-molecular bond energy. In the case of a molecule dissociating from two neighbors, this increase the inter-molecular bond to twice the amount, in the case of three neighbors, three times, etc. This increase in activation energy is reflected in a lowered diffusivity compared to the free monomers above.
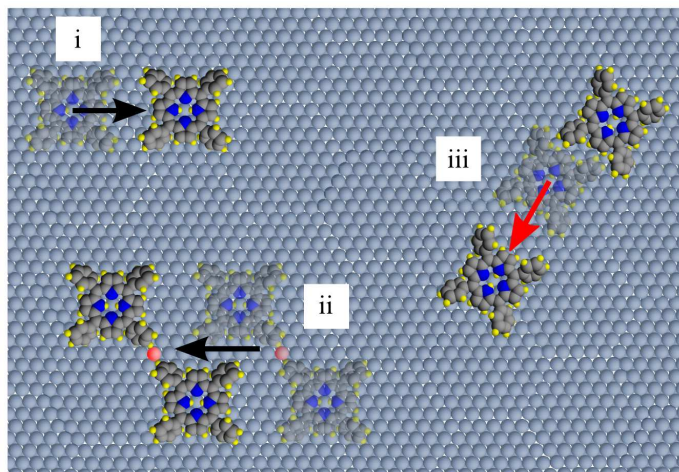
Figure 3.11: A diagram of a collection of 2H-TPP/Ag(111). Diffusion of monomer (i) and dimer (ii) across surface with no detachment. (iii) The dissociation of a dimer - the diffusion of molecules away from bonds with a neighboring molecule.

With greater density, the mean free path between adsorbates is lowered and there is a higher tendency of particles to form bonds, nucleating small islands. Similarly, at lower temperature the diffusion of the molecules is decreased, also lowering the mean free path and resulting in the same phenomenon. The rate of island nucleation can be approximated through a comparison then of the ratio between the rate of incoming adsorbates, R, which reflects the density, and the temperature dependence of D. [111].

Now, while all of this is applicable to both metal adatoms and molecular adsorbates, organic molecules provide additional complexity to this model of diffusion due to the vibrational modes of molecular adsorbates (Chapter 2.2.2). D is dependent not only on the relationship between the activation energies and the temperature, but also the separation between adsorption sites and the parameter known as the hopping frequency, ν, given by,

$$D = \frac{\nu a}{4} \, e^{-E_A/k_B T} \tag{3.3}$$

ν is the frequency of jump attempts made by the adsorbate between sites, typically on the
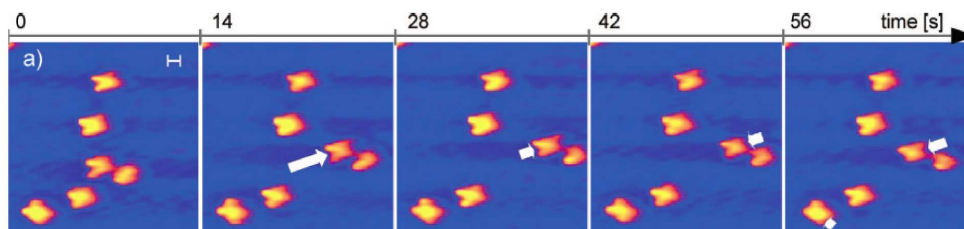
Figure 3.12: 2H-TPyP diffuses across the surface of Cu(111), with a calculable diffusion barrier of 0.96 eV [61].

order of 10^{12} s^{-1} for weakly adsorbed systems [53]. As molecules exhibit modes of vibration, unlike single adatoms, when these vibratoinal modes are in-phase with the direction of motion, this increases the hopping frequency in this direction, and therefore the diffusivity [61].

This has been theorized as an explanation for an observed phenomenon in surface-bound dimers where the diffusivity of *dimers* has been reported to increase by two orders of magnitude in comparison with coadsorbed monomers [113, 61]. The molecules in the dimer do not dissociate, as in Figure 3.11 iii, but rather diffuse in a common direction of motion, Figure 3.11 ii.

This is shown in this example of 2H-TPyP/Cu(111) by Eichberger, Figure 3.12 [61]. Here, a series of fast STM scans were taken over the same set of molecules, monitoring the motion. A single dimer is seen in the bottom half of the image, moving to the right and back towards the center again as the scans proceed. The monomers were found to diffuse with barriers of 0.96 eV, and attempt frequencies on the scale of 10^{12} s^{-1}, the same order as metal adsorbates. Dimers, as illustrated in this set of images, diffused under the same energetic barriers but with a frequency rate on the order of 10^{14} s^{-1}.

The source of this behavior was theorized as due to an in-phase vibrational mode between the molecules of the dimer. As the molecules are bound parallel to one another, the vibrational modes of the individual molecules are changed to create a new mode of vibration in the same direction as the $\langle 111 \rangle$ axes [61]. If this is a common phenomenon, it could be used to design self-assembling systems with nucleation rates orders of magnitude higher than metallic adsorbates.

Chapter 4

Studies of 2D monolayers of tetra phenyl porphyrin

4.1   Introduction

It is the interplay between these interactions that governs the self-assembly and island growth of 2D organic SAMs. Only through sufficient understanding can the self-assembled growth of organic surface systems be controlled through molecular design. As outlined above, this can be done by changing the functional groups, the stochiometric ratio of molecules and other metal atoms, linker clusters, etc., as well as the temperature. The surface/molecule interactions however also limit the mobility of the molecules. This is not only caused by the charge repulsion between adsorbates [114, 10], but, as with metals [115], also by interactions with the electron gas of the metal surface state. A consequence is that the established concepts of solution-based coordination chemistry cannot be applied without appropriate modification. The substrate becomes therefore an important additional parameter to steer the self-assembly process and to control the final architecture of the networks.

An example is shown below, Figure 4.1. Sub-monolayer coverage of 2H-TPP is adsorbed on
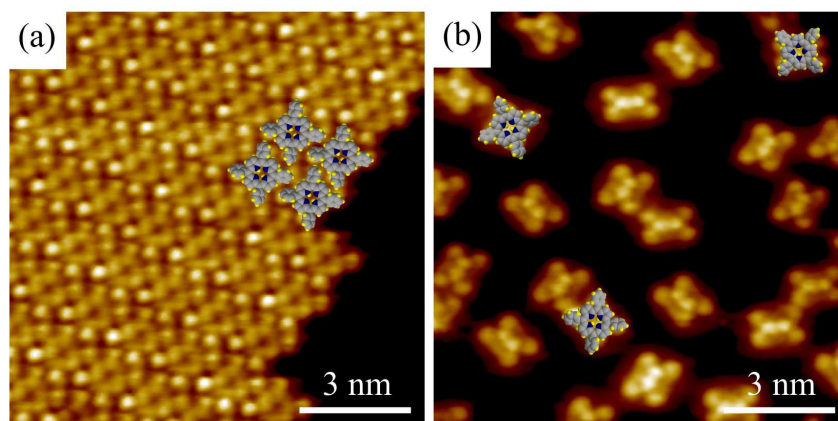
Figure 4.1: 2H-TPP adsorbed on (a) Ag(111) surface and (b) Cu(111) surface.

the surfaces of Ag(111) (a) and Cu(111) (b). The molecules adsorbed on Ag(111) form regular, close-packed square structures [116], with all molecules within the structure oriented according to a repeatable pattern within the architecture. The molecules on Cu(111) instead remain isolated and statistically distributed (b). No supramolecular ordering, self-assembly or nucleated islands are observed, unlike 2H-TPP/Ag(111). By choosing the metal surface, the growth and self-assembly of the molecules can be manipulated.

The molecule studied in this dissertation is *meso*-tetraphenyl porphyrin, a large, 1.4 nm × 1.4 nm molecule composed of the assembly of five aromatic components: a single porphine molecule with four benzene ligands rotated ∼60° out of the porphine plane and bound to the carbons bridging the nitrogen containing pyrrolines Figure 4.2. The geometry, chemical makeup, and metal-organic binding discussed above allow for the porphine macrocycle of the compound to be catalyzed with over 60 different metallic elements for the formation of metal-tetraphenyl porphyrins (M-TPP) Figure 4.2 (c), catalyzed with both transition and rare earth elements. These molecules may also be metallated in UHV conditions post-adsorption on the underlying metal surface [117, 118, 119, 120] including rare-earth metals such as Ce [121]. Photoemission studies have even demonstrated post-metallation chemical reaction of the metals [122, 123]. It has been seen that through this metallation under UHV conditions, the coordinated metal atom is able to
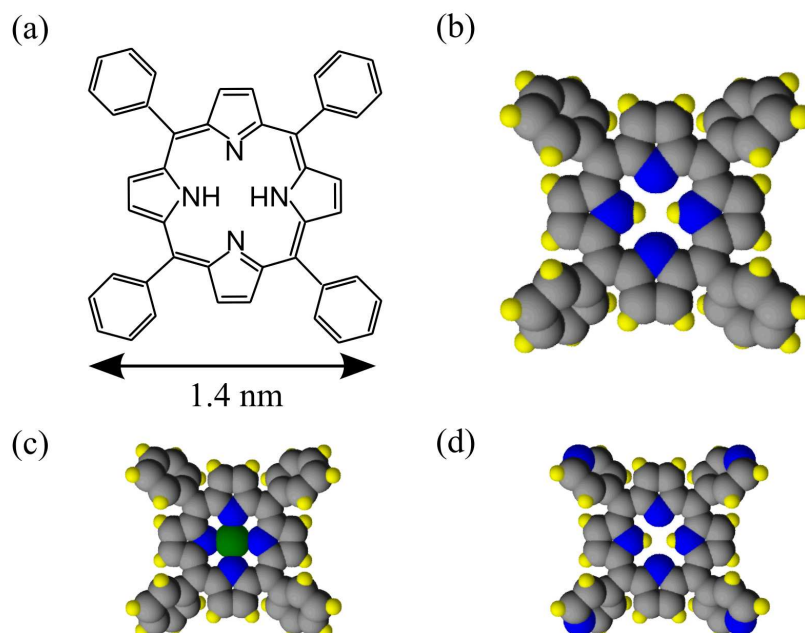
Figure 4.2: (a) Stick diagram of a single tetraphenyl porphyrin molecule, (b) 3D model of molecule, (c) 2H-TPP bound with some metal adatom *M* (green), M-TPP, and (d) *meso*-tetrapyridyl prophyrin

retain a lower oxidation state under much greater ease than if performed using a solution-based wet chemistry synthesis, thereby keeping the electronic and spin properties of interest [124].

The key interest the community has had in this, and the very similar tetra pyridyl porphyirn (TPyP) molecules [125, 126] Figure 4.2 (d), and tetra (3,5-di-tert-butylphenyl) porphyrins (TBPP) [127] molecules, has lead to considerable review over the self-assembly of these molecules and a variety of metallated species. Examination has been carried out at length on the self-assembled ordering and variations in the 2D lattice constant of the SAMs due to the chemical components of the metallated M-TPP species on both the Ag(111) surface [128, 129] and Au(111) surface [130, 131]. In all cases of self-assembly, the TPP molecules in the SAM form compact, well-packed structures, Figure 4.3 (a - b). What has been observed on the noble metal surfaces across both metallated and non-metallated species is that the ordering varies only minimally [131], this occurs across metallated species and chemical reaction [132, 122, 119, 120, 129], and there is
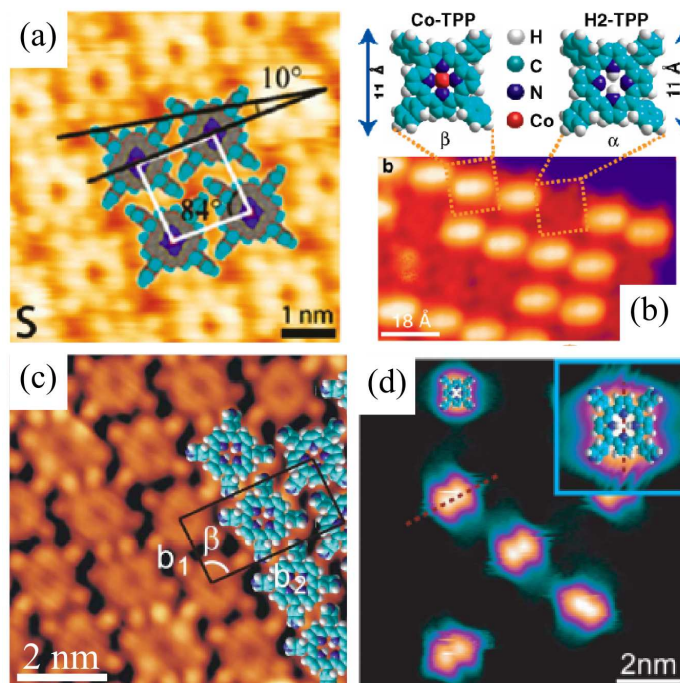
Figure 4.3: (a) NiTPP adsorbed on Au(111) in close-packed structures with molecules oriented similar to that observed in Figure 3.10 (a) [131]. (b) Co-TPP and 2H-TPP adsorbed on Ag(111) surface with the mixed SAM ordered as in Figure 3.10 (a) [121]. (c) 2H-TPyP adsorbed on Ag(111) surface in a close-packed SAM forming bi-column structures [125]. (d) 2H-TPyP on Cu(111) [134]

general intermixing between metallated and non-metallated species within the SAM [121, 133, 130], Figure 4.3 (b).

As can be seen, while the geometries of all post-assembled systems have been properly identified, most research has focused on the chemical nature and electronic properties of the various systems in question. This includes both the general chemical structure of the differing adsorbates as well as how these can be distinguished and vary using local probe methodologies [132, 133, 120, 135]. This makes sense as it is ultimately the application of these qualities for which such excitement has grown over the use of organic SAMs.

While insightful, unfortunately only a small amount of headway has been made on the *dynamics* of the self-assembly process of these chemically adaptable molecules. It is only through understanding the dynamics of the growth processes of these molecules that future systems can
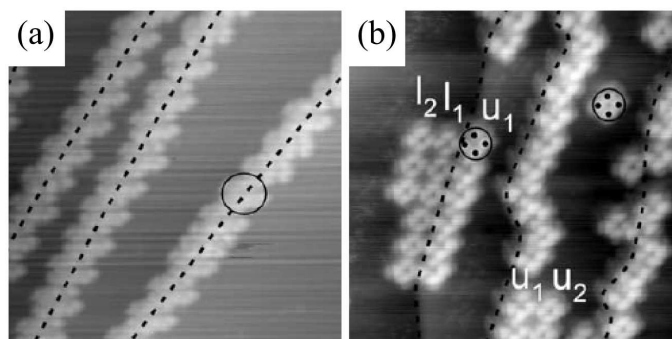
Figure 4.4: (a) 2H-TBPP on Cu(100) form, bridging the step edges of the terrace. (b) Cu-TBPP form along the step-edges, as commonly observed with metal adatoms [136]

be predicted, designed, and engineered *a priori*. As an example, Kamikado *et al.* have shown that both 2H-TBPP and Cu-TBPP preferentially bind to the step-edges of the terrace on Cu(100) [136]. While this might be thought consistent with edge-diffusion versus corner crossing as with metal adatoms, 2H-TBPP preferentially bridge over the step edges while the metallated Cu-TBPP instead form along its edges, Figure 4.4. The former is well known and typifies the behavior observed in inorganic adatoms, whereas the latter is peculiar only to large molecules which have the size to form such bridges. Little more is drawn from this paper and this leaves open the question of how accurately the diffusion mechanics applied to inorganic systems can be applied to such large organic compounds. If it is known that molecules as large as 2H-TBPP bridge the step edge of terraces, does the concept of edge diffusion still apply as with metal/metal surface systems? Furthermore, how, if at all, does the diffusion of these adsorbates along the edges of 2H-TBPP islands within the terrace affect the growth of the island self-assembly?

Recent studies by Buchner *et al.* in the mixed phase analysis of 2H-TPP and Co-TPP on Cu(111) found while Co-TPP remain in self-assembled island structures, as with the other studies of M-TPP on Ag(111) and Au(111), the non-metallated 2H-TPP remain isolated and statistically distributed across the surface [129]. Similar isolation is observed for the 2H-TPyP on Cu(111), with the molecules remaining isolated and evenly distributed across the underlying Cu(111) sur-

face, Figure 4.3 (d) [134]. Upon annealing to higher temperatures, it was observed that the TPyP molecules in this system formed MOCN from interaction of the nitrogen end group of the pyridyl ligand with freed Cu atoms, while no such temperature dependent study was conducted regarding the 2H-TPP/Cu(111) system. Furthermore, it has been seen that isolated 2H-TPyP diffuse across the surface, even after forming dimer pairs with metal linkers [61].

While this isolated pattern of adsorbates is consistent with that seen for self-repulsion between other adsorbed organic species [114, 10], no similar such method of analysis can be conducted on either sample. This is due to the intermixing of the Co-TPP limiting the available surface area 2H-TPP/Cu(111) may migrate into. This is also due to the fact that the metal-ligand bond strength of the Cu linkers on 2H-TPyP/Cu(111) may be large enough to counter act the charge repulsion (Table 3.1).

Porphyrin presents the opportunity to adapt the desired electric and spin properties of a metal atom to the organic system which self-assembles into the geometry desired. Understanding the mechanism of the self-assembly is therefore key to not only expanding our understanding of the self-assembly and growth of organic thin films, but also understanding how this molecule behaves. It is for this reason that the following experiments have been conducted. Because 2H-TPP only interact with neighboring molecules through weak forces such as vdW, this allows the molecule to be studied on systems where the surface interaction is strong enough to prevent such bonds. Whereas the very similar molecule, 2H-TPyP, is able to form strong bonds through dissociated surface atoms of Cu, this prevented study of whether it is a matter of diffusivity, surface deformation, or electrostatic repulsion that inhibited the growth [61].

Due to the increased porphine-surface separation compared to octaethyl porphine [137] and decreased separation compared to TBPP [124], this allows the molecule to interact with the Cu(111) surface due to the extended d_{z^2} orbitals of the Cu atoms, while not interacting with the shielded orbitals of the atoms in the surfaces of Ag(111) and Au(111). Comparison of this system across temperature, coverage, and surface allows for the in-depth study of the basic mechanics of self-

assembly of the weakly bound organic molecule of interest while determining the limiting factors and how they may be overcome without affecting the molecule itself.

In what follows, three published and to-be-published papers investigating the energetic barriers and associated dynamics of 2H-TPP on group 11 metal surfaces, focusing on Ag(111) and Cu(111) are presented. Through the comparison of the ordering behavior, energy levels, and work function measurements across temperature and varied substrate, the chemical interaction between molecule and substrate is explored on a sub-molecular scale. Through this study, the mechanics of the self-assembly and the source of its inhibition is discovered.

Each study addresses a separate topic regarding the problem of the self-ordering of 2H-TPP-surface structures: growth dynamics, intermolecular binding, and inhibition of nucleation. These three topics, in combination, can describe the self-assembly of any surface system in full.

The current difficulty is that most papers and review articles discussing self-ordering treat the individual systems discussed as entirely separate. Due to the uniqueness of each molecule/surface combination, the discussions of surface systems with sub-monolayer coverage are presented much the same way as studies of newly discovered molecules. The geometric properties are presented, the electronic properties are mapped, occasionally theoretical descriptions are given in conjunction with explanation and a study of a new system is later given. In the case of systems lacking self-ordering, connections are infrequently made to similar systems that do.

In the following three papers this is changed. A full description is given of the molecule 2H-TPP on the Ag(111) substrate. On this substrate, it is observed that the molecules form ordered, two-dimensional networks. The geometry of the final, ordered networks does not only reflect the symmetry of the individual molecules but the directionality of the dipolar CH-π interactions. The inter-molecular binding energies are of the same order as those of noble gas adatoms and weakly interacting metals. The observed ordering of the islands is temperature dependent, from nucleation to dissolution. From this it is learned that such organic surface system can be described by the very same growth dynamic formula applied to metal heteroepitaxy.

Those molecules adsorbed on the Cu(111) surface however exhibit no such ordering, across all temperatures, and despite freedom of motion. The inter-molecular separation grows proportionally with available surface area, providing evidence of long-range repulsion between adsorbates. Such a long-range, repulsive interaction can only be due to electrostatic dipole-dipole interactions and the source of this interaction is investigated and determined to be due to a weak surface interaction and not a chemical bond. Work function maps validate the pattern of dipole formation expected from both repulsion of the underlying surface electrons (the pillow effect) and the IDIS models of surface adsorption.

Through addition of single-atom thick layers of Ag on top of the Cu(111) surface, the inter-face interaction is controlled in a repeatable, step-wise manner. Eventually, the self-ordering and electronic properties of the 2H-TPP/Ag(111) system are replicated on the 2H-TPP/Ag/Cu(111) buffer layer system. In this, the source of the repulsive interaction is discovered and matched to existing theoretical predictions. As it is this repulsive interaction which inhibits self-assembly, the inhibition of self-assembly is not only explained, but through its understanding this phenomenon is controlled.

4.2 Temperature dependence of metal-organic heteroepitaxy[*]

Geoffrey Rojas[†], Xumin Chen[†], Donna Kunkel[†], Matthias Bode[‡,§], Axel Enders[†,¶]

Department of Physics, University of Nebraska-Lincoln, Lincoln, NE, 68588

Department of Physics, Universität Würzburg, Würzburg 97074 Germany

Center for Nano Materials, Argonne National Laboratory, Argonne, IL 60439 USA

Center for Nano Materials, Argonne National Laboratory, Argonne, IL, 68588

Abstract

The nucleation and growth of two-dimensional layers of tetra phenyl porphyrin molecules on Ag(111) is studied with variable temperature scanning tunneling microscopy. The organic/metal heteroepitaxy occurs in strict analogy to established principles for metal heteroepitaxy. A hierarchy of energy barriers for the diffusion on terraces and along edges and around corners of adislands is established. The temperature is key to selectively activating those barriers, thus determining the shape of the organic aggregates, from fractal shape at lower temperatures to compact shape at higher temperatures. The energy barrier for the terrace diffusion of porpyrins and the molecule-molecule binding energy were determined to $30\,\mathrm{meV} < E_{terrace} < 60\,\mathrm{meV}$ and $130\,\mathrm{meV} < E_{diss} < 160\,\mathrm{meV}$, respectively, from measurements of island sizes as a function of temperature. This study provides an experimental verification of the validity of current models of epitaxy for the heteroepitaxy of organics and is thus expected to help establish design principles for complex organic / metal hybrid structures.

4.2.1 Introduction

The current interest in ultra thin layers of organic molecules on metal surfaces is fueled by the prospect to be able to synthesize new and improved hybrid materials for applications in next generation electronic devices, catalysis, chemical sensors, and passivation coatings. Many of the useful properties arise from interactions at the metal-organic interface. Their study and exploitation depends on the meticulous fabrication of desired organic structures by precisely controlling the interactions between molecules, following the established principles of supramolecular chemistry. The control parameters for the self-assembled growth of organics are the design of the molecules and their functional groups, the stoichiometric ratio of molecules, atoms and linker clusters, and the temperature. In contrast to solution-based chemistry, the molecular self-assembly on surfaces is limited by the mobility of the adsorbed molecules. The substrate thus becomes an important additional parameter to steer the growth and to control the architecture of the networks [53, 111, 116]. As such, the question about similarities and differences between organics/metals heteroepitaxy and metals/metals heteroepitaxy arises.

It is well established for the heteroepitaxial growth of metals on metal surfaces that the growth can occur either near the thermodynamic equilibrium or far from equilibrium [111]. The growth near thermal equilibrium is often correctly predicted by comparing the surface free energies of the film and substrate interfaces [138], thereby considering the growth as a wetting phenomena. Often though, the growth is far from equilibrium, especially when the deposition rate of atoms or molecules, R, is high, and the diffusivity of adsorbed species, D, is low. The latter is temperature-dependent and determines the average distance an adatom has to travel to nucleate a new aggregate or to attach to an already existing aggregate. If the deposition of molecules is fast compared to their diffusivity, the individual atomistic processes become important and the growth is essentially determined by kinetics, i.e. thermally activated motion in the presence of diffusion barriers. The size and areal density of adlayer islands is dependent on the ratio R/D [139, 53, 110]. As a trend,

a large number of small islands is found at low temperature and high deposition rate, while fewer but larger islands are formed at high temperatures or low deposition rates. Fundamental diffusion processes are diffusion on terraces and over steps, and upon attachment on nucleated aggregates also along adisland edges and across corners. Each of these processes is associated with a characteristic energy barrier. The diffusion across such barriers is thermally activated, with the respective rate depending on the barrier height. The growing aggregates can thus be shaped by selective activation/freezing of certain diffusion processes via the temperature [53, 110, 111].

There are good reasons why these established principles for metal heteroepitaxy may not be applicable to the heteroepitaxy of organics on metal surfaces. Unlike many metal adsorbates, organic molecules are closed-shell systems with energy gaps across the Fermi energy E_F. Usually, interactions between organic molecules and metal surfaces are complex and involve charge donation and back donation, electronic level realignment, static surface dipoles, and other factors [1]. Also given the large size of organic molecules, they often extend over several atomic spacings of the substrate, which makes diffusion barriers on the terraces and at the step edges of the substrate less relevant.

Despite an increasing effort to investigate structure and properties of ultra thin organic layers, the question remains, how accurately can existing models of nucleation and growth be applied? In this article, we will study the growth of 2D layers of hydrogenated tetra phenyl porphyrin molecules (2H-TPP) on Ag(111). Porphyrins have become a model system, and a large number of studies addressing the network formation on various metal substrates, as function of metallization and of functional groups is now available [125, 140, 119, 128, 116, 141, 131]. The 2D networks observed are typically equilibrium structures where the functional groups of the molecules, and not the terrace diffusion, determine the architecture of the networks. We present here a growth study of 2H-TPP as function of temperature, performed with variable temperature scanning tunneling microscopy. It is found that nucleation and growth dominated regimes can be distinguished clearly, and that selective activation of edge diffusion and corner crossing by the growth temper-

ature determine the island's shape. While this is result is well-known for metals and as such not very surprising, the value of this study is that it extends now the validity of those models to organic heteroepitaxial systems.

4.2.2 Experimental Procedure

Our study was conducted under ultrahigh vacuum (UHV) in a multi chamber system comprising all tools required for comprehensive in-situ sample preparation and characterization. Ag(111) single crystals were prepared by repeated cycles of Ar^+ ion sputtering and annealing to 650 K. The 5, 10, 15, 20-tetraphenyl porphine (2H-TPP) molecules, purchased from Frontier Scientific Inc., were deposited by thermal evaporation using a knudsen cell evaporator. The deposition rate was approximately 0.05 monolayers·minute^{-1}, unless specified otherwise. Images were obtained as function of temperature using an Omicron variable temperature scanning tunneling microscope (VT-STM). The deposition of molecules was done directly with the sample resting in the VT-STM sample stage, so that imaging could be done during or directly after deposition and at deposition temperature. Where the deposition continued during scanning, the tip was moved between images to prevent shadowing the sample with the STM tip. Some of the studies presented were performed, using the same substrate and molecules, in a separate UHV system with an Omicron low-temperature scanning tunneling microscope (LT-STM). In such studies, the molecules were deposited at room temperature.

4.2.3 Growth studies with VT-STM

Images of islands of 2H-TPP on Ag(111), taken with scanning tunneling microscopy, are shown in Figure 4.5. Here, the 2H-TPP molecules were deposited and imaged at 300 K. The images show the well-known 2D networks of the 2H-TPP on the terraces of the Ag(111) [116, 128, 131], and the decoration of the substrate step edges [116]. At room temperature, the size and shape of the islands

is time-dependent, due to a constant flux of detachment and attachment of edge molecules between islands. Figure 4.5 (b-c) show the shape of one selected island over a time period of 30 minutes following deposition. Over the entire course of observation, the molecule count of the shown adisland went from 125 attached molecules to 74, with a new smaller island forming above it (not pictured). The molecules are only weakly bound to the surface and are easily dragged around with the tip of the STM, resulting in visible streaks in the images. When the same sample was cooled to 80 K, the size of observed adislands increased dramatically as the result of condensation, Figure 4.5 (d). Long-term observation of the same system at 80 K showed no significant molecule diffusion.
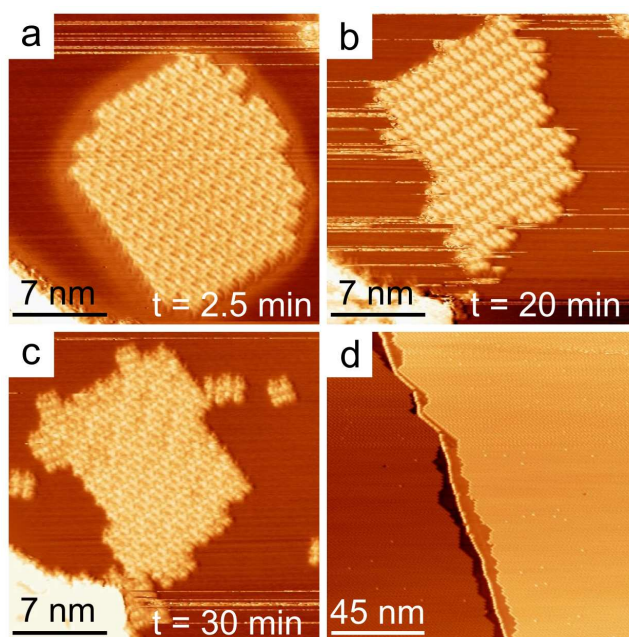
Figure 4.5: (a - c) STM topograph of 2H-TPP/Ag(111) deposited and imaged at room temperature. The images were taken at specified times after deposition of the molecules. Image size: 23 nm × 23 nm. (d) STM topograph of 2H-TPP/Ag(111) deposited at room temperature and imaged at 80 K. Image size: 100 nm × 100 nm.

Next, the island nucleation and growth at low temperatures was studied. The molecules were deposited on the Ag(111) crystal, held at 58 K, and continuously imaged during deposition. In the STM image in Figure 4.6 (a), taken after 10 minutes of deposition, the coverage is $\theta = 0.14$ ML,

and after 30 minutes of deposition, an increased coverage of $\theta = 1.28$ ML was observed, see Figure 4.6 (b). Here, one monolayer corresponds to a coverage of 0.51 molecules·nm^{-2}, as observed in the densely packed 2D networks formed at room temperature as in Figure 4.5 (d). It is apparent from inspection of the STM images that the nucleated adislands are single monolayer in height and show irregular, fractal-like shape. With increasing coverage, the islands develop a ramified shape, and nucleation sets in on top of the islands.
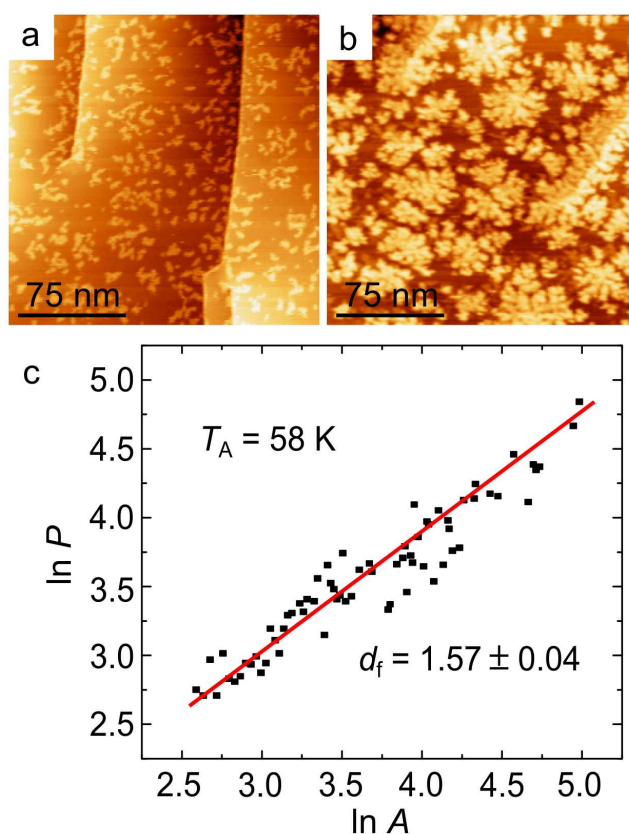
Figure 4.6: STM topograph of 2H-TPP/Ag(111) taken at 58 K after (a) 1 minute of deposition, and (b) 30 minutes of deposition. (c) Plot of the perimeter v. area relationship of 2H-TPP islands at 58 K.

The onset of thermally activated motion was studied by depositing molecules on Ag(111) at approx. 55 K and annealing the sample after deposition to specific annealing temperatures, T_A. STM images were then taken at 80 K, to suppress molecule diffusion during imaging. Character-

istic STM images taken after annealing at different temperatures $T_A < 300$ K are summarized in Figure 4.7. No significant change in island size and shape with respect to the as-grown morphology was observed upon annealing up to $T_A = 110$ K. The islands remained as small, narrow, irregular structures and were typically of 2 ML height. At $T_A = 110 - 130$ K, the double layer islands began to disappear, and islands showed increased diameter. No 2 ML islands were observed above 150 K, indicating the diffusion of all molecules in the second layer over the organic island edges and on to the Ag(111) surface. The average area of the adislands continued to grow with increasing temperature up to 250 K, and the larger islands exhibited a rather compact shape.
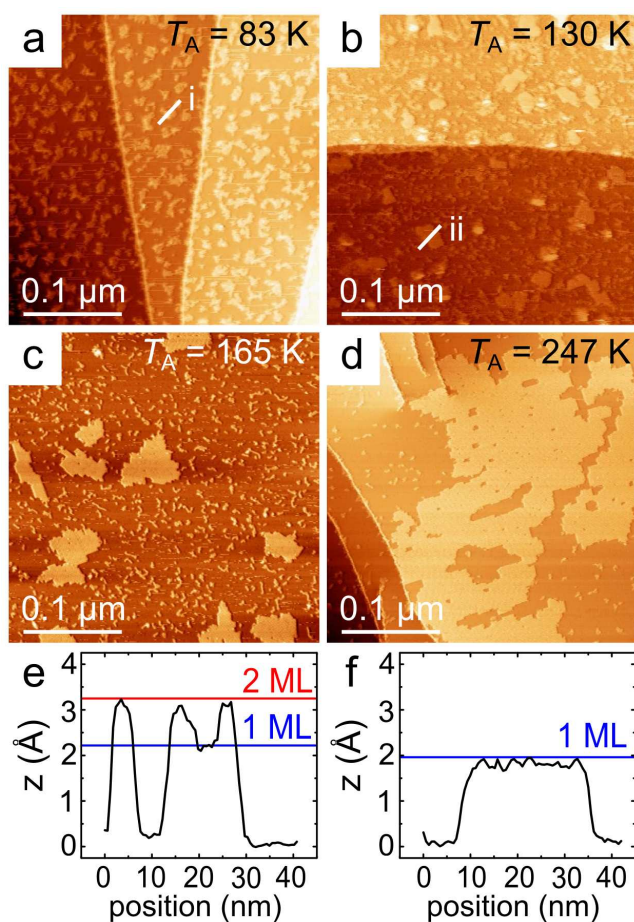
Figure 4.7: (a - d) STM topographs of 2H-TPP/Ag(111) taken after annealing the system to the specified annealing temperatures. Height profiles at 83 K (e) and 130 K (f) show relative heights of 1 ML and 2 ML adislands. All data taken at 80 K.

4.2.4   Discussion

The nucleation and growth of 2D organic layers, as observed on the example of 2H-TPP molecules on Ag(111), shows striking similarities to metal heteroepitaxy. As has been demonstrated, the substrate temperature is a key parameter to control the growth. We find here for 2H-TPP a comparatively high density of rather small islands of fractal shape at temperatures below 100 K, while at higher temperature large and compact islands are formed.

The found fractal shape of the islands is evidence of activated diffusion of the molecules on the substrate terraces and along island edges after attachment, but crossing the corners at the adisland perimeter is associated with a higher barrier and thus not activated at lower temperature. The fractal shape of the islands can be quantified in terms of their fractal dimension, d_f, which relates the scaling of the mass of an object with its size. A common approach to determine the fractal dimension is to calculate the ratio of island perimeter, P, to island area, A of the islands from the STM images. Island perimeter and area are related as

$$P \propto A^{d_f/2}. \tag{4.1}$$

As structures becomes more compact in form, their P/A ratio grows smaller. The d_f is calculated from the slope in the plot of the logarithms of perimeter versus area, which are determined from the STM images, Figure 4.6. From the data in Figure 4.7, the fractal dimension is determined to $d_f = 1.54 \pm 0.03$ at the temperature of 58 kelvins. This value appears to be similar to the fractal dimension of metallic nucleates that lack the energy to cross corner boundaries [142, 143].

The temperature dependence of the fractal dimension is plotted in Figure 4.8. Clearly, the d_f remains constant until the annealing temperature reaches $T_A \sim 100\ K$. Further increasing the sample temperature causes a significant reduction of the fractal dimension to $d_f = 1.21 \pm 0.08$ at $T_A \sim 130$ K, and further annealing up to room temperature does not change the value of d_f further. A phenomenological fit of the data to a sigmoidal function was used to approximate the critical

temperature, determined from this plot to $T_c = 125 \pm 7$ K. This sudden decrease in d_f is related with the observed transition from fractal to compact island shape. This, too, is in analogy to the similar transitions in metallic islands, such as those reported for Au/Ru(001) [144] and Ag/Pt(111) [145], where this compactification was ascribed to the activation of corner crossing of atoms.

In this present study we find that terrace diffusion, associated with an energy barrier $E_{terrace}$, occurs even at the lowest temperature studied (58 K). The onset of of corner crossing, observed at approximately 100 - 110 K, coincides with the gradual disappearance of islands of double layer height, and with the onset of island ripening (Figure 4.7). For instance, while at lowest temperatures studied the occurrence of double layer islands is near 100%, at $T_A \simeq 109$ K only about 50% of all islands are of monolayer height. It is believed that aggregates in the second layer must dissociate first, before diffusing as monomers on the surface of single monolayer islands and descending across the adisland edge. This implies that the barriers for corner crossing, E_c, molecule-molecule dissociation, E_{diss}, and step edge descent, E_s, are all of similar magnitude.

The growth of some of the island on the expense of smaller islands is the familiar Ostwald
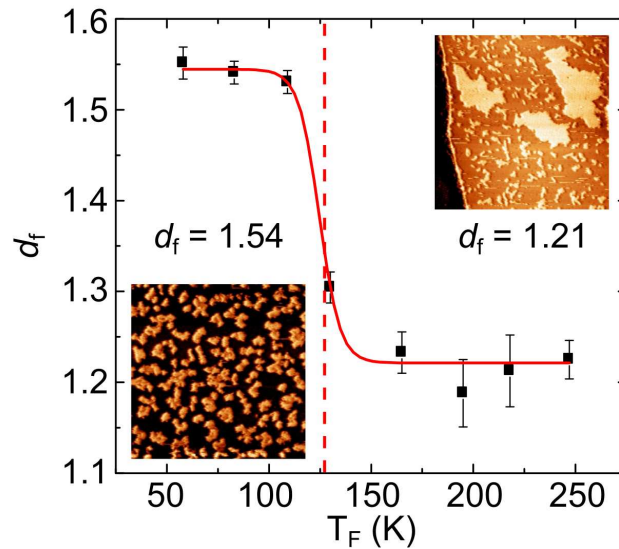

Figure 4.8: Calculated d_f as a function of temperature. Red solid line: sigmoidal function with $T_0 = 124 \pm 2$ K. Insets: characteristic STM images for high and low T_A reflecting the change in d_f.

ripening: adsorbates on the island edges begin to dissociate with increasing frequency and diffuse away until attaching to neighboring larger islands [146]. The ripening of expitaxial systems is well established and described as a growth rate, K, of a circular island over time,

$$K = \frac{\Delta r^3}{\Delta t} = \frac{K_0}{k_B T} e^{-(E_A/k_B T)}, \tag{4.2}$$

where K_0 is a measure of the surface energy of islands and availability of free molecules [146, 138, 147], the k_B is the Boltzmann constant, and the activation energy here is the energy required for a molecule to dissociate from an existant island and diffuse across the surface [148, 139, 149, 150],

$$E_A = nE_{diss} + E_{terrace} \tag{4.3}$$

The n specifies the critical number of nearest neighbors to start island nucleation, taken to be 1 from the very low coverage data at 58 K (not shown). Both the island area and the growth rate were determined from the STM images and are plotted as functions of temperature in Figure 4.9. The islands become unstable near 300 K, seen in Figure 4.5, explaining the kink in the trend in A at that temperature in Figure 4.9. Upon cooling of the sample down to 80 K, the dissociation rates decrease, the islands become stable. The K was determined by comparing the size of identical islands in consecutively taken STM images, separated by time intervals Δt. The sharp increase in the island area at a temperature of 110 K is consistent with the onset of the change in the fractal dimension of the islands (Figure 4.9 (a)), step edge descent and compactification of the islands. The intersection of the trend lines for the static and ripening regimes (i and ii respectively) is seen located at the same critical temperature from the fractal analysis, 120 K. This is concurrent with the expectation that the ripening of the system is controlled by the energetic barriers acting against dissociation from the adislands.

The fit over the growth rate of the adislands, K, with both K_0 and E_A held as free parameters, shown in Figure 4.9 (b) provides an estimate of the activation barrier, $E_A = 194 \pm 27$ meV. While
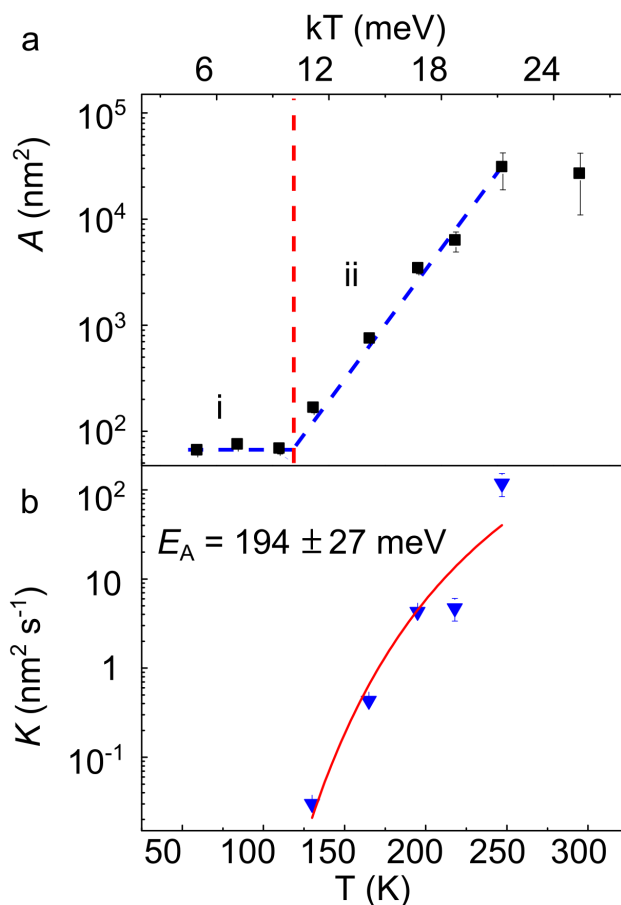
Figure 4.9: (a) Temperature dependence of the mean island area. Exponential growth occurs in the range labelled (ii) between 100 K - 250 K. The onset of growth is at ∼125 K (red dashed line). (b) Island growth rate K, with fit to equation (2).

noticeably weaker than the typical terrace diffusion barriers of many metal-metal systems [145, 151, 152] with some on the order of 800 meV [153], it is consistent in magnitude with the activation energy of the more weakly adsorbed systems such as Pt/Pt(111) (260 meV) [154], Ag/Pt(111) (320 meV) [155] and the weakly-bound organic-metal system of PTCDA/Ag (130 meV) [156].

The critical temperature where the system crosses from the static nucleation regime to the ripening regime is clearly near 124 K from Figure 4.9. This allows for the estimation of $E_{terrace}$ at $k_B T \ll E_{terrace}$ using the same nucleation model of metal adsorbates and the low temperature data

in Figure 4.6 [157] the nucleation density of dimers is,

$$n_x = \frac{1}{4}\left(\frac{4\,R}{\nu\,a^2}\right)^{1/3} e^{(E_{terrace}/3k_BT)} \tag{4.4}$$

Applying the observed deposition rate $R = 4.97 \times 10^{-4}$ molecules$\cdot$nm^2 $\cdot$s^{-1} in this experiment, the nucleation density of $n_x = 4.9 \times 10^{-4}$ islands$\cdot$lattice site^{-1}, and the lattice constant for the Ag(111) surface ($a = 2.88$ Å) yields $E_{terrace}$ of 30 meV to 60 meV. The variance is the result of uncertainty in the hopping frequency, which are expected to be in the range between $10^9 < \nu < 10^{12}$. This leaves a dissociation barrier between ~ 130 meV and 160 meV for 2H-TPP/Ag(111). While an approximation, this is in reasonable agreement with the diffusion barrier for 2H-TPP from first-principle calculations [116] and of the same order of magnitude as weakly bound metal/metal systems with similar attempt frequencies [157].

4.2.5 Conclusions

The nucleation and growth of 2D films of 2H-TPP on Ag(111) occurs in analogy to metal heteroepitaxy. It was shown that existing models accurately describe the surface kinetics of the 2H-TPP / Ag(111) system, despite the incommensurate matching of the film structure with the substrate lattice, the large size of the molecules in comparison with the substrate lattice spacing, weak physisorbed interaction, and van der Waals intermolecular bonding, which all distinguishes organic adsorbates from metallic species. An important reason for this good agreement is that the energy barrier for terrace diffusion is determined by the landscape of the binding energy for the molecules, which has the same symmetry and periodicity as the potential energy landscape for single adatom diffusion, namely the surface structure of the substrate. However, the effective barrier height is expected to be smaller for the molecules compared to single atoms, due to the lateral size of the molecules, expanding over several substrate lattice spacings, and the increased bond length to the substrate. This is exactly reflected in our measured energy barrier for terrace diffusion The

same hierarchy of diffusion barriers that determines the shape of metallic aggregates is also governing the shape of the organic aggregates: with increasing temperature, terrace diffusion, edge diffusion, corner crossing and dissociation are successively activated and cause a change in the island shape and size, from small and fractal to large and compact. This experimental verification of the validity of current models of epitaxy is thus expected to help establishing design principles for complex organic/metal hybrid structures.

acknowledgement

4.3   Non-metallated tetraphenyl-porphyrin on noble metal substrates[†]

Geoffrey Rojas[†], Xumin Chen[†], Cameron Bravo[†], Ji-Hyun Kim[‡], Jae-Sung Kim[‡], Xie Jiao[†], Peter A. Dowben[†], Yi Gao[§], Xiao Cheng Zeng[§], Wonyoung Choe[§], Axel Enders[†,¶]

Department of Physics, University of Nebraska-Lincoln, Lincoln, NE, 68588

Department of Physics, Sookmyung Women's University, 52 Hyochangwon-gil, Yongsan-gu, Seoul, 140-741, Korea

Department of Chemistry, University of Nebraska-Lincoln, Lincoln, NE, 68588

Abstract

The structure-electronic structure relationship of nonmetalated meso-tetraphenyl porphyrin (2H-TPP) on the (111) surfaces of Ag, Cu, and Au was studied with a combination of scanning tunneling microscopy, photoelectron spectroscopy, and density functional theory. We observe that the molecules form a 2D network on Ag(111), driven by attractive intermolecular interactions, while the surface migration barriers are comparatively small and the charge transfer to the adsorbed molecules is minimal. This is in contrast to a significant charge transfer observed in 2H-TPP/Cu(111), resulting in repulsive forces between the molecules that prevent molecular adlayer network formation. It is shown that the limiting factor in formation of selforganized networks is the nature of the frontier orbital overlap and the adsorbate-interface electron transfer. Further, the

electronic structure, most notably the HOMO-LUMO splitting, are found to be dependent on the substrate as well. The comparison of the results in this article with published work on similar porphyrins suggests that the molecule-substrate interaction strength is determined by the molecule's metalation, and not so much by the ligands.

4.3.1 Introduction

The self-assembly of porphyrins on well-defined surfaces is attracting considerable interest because it promises to create surface patterns with nanometer dimension that exhibit specific electronic, sensoric, optic or catalytic functionality [158, 159, 160], or even interesting magnetic properties [6, 161]. The ability of porphyrin to show self-organization and to accommodate metal atoms in their macrocycle is exploited, for instance, to form metal-organic frameworks or adsorbed layers for catalysis [122, 162, 163, 164]. The self-assembly is mainly driven by non-covalent metal-organic coordination interactions, which is well-known and important in solution-based 3D supramolecular chemistry [106, 103, 104, 165, 105, 166].

Porphyrin molecules have been adsorbed onto surfaces to form supramolecular networks from solution [167, 168, 169, 170], electrochemically [171, 172] or by thermal evaporation under vacuum conditions [173, 174, 175, 125, 176, 136, 177]. While there is a rich literature on the electronic structure of these adsorbates, the surface adlayer structures have also been characterized with scanning force microscopy, scanning tunneling microscopy, or X-ray absorption near-edge structure analysis [79]. The rationale of such experiments on 2D structures has been to study the long-range interactions that determine the self-assembly processes. It has been demonstrated that the bottom-up fabrication of highly organized porphyrin layers, as well as of porphyrin-based multicomponent molecular entities, depends on the interplay of molecule-molecule and substrate-molecule interactions. Molecule-substrate interactions will set limits to the mobility of the adsorbed molecules and may alter the electronic structure of the absorbed molecules, or the electronic states at the sur-

faces may become locally perturbed by the adsorbate [120]. A consequence is that the established concepts of solution-based coordination chemistry cannot be applied without appropriate modification. The substrate thus becomes an additional parameter to control the adsorption energy of the molecules and, hence, their diffusivity at surfaces. An intriguing demonstration of this effect is the self-assembly of porphyrins, which are decoupled from their metal substrate by insulating NaCl layers of varying thickness [174]. The interaction was shown to be dependent on the NaCl layers and the thicker the NaCl the weaker the interaction and the more delayed the onset of network formation. The occupation of the center ring of the porphyrin may affect the molecular adsorption at surfaces. As an example, free-base or Cu-incorporated porphyrin molecules show different arrangements along step edges on Cu(100) surfaces. While the 2H-TPP bridge over the step edges, Cu-TBPP rather sit on either side of step edges [136]. In contrast, no differene in the network architecutre was found for differently metalated TPP on Ag(111) [178]. Such a subtle dependence of adsorption site on metal incorporation, if fully understood, may become useful to control the self-assembly or the properties of the molecules on surfaces.

The goal of the present work is to investigate the competition between non-covalent intermolecular interactions and molecule-substrate interactions for 2H-TPP on Ag(111), Cu(111), and Au(111) and to establish the structure-properties relationship and its dependence on interactions with the supporting substrate.

4.3.2 Experimental

Ag(111) and Cu(111) single crystals of purity $> 99.999\%$ were prepared by repeated cycles of Ar^+ ion sputtering and annealing at temperatures of 850 and 800 K respectively for multiple cycles in ultrahigh vacuum (UHV) conditions ($< 1 \times 10^{-10}$ mBar). The substrate's cleanliness was checked by STM at 80 K before deposition of organic material, as well as by photoemission.

The 5, 10, 15, 20-tetraphenyl 21H, 23H, porphine (2H-TPP) was purchased from Frontier

Scientific (purity $> 97\%$) and used without further modification. Molecules were deposited by evaporation using a homebuilt Knudsen Cell evaporator. Molecules were evaporated at a rate of approx. 0.05 ML/min at crucible temperatures of appr oximately 500 K. Coverages were initially limited to approximately $\Theta = 0.01$ ML, where a monolayer (ML) is defined as coverages of approximately 5.1×10^{13} molecules·cm^{-2}, and gradually increased by successive evaporation cycles as needed. For a comparison of molecular adsorption, the 2H-TPP adlayers were studied after evaporation onto Ag(111) and Cu(111) under identical growth conditions.

Samples were immediately transferred in situ to an adjoining chamber for scanning tunneling microscopy (STM) measurements. Image data were obtained under constant current mode using an Omicron Nanotechnology low temperature STM (LT STM) with a W tip at 80 K and pressures of low 10^{-11} mBar. Combined photoemission (UPS) and inverse photoemission spectra (IPES) were taken in a separate UHV system using the same single crystal substrates and evaporators. In all spectroscopy measurements, the binding energies are referenced with respect to the Fermi edge of the substrates in close contact with the sample surface. The IPES were obtained by using variable energy electrons incident along the sample surface normal while measuring the emitted photons at a fixed energy (9.7 eV) using a Geiger-Müller detector. The instrumental linewidth is 400 meV, as described elsewhere [179]. The angle integrated photoemission (UPS) studies were carried out using a helium lamp at $hv = 21.2$ eV (He I) and a Phi hemispherical electron analyzer with an angular acceptance of $\pm 10°$ or more, as also described elsewhere [179].

Calculations were performed using density functional theory (DFT) utilizing the generalized-gradient approximation (GGA-DFT) HCTH functional [180, 181, 182]. The double numerical polarized basis sets (DNP) with the semicore pseudo potentials were applied for all atoms, including Ag, C, N, and H atoms [183, 184]. A 2-layer 10×10 silver slab was used to simulate the Ag(111) surface substrate. In addition, a layer with 10×4 Ag(111) surface was placed on top of the slab to simulate the step-edge effects. In order to reduce the computational cost, the substrate was frozen while the 2H-TPP was fully relaxed. All calculations were performed by using the

DMol^3 software package [183, 184].

4.3.3 Growth studies with STM

4.3.3.1 2H-TPP on Ag(111)

The 2H-TPP adlayers were studied after evaporation onto Ag(111) and Cu(111) under identical growth conditions. First, submonolayer aliquots of the 2H-TPP molecules were evaporated onto a Ag(111) substrate at 300 K. The substrate was subsequently cooled to liquid nitrogen temperatures ($T = 77$ K) for STM studies. For very low 2H-TPP coverage, ($\Theta < 0.01$ ML), molecules are exclusively observed at the substrate step edges, while nothing is seen on the terraces. Higher resolution STM images, as in Figure 4.10 (a), show that those 2H-TPP molecules straddle the step edges, with the phenyl ligands oriented with an angle of approximately ϕ 21° relative to the boundary of the step-edge. All observed step-edge phase molecules sit across the Ag(111) step-edges in apparently identical geometries. These molecules are not seen to engage in any lateral motion even over the period of several hours. Increasing the 2H-TPP coverage resulted in an increase of the step-edge occupancy, until every step edge was fully occupied.

Molecules nucleated into clusters on the terraces only after complete occupation of the step-edges, resulting in ordered two dimensional networks as those seen in Figure 4.10 (b - c). Clearly visible in this figure is the coexistence of the step-edge phase [136] with extended 2D networks of 2H-TPP at a coverage of ($\Theta \simeq 0.5$ ML), while (c) provides a detailed view of the molecular arrangement in the network. The molecules are found to order in tetragonal unit cells of length a = 13.(8) Å, and to be rotated by 16° relative to the axis of the network (Figure 4.10 (d)). Similar 2D arrangement can be found in bulk phases of TPP molecules incorporated with various metals such as Ti, V, Cr, Fe, Co, Cu, Zn, Ru, Mg, Sn, and Ge [185, 186, 187]. The tetragonal unit cell parameter *a* obtained from X-ray single crystal diffraction of these phases ranges from 13.3 Å to 13.8 Å [185, 186, 187], comparable to the same parameter from our surface pattern. Interestingly, free-base
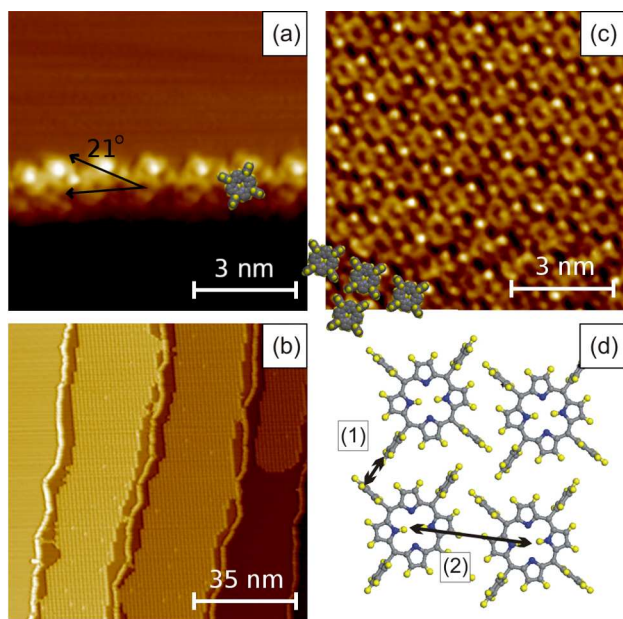
Figure 4.10: STM images of 2H-TPP molecules adsorbed on Ag(111). (a) $\Theta < 0.01$ ML, all observed molecules located straddling step edges. (b) Molecules adsorbed at $\Theta \simeq 0.5$ ML, (c) Close up of molecules on terraces from (b) showing the relative orientation of the molecules. (d) Schematic illustration of measured intermolecular distances for (1) CH-π interaction at 3.9(3) Å and (2) unit cell dimension of 13.(9) Å. All images taken at I = 0.8 nA, V_{Gap} = -0.90 nA.

2H-TPP molecules in bulk phase do not form this observed tetragonal 2D pattern [185, 186, 187]. The value of the CH-π spacing of 3.9(3) Å, found in Figure 4.10 (d), was again comparable to the tetragonal phase of metallated TPP bulk phases.

The orientation of the adsorbed molecules shows a clear influence of the underlying substrate crystallography, as we found three characteristic domains with main directions separated by roughly $60°$, following Ag(111) substrate symmetry.

We conclude from the STM studies that 2H-TPP is highly mobile on Ag(111) at 300 K except at step-edges, with a mean diffusion length significantly larger than the mean terrace width of our substrate. The substrate step-edges, however, provide efficient pinning sites for the porphyrin molecules. The 2D network formation on the terrace is mainly driven by molecule-molecule interaction while the interaction between the molecules substrate the substrate, specifically the migra-

tion barriers, is comparatively weak.

The same arrangement of molecules has been reported for 2H-TPP on the same substrate, as well as on Au(111) [126, 178, 119]. The geometry of the molecules and the limitations imposed by multiple interactions with neighboring molecules, including potential CH-π interactions between phenyl ligands and C-H pairs on neighboring macrocycles, determines the arrangements of molecules at surfaces, has, for example, been suggested in ref [178]. Calculations were performed to further examine these interactions and will be discussed later.

4.3.3.2   2H-TPP on Cu(111)

2H-TPP molecules were evaporated onto Cu(111) under conditions identical to the 2H-TPP/Ag(111) system, as described in the previous section. STM images of sub-monolayer coverages of 2H-TPP on Cu(111), taken at 77 K, are summarized in Figure 4.11. The molecules were not observed to form 2D networks on the Cu substrate, unlike the Ag case. Rather, they tend to be randomly distributed across the terraces at the substrate surface and remain isolated from neighboring molecules. No tendency towards step decoration was observed, as seen in Figure 4.10 (a). However, the molecules appear to be oriented along the principal crystallographic directions of the underlying surface structure, as concluded from the generally observed angle of $120°$ between the major axes of any two closely adjacent molecules.

Observation of the molecules over significant lengths of time showed no lateral motion of the molecules over the substrate, contrary to what was seen for terrace-adsorbed molecules on Ag(111). Furthermore, the molecules on Cu(111) appear topologically distinct from the same molecular species adsorbed on the Ag(111). Under identical scanning conditions, the molecules appear with a raised center and 2-fold symmetry on Cu as seen for metalated species [188], while on Ag they appear as ring-like structures with dark centers and clearly resolved arms. However, the appearance of the molecules is dependent on the bias voltage during the STM experiment, as a comparison of Figure 4.11, panels a and b, shows. At sufficiently low bias voltage, a ring
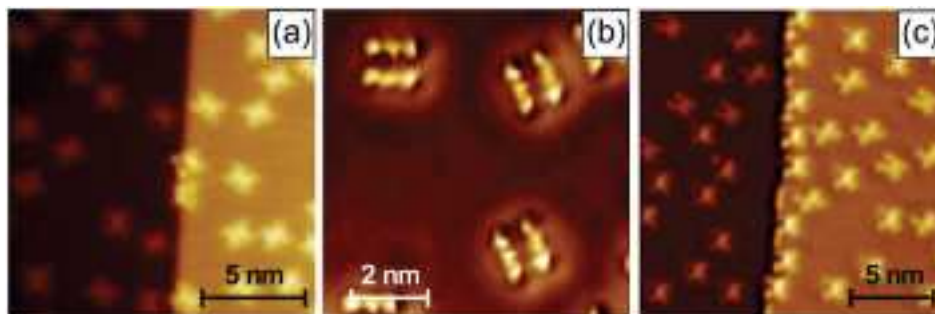
Figure 4.11: (a) STM images of 2H-TPP chemisorbed on a cleaned Cu(111) substrate at T = 300 K and taken at V = -0.8 V with a tunneling current of I = 0.90 nA, (b) a close-up image of the molecule taken at V = +0.4 V and I = 0.8 nA, and (c) after annealing to T = 350 K taken with bias voltage of V = -1.0 V and I = 1.4 nA.

becomes visible in the substrate in the vicinity of chemisorbed molecules (Figure 4.11 (b)). This ring is ascribed to the formation of a surface dipole at the molecule site by drawing electrons from the substrate, leaving the molecules negatively charged. This surface induced dipole, along with greatly increased migration barrier for Cu(111) [61] seems to be related to the absence of self-assembled ordered structures of 2H-TPP on Cu(111).

In an attempt to overcome the diffusion barriers, the molecule-substrate system was annealed to higher temperatures (Figure 4.11 (c)). Following moderate annealing to 350 K for 2 minutes, the molecules were seen to partially decorate the step edge, shown in Figure 4.11 (c). The step-edge occupancy was observed to become complete only after all further annealing to 450 K. The molecules occupying the step-edges in the 2H-TPP/Cu(111) remained seated at the top of the step-edge on the terrace and aligned with the axis of the molecule parallel with the step-edge boundary. No bridging of the step-edges, similar to 2H-TPP/Ag(111), was observed. Despite this observed motion on the terraces, the 2H-TPP molecules did not exhibit any 2D lateral organization on the Cu(111) terraces for all annealing temperatures studied up to 450 K.

4.3.4 Photoelectron Spectroscopy

Combined photoemission and inverse photoemission spectra have been taken for sub-monolayer, monolayer, and multilayer coverages of 2H-TPP on a variety of noble metal substrates. The goal was to correlate the occupied and unoccupied electronic states of the molecules in contact with the metal surfaces with the observed structures. All spectra obtained, together with spectra from the pristine substrates are summarized in Figure 4.12.

Features resulting from the occupied and unoccupied molecular orbitals were clearly observed at all coverages for the Cu(111) and Au(111) systems (Figure 4.12 (b - c)) in the combined photoemission and inverse photoemission. In contrast, peaks due to the molecular orbitals are difficult to distinguish in the occupied states at low 2H-TPP coverages on Ag(111) (Figure 4.12 (a)). All the photoemission spectra show a rapid decrease in those peaks of the underlying substrates with increasing molecule coverage. The generally good agreement of the low coverage combined photoemission and inverse photoemission spectra of 2H-TPP on Cu(111) and Au(111) is remarkable, and indicates a planar adsorption geometry. The absence of clear states at low coverages for 2H-TPP on Ag(111) is attributed to the coexistence of different adsorption geometries as observed with STM, and will be discussed later.

At greater thicknesses, features from the molecules become resolved also on Ag(111) (Figure 4.13). Similarities of the electronic structure in 2H-TPP films are apparent for all three substrates studied. Those features are also in good agreement with the calculated spectra, also shown at the bottom of Figure 4.13. The calculated spectrum is based on simplistic single molecule semiempirical method NDO-PM3 model calculations based on Hartree-Fock formalism, neglecting differential diatomic overlap and assuming a parametric model number of 3, all performed using SPARTAN 8.0 [189]. Geometry optimization of the molecule was performed by obtaining the lowest restricted Hartree-Fock energy states. The calculated density of states (DOS) shown was obtained by applying equal Gaussian envelopes of 1 eV full width half-maximum to each

Table 4.1: Orbitals and Energies of a single 2H-TPP molecule. Calculated values are from PM3 calcuations in SPARTAN, Cu, Ag, Au are from 8 ML samples on the respective substrates.

	Calcuated	Cu	Ag	Au
HOMO -1 (eV)	-2.73	-4.10	-4.30	-4.10
HOMO (eV)	-2.37	-1.90	-1.90	-1.90
LUMO (eV)	2.63	2.10	2.10	1.00
LUMO +1 (eV)	2.82			2.10
Gap (eV)	5.00	4.00	4.00	2.90
Radius (Å)		1.45	1.65	1.74

molecular orbital and then summing to account for the solid state broadening in photoemission. This model density of states calculation was rigidly shifted in energy, largely to account for the influence of work functions on the orbital energies, and no corrections were made for molecular interactions and final state effects.

Photoemission and inverse photoemission are final state spectroscopies, and the HOMO-LUMO gap has been estimated from the vertical energies, with corrections included for the measured instrumental line widths. The combined photoemission and inverse photoemission provides an estimate of the HOMO-LUMO gap of 4.00 to 2.90 eV, depending on substrate, as summarized in Table 4.3.4. This means the HOMO-LUMO gap of a thin film is strongly dependent on the underlying substrate, showing a difference as large as 25%. We further note that the HOMO-LUMO gap predicted by the ground state theory is larger than that measured, which is unusual. The observed HOMO-LUMO gaps for the 2H-TPP/Ag(111) and 2H-TPP/Cu(111) systems differ from those reported for bulk samples [190] in that they are significantly larger. A splitting of the LUMO state is seen for the 2H-TPP/Au(111) system, and weakly also for the 2H-TPP/Ag(111) system. Such splitting indicate either strong intermolecular or substrate interactions, and is in fact consistent with the close packed 2H-TPP on Ag(111), as discussed later. No such splitting is seen for the Cu(111).
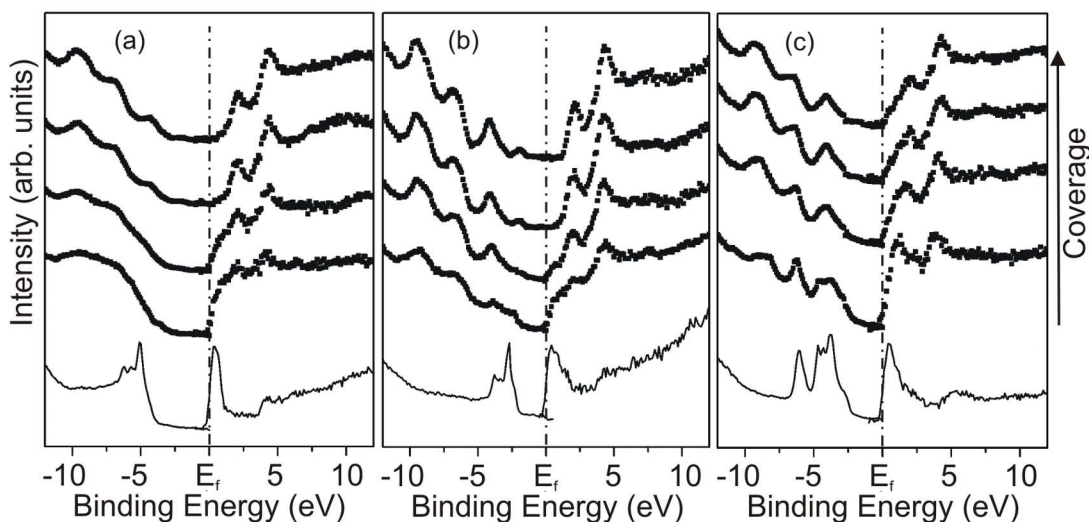
Figure 4.12: Coverage dependant photoemission and inverse photoemission spectra (symbols) of metal-free porphyrin (2H-TPP) adsorbed at 300 K in coverages (from bottom to top) of $\simeq$ 0.5 ML, 1 ML, 3 ML, and 8 ML on (a) Ag(111), (b) Cu(111), and (c) Au(111). The bottom thin line shows the spectra of the pristince substrates as reference.

4.3.5 Density Functional Theory

Calculations of molecules and dimers of 2H-TPP on Ag(111) were performed in order to gauge the effect of molecule-molecule and molecule-substrate interactions, and their influence on the aggregation of molecules at the surface. It is known that traditional DFT methods often cannot reproduce the weak interactions qualitatively and quantitatively due to the lack of dispersion [191]. In order to test the applicability of the HCTH functional in this system, we examined the binding energy of a benzene dimer. Binding energies for the T-shaped and sandwich benzene dimer of 0.04 eV and 0.02 eV were obtained, respectively. Although these values are much smaller than the results based on high level CCSD(T) calculations [192], it gives a correct qualitative description of van der Waals interactions, which means the HCTH functional could be used to evaluate the σ-π and π-π interactions.

With our calculations we optimized a 2H-TPP monomer on a Ag terrace and on a step edge, as well as free 2H-TPP dimers. On the Ag(111) surface, the molecules were found to exhibit little
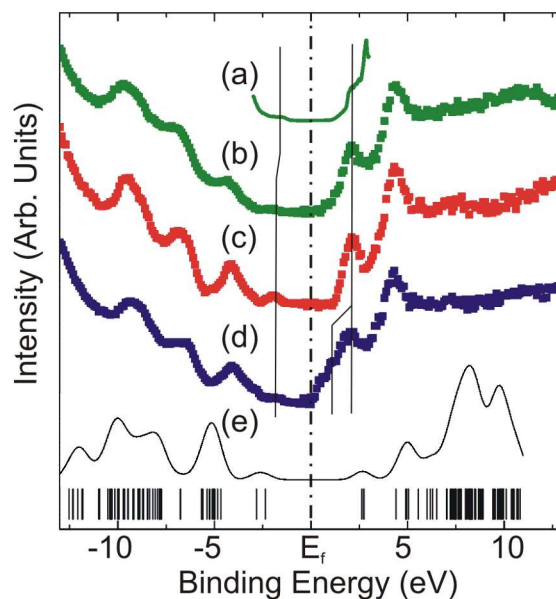
Figure 4.13: Comparison of scanning tunneling spectra of 2H-TPP on Ag(111) at 77 K, and photoemission and inverse photoemission spectra of thick films of 2H-TPP (nominally 5 ML) on (b) Ag(111), (c) Cu(111), and (d) Au(111) at room temperature. (e) The barcode at the bottom are the calculated molecular orbital eigenvalues and the bottom thin line are the model calculations of the single molecule density of states. The LUMO splitting from Au to Ag and Cu as well as the HOMO are indicated by vertical lines between spectra.
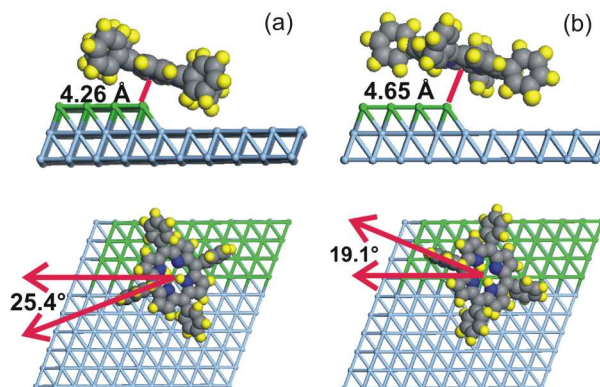
Figure 4.14: GGA-DFT calculated adsorption geometry of 2H-TPP at a step-edge initially oriented with ligand directions at (a) 45° and (b) parallel to the direction of the step-edge.

distortion of the overall shape, with the porphyrin molecules centered above a Ag(111) lattice site. The dihedral angle of the phenyl arms of 2H-TPP on a Ag(111) terrace was found to be 70.5°, which is reasonably close to previously reported 60° for an isolated 2H-TPP molecule [125, 126, 120]. On the step edge, the phenyl arms are rotated between 69° and 74° depending on adsorption geometry. Considering the very slight energy change (0.03 eV) with the dihedral rotation from 60° to 90° [193], the small dihedral angle change of 2H-TPP reflects the interaction between Ag surface and the 2H-TPP molecule.

The molecule-molecule total binding energy for a free porphyrin dimer was found to be 0.15 eV, due to a combination of van der Waals, electrostatic, CH-π, and π-π interactions. In contrast, the resulting binding energy of a 2H-TPP monomer to the Ag(111) terrace was found to be 0.44 eV. The diffusion barrier for a single molecule on the Ag(111) surface was found to be 0.032 eV, on the same order as that seen for other organic adsorbates on Ag(111) surfaces [194]. For comparison, the kinetic energy at 300 and 77 K would be 0.026 and 0.007 eV respectively. Such a small surface diffusion barrier would allow for the molecules to move along the surface, making single lattice jumps before interacting with another at room temperature, as well as at liquid nitrogen temperatures at a reduced rate. The resulting distance of a CH-π interaction in 2H-TPP dimers on a Ag(111) terrace was found to be 3.03 Å, which is only slightly shorter than what was observed with the STM.

Further DFT calculations show the binding between 2H-TPP and the Ag(111) terrace comes from modest electron transfer between the Ag surface and the adsorbed 2H-TPP molecule, where the molecule takes up 0.191 e according to a Hirshfeld analysis. Meanwhile, the electrostatic potential surface (ESP) indicates that the negative electrostatic potential of the inner porphyrin ring of 2H-TPP has an interaction with the positive electrostatic potential of the Ag(111) surface, which could explain the nature of the 2H-TPP adsorption on Ag(111) surface.

Calculations were undertaken for individual molecules bridging the step-edge in multiple orientations. First, a single 2H-TPP molecule was tested with the molecule initially bridging a Ag(111)

step-edge with all phenyl ligands 45° to the boundary of the step-edge. It was found by structural optimization that in this orientation the molecule bound to the substrate at an angle of 28° between the molecule plane and the substrate surface, and at a distance of 4.26 Å(Figure 4.14). The phenyl arms and the step edge enclose an in-plane angle of 25.4°, and the net binding energy was calculated as 0.39 eV. When calculations were run with the molecule initially oriented with two phenyl arms parallel to the boundary of the step-edge and two normal, this molecule rotated upon optimization to an orientation similar to that observed by the STM (exp: in-plane angle of 21°, calculated: in-plane angle of 19°; Figure 4.10 (a) and Figure 4.14 (b), respectively). The resulting molecule-substrate distance was found to be 4.65 Å and the binding energy was found to be 0.55 eV and the Hirshfeld analysis found the Ag gives 0.193 e to 2H-TPP molecules. In both examples, the binding energy for the molecules at the step edge is larger than on flat terraces, explaining the found preferential step decoration.

Computation of the interactions of the 2H-TPP molecule or dimer on the Cu(111) substrate were infeasible for us. However, given the highly preferential binding of the 2H-TPP molecules over step edges on Ag(111), the limiting interaction of the 2H-TPP/Cu(111) system were thought to be due to the nitrogens of the porphyrin macrocycle interacting strongly with the underlying Cu(111) atoms as per similar interactions claimed for 2H-TPyP/Cu(111) [134]. In making a computational comparison between the Ag(111) and Cu(111) systems, calculations were thus performed for lone pyrroline molecules as representing components of the porphyrin macrocycle which have the strongest potential interaction with the substrate. Two types of calculations were performed, one with the pyrroline initially parallel to the substrate, representing 2H-TPP in the terrace phase (Figure 4.15 (a)) and one with the pyrroline initially normal to the substrate, representing 2H-TPP in the step-edge phase (Figure 4.15 (d)).

It was found that for those pyrroline molecules which began initially parallel to the underlying substrates, the simulations of the pyrroline on Ag(111) did not converge (Figure 4.15 (b)), despite being attempted in several different initial orientations. For the pyrroline/Cu(111) sys-
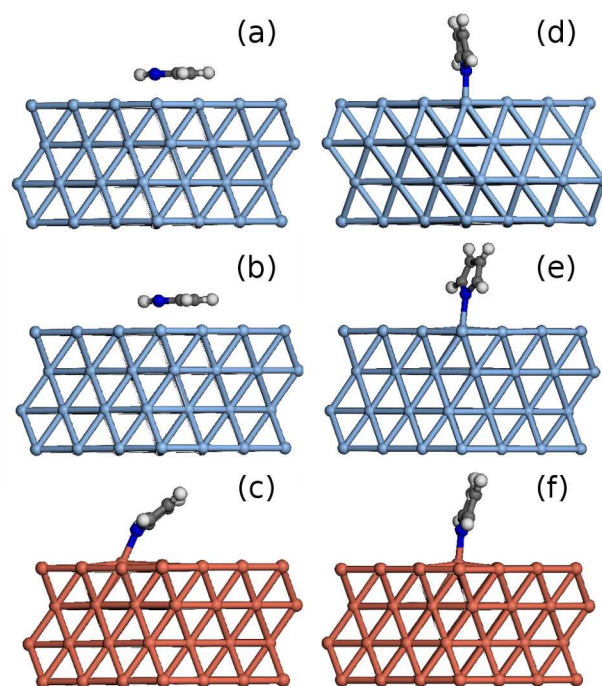
Figure 4.15: Calculated adsorption geometry of pyrroline molecules at Cu(111) and Ag(111) surfaces. The orientations of the molecules (a) initially parallel to the substrate and after convergence for (b) pyrroline parallel to Ag(111) (c) pyrroline parallel to Cu(111). The orientations of the molecules (d) initially normal to the substrate and after convergence for (e) pyrroline normal to Ag(111) (f) pyrroline normal to Cu(111).

tem the molecule bound to the underlying substrate with an energy of 1.49 eV (Figure 4.15 (c)). For those pyrroline molecules initially normal, both the pyrroline/Ag(111) (Figure 4.15 (e)) and the pyrroline/Cu(111) (Figure 4.15 (f)) converged to a strong chemical bond with the substrate. However, the energy of the pyrroline/Cu(111) bond (1.50 eV) was more than twice that of the pyrroline/Ag(111) bond (0.73 eV). In both cases for the Cu(111) substrate, the molecule-substrate system converged to a strong bond due to overlap of the π-orbitals of the pyrroline with the d orbitals of the underlying Cu as per the LDOS.

Taken from these results it is concluded that for the 2H-TPP/Cu(111) system, there was no energetic preference for the molecules binding to the step edge over binding to the underlying terrace. The overlap in the orbitals calculated would be strong enough to create a significant bond

of the porphyrin macrocycle with the underlying substrate regardless of initial orientation. In contrast, a clear preference for step decoration was seen both experimentally and from the 2H-TPP/Ag(111) and pyrroline/Ag(111) calculations.

4.3.6   Discussion

Our observations can be summarized as follows: (i) 2H-TPP are highly mobile on Ag(111) and prefer to occupy substrate step edges in a bridging position, with an angle between phenyl arms and the step edge of approximately $20°$. Upon achieving 100% step-edge occupancy, extended 2D networks are formed on the terraces. (ii) 2H-TPP on Cu(111) does not show any tendency of surface diffusion or self-assembly. The mobility was increased at elevated temperatures, but still no network formation or step edge bridging was observed. The formation of a surface dipole at the molecule sites is observed with STM. (iii) Photoelectron spectroscopy of the occupied and unoccupied states show distinct and easily discernible peaks generally matching published UPS data and theoretical expectations [124, 195, 80, 49]. For low and moderate 2H-TPP coverages on Ag, distinctive molecular orbital features of the occupied states are absent and peak splitting of the LUMO is observed for 2H-TPP/Au(111) by inverse photoemission. (iv) DFT calculations show that the binding energy for 2H-TPP on Ag in various positions and geometries is largest for a bridging position at step edges, with rotated "X" geometry, whereas the binding energy is by over a factor of 2 larger on Cu(111) and independent on the adsorption site.

The observed ordering of the molecules on the terraces of Ag(111) has also been reported for the same moleculs on Ag(111) [117, 119] and for metalated TPP molecules on Cu(111) [178] and is consistent with what has previously been reported for similar systems of porphyrin molecules on noble metal substrates [172, 126, 92, 196, 132, 133, 197]. However, the very strong preferential and ordered bonding the molecules show toward the surface step-edge has not been reported thus far. Also, the observed absence of self-assembly for 2H-TPP on Cu(111) is in striking difference

to the networks reported for Co-TPP or Cu-TPP on Cu(111) [178].

To explain the preferred step edge adsorption, we have presented energy calculations by DFT-GGA for various absorption geometries on step-edges, by varying the angle between the phenyl arms and the step edge as well as the inclination of the molecule against the step-edge. As a result, the experimentally observed orientation of the 2H-TPP was found to have the highest binding energy, about 125% higher than what was calculated for the molecules occupying terrace sites. The preferential step edge decoration is not related to the 2H-TPP macrocycle metalation, as comparative measurements with Ag-TPP on the same Ag(111) substrate showed, which is also inagreement with arguments made in ref [178]. We thus suggest that the observed geometry is largely due to a simple energetic favorability of geometric orientations. The achieved geometrical closeness of the nitrogen atoms in the porphyrin macrocycle to the Ag atoms of the step-edge cannot be achieved on terraces where the rotated phenyl arms determine the macrocyclesubstrate distance, explaining the higher binding energy at the step edges.

Our calculation showed further that the energy of the T-type interaction between neighboring phenyl ligands is 1 order of magnitude smaller than the total binding energy of a 2H-TPP dimer. It is thus concluded that the self-assembly of 2H-TPP into the 2D networks observed on Ag(111) is the result of the interplay between several factors. It is driven by the attractive interaction between the molecules, but only possible if the 2HTPP interacts weakly with the substrate underneath so that diffusion barriers are sufficiently low. The attractive CH-π bonds, regarded as the driving force for network formation in ref [178], are alone insufficient to overcome the diffusion barriers on Ag(111), but do determine the alignment of neighboring molecules with respect to each other, or in other words, the network's geometry.

In contrast to what has been found for 2H-TPP on Ag(111) and for metalated TPP on Cu(111) [178], no self-assembly of 2H-TPP is observed on Cu(111). Networks are also not formed at increased temperatures, when the molecule's diffusion rates are already substantial. It is thus concluded that on Cu(111) the interaction between 2H-TPP is repulsive, which can only be the result

of the interaction with the Cu substrate. The pickup of charges by the molecules from the substrate can result in the formation of a electric dipole and hence electrostatic repulsion between molecules, thereby inhibiting network formation. Such a charge pickup by the 2H-TPP is observed with STM on Cu(111), where the modification of the substrate around isolated 2H-TPP molecules is clearly visible as a ring, which is in analogy to the observed sombrero-like shape of charged metal atoms on insulating films [198] or TCNE molecules on Ag(100) [199] This modified electronic structure surrounding the molecule corresponds well with those predicted and observed for simple two body molecules on Cu(001) [200]. This electron exchange then leads to long-range, electrostatic repulsive molecule-molecule interactions as seen also for other species [201, 199].

A comparison of our findings on 2H-TPP on Cu(111) with published STM data on metalated TPP or TPyP on the same substrate [188, 178, 140] seems further to suggest that not the ligands but rather the macrocycle metalation is controlling the self-assembly: nonmetalated molecules with different ligands (2H-TPP, TPyP) remain isolated on the Cu(111), while only metallated TPP are observed to form networks. This conclusion is backed by related studies of molecule-substrate interactions that conclude that the metal ion in the porphyrin macrocycle plays the central role in the electronic interaction between the complexes and the metal surface, which was even found to result in additional electronic states [124].

Qualitatively, the Cu system possesses a d_{z^2} orbital extending into the vacuum while the outermost orbitals for the Ag and the Au system are more dominated by the frontier s orbitals. The calculated molecular orbitals from our semiempirical calculations of the free molecule, and matching those found with GGA-DFT calculations, are shown in Figure 4.16. It is apparent that the HOMO orbital possesses a_{1_u} symmetry and the LUMO and LUMO+1 orbitals posses b_{1_g} symmetry. Given this, the former will be dominated by d_{z^2} levels while the later will be dominated by p_x and p_y levels. This results in a greater cross-sectional overlap of the 2H-TPP HOMO levels with both the d_{z^2} and 4s frontier orbitals of the Cu(111) system versus only the 5s and 6s orbitals of the Au(111) and Ag(111) systems. Given that the former will have a much larger cross-sectional
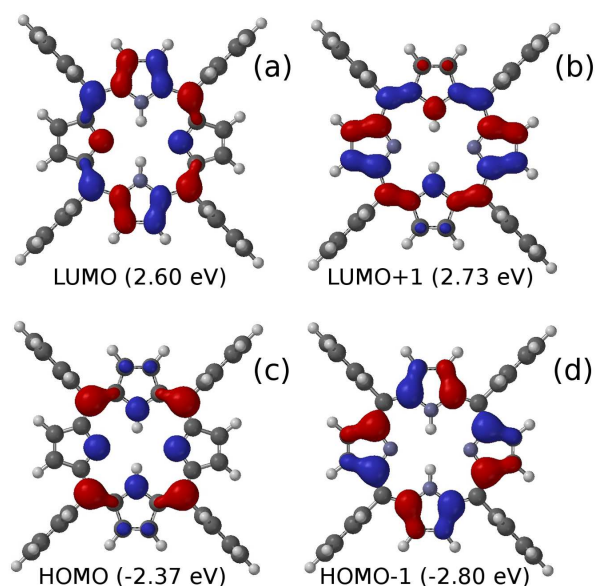
Figure 4.16: Orbitals corresponding to semiempirical NDO-PM3 model calculations. (a) LUMO (b) LUMO+1 (c) HOMO and (d) HOMO-1

overlap with the orbitals of the adsorbed porphyrin than will the later, enhanced electron transfer and therefore, tunnelling, directly from the tip to the metal substrate via the adsorbed molecules is achieved. This interaction can create enough charge in the molecule-substrate system to hinder 2D network growth through Coulomb repulsion. This is similar in concept to Co-TPP [178, 202] and Fe-TPyP [126, 135] deposited on metal substrates, as the d_{z^2} orbital of the metal in the molecule provides the same general overlap with the underlying metal that the Cu has with the adsorbed molecules here.

Given that the substrates are, by themselves, similarly electronegative, it is this greater frontier orbital overlap which transfers a greater amount of charge between the substrate and the adsorbate. The charge transfer is then responsible for the significant electronegativity seen in the HOMO state of the surface 2H-TPP on Cu(111) of Figure 4.11 (b) as well as the apparent modified electronic structure surrounding the molecule.

From the location of the LUMO of the 2H-TPP on the macrocycle, as seen in Figure 4.16, a
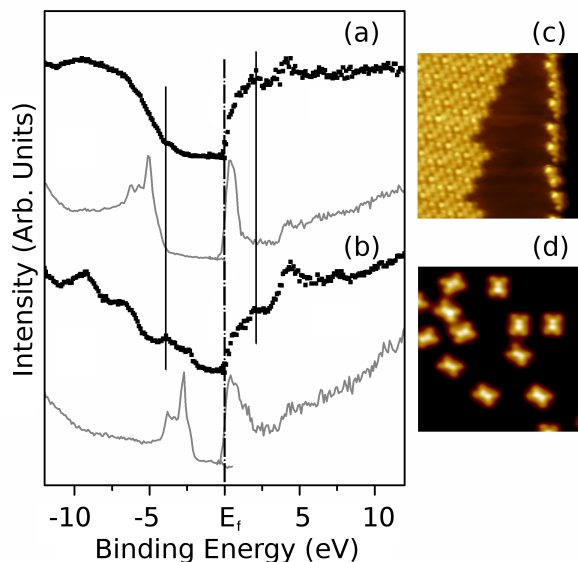
Figure 4.17: Comparison of photoemission and inverse photoemission spectra of thin film 2H-TPP (0.5 ML) on (a) Ag(111) and (b) Cu(111), along with the spectra of the corresponding clean substrate at room temperature. STM images of 1/3 ML thick 2H-TPP on (c) Ag(111) and (d) Cu(111) are shown on the right side of the Figure (10×10 nm). V = -0.8 V.

perturbation of the LUMO by the formation of week CH-π bonds with the phenyl arms of neighboring molecules can be expected. This perturbation may lead to the splitting of the LUMO states by 1.1 eV observed in the inverse photoemission data, see Figure 4.13 (d). This level splitting is observed on Au(111) and, to lesser extend on Ag(111) where the 2H-TPP molecules are observed to form a network structure [178, 203, 204]. This splitting is not observable on Cu(111), where the molecules remain isolated.

In Figure 4.17 we compare UPS/IPES spectra for sub-monolayer coverages of 2H-TPP on Ag and Cu with STM images taken at such coverages. Striking here is the absence of discernible peaks in the UPS spectra of 2H-TPP/Ag(111). We suggest that the coexistence of different structural phases with fundamentally different orientation relative to the substrate in multiple energetic orientations smear out peaks in the UPS spectra as seen for other adsorbate-surface systems [205]. DFT calculations support this observation by showing that step-edge sites held significantly higher

binding energies than terrace sites for the 2H-TPP/Ag(111) system. Electronic features similar to those of free 2H-TPP molecules appear only at coverages above 3 ML where the layer stacking is the dominating structural arrangement.

4.3.7 Conclusion

It has been demonstrated that the tendency of porphyrins to self-organize is limited by interactions with the substrate. While a rather significant molecule-substrate bond exists for 2H-TPP on all substrates studied, the limiting factor in formation of self-organized islands is apparently the nature of the frontier orbital overlap and resulting electron transfer, which is mainly involving the macrocycles of the molecules.

The self-assembly of near charge neutral 2H-TPP molecules into extended 2D networks on Ag(111) is due to a combination of van der Waals, electrostatic and CH-π interactions between the molecules. The relative orientation of neighboring molecules is mainly given by the CH-π interactions, due to which there is a perturbation of the electronic states of the adsorbed molecules. Charge pickup and dipole formation of 2H-TPP on Cu(111) results in repulsive Coulomb interactions which seem to dominate over attractive intermolecular interactions, thus preventing network formation. A zone of modified electronic structure is observed around the molecules on Cu(111), which is indicative of such strong molecule-substrate interactions and charge uptake by the molecules. This mechanism seems to be absent for 2H-TPP/Ag(111) and 2H-TPP/Au(111), where the orbital overlap differs significantly from that of the 2H-TPP/Cu(111) system. The comparison of our results with published work on Co-TPP, Cu-TPP, and TPyP suggests that the molecule-substrate interaction strength is governed by the molecule's metalation, and not so much by the ligands.

The morphology of the substrate surface is also important as the molecules are observed to preferentially bridge the substrate step-edges before island nucleation starts on the terraces. The discussed examples showed that the properties of 2D layers of organic materials can be controlled

by interactions with the supporting substrate. Specifically, it was shown that the structural arrangement, HOMO-LUMO gap, and details of the electronic structure are determined by the substrate, therebu improving our understanding of planar organic molecular adsorption and self-assembly on surfaces.

Acknowledgements

4.4   Surface state engineering of molecule-molecule interactions[‡]

Geoffrey Rojas[†], Xumin Chen[†], Donna A. Kunkel[†], Justin Nitz[†], Xie Jiao[†], Peter A. Dowben[†], Scott Simpson[‡], Eva Zurek[‡], Axel Enders[†,§]

Department of Physics, University of Nebraska-Lincoln, Lincoln, NE 68588 USA

Department of Chemistry, State University of New York at Buffalo, Buffalo, NY 14260 USA

Abstract

Engineering the electronic structure of organics through interface manipulation, particularly the interface dipole and the barriers to charge carrier injection, is of essential importance to improved organic devices. This requires the meticulous fabrication of desired organic structures by precisely controlling the interactions between molecules. The well-known principles of organic coordination chemistry cannot be applied without proper consideration of extra molecular hybridization, charge transfer and dipole formation at the interfaces. Here we identify the interplay between energy level alignment, charge transfer, surface dipole and charge pillow effect and show how these effects collectively determine the net force between adsorbed porphyrin 2H-TPP on Cu(111). We show that the forces between supported porphyrins can be altered by controlling the amount of charge transferred across the interface accurately through the relative alignment of molecular electronic levels with respect to the Shockley surface state of the metal substrate, and hence govern the self-assembly of the molecules.

4.4.1 Introduction

The electronic properties of organics in contact with metal substrates depend on the alignment of the electronic levels and bands at the metal-organic interface and the resulting hybridization of states, as well as charge transfer to or from the adsorbate, the molecular band offsets [14, 206, 67], the emergence of interaction-induced states [207, 124], the distortion of the molecules [208] as well as changes that may occur at the substrate surface [209]. Also key to the interface electronic structure is the presence of substrate surface states [210]. Generally, the properties of metal-organic interfaces are determined by a delicate balance of competing factors and experiments usually assess only the cumulative effect of many different contributions to the interface electronic structure [208, 209]. The net charge transferred across the interface, the formation of charge dipoles, and the work function are intrinsically related effects. Often what is highlighted is the interface dipole or the work function, but the substrate surface states, a fundamental ingredient to the interface electronic structure is often poorly described. Here we demonstrate the importance of the Shockley surface states [210] in establishing the interface electronic structure using the example of tetraphenyl porphyrins (2H-TPP) chemisorbed on Cu(111). The surface state interactions with the adsorbed molecular layers are important for the charge transfer between the substrate and the molecule and the resulting surface dipoles that ultimately strongly influence the intermolecular lateral interactions. The surface state can be shifted in energy by using Ag buffer layers of varied thickness on Cu(111), thereby determining the overlap of molecular levels with substrate surface metal bands [206], the amount of charge transferred, and consequently the intermolecular forces. We can relate our findings to the observed strong repulsive intermolecular Coulomb forces and the repression of molecular self-assembly. We show that the molecule-molecule interactions can be changed from repulsive to attractive by controlling the amount of charge transferred across the interface through surface state engineering using Ag buffer layers on the Cu(111).

4.4.2 Results and Discussion

The 2D character of an adsorbed monolayer of 2H-TPP has been exploited for a comparative study of the occupied and unoccupied band structure of large ensembles with direct and inverse photoelectron spectroscopy (UPS and IPES), as well as of selected individuals with the tip of a scanning tunneling microscope (STM) in the local spectroscopy mode (STS). By this combination of local and area-integrating complementary methods the atomistic basis of observed features in the electronic structure became evident. STM images, taken at sub-monolayer to monolayer coverage of 2H-TPP on Cu(111), are shown in Figure 4.18. A coverage of $\Theta = 1$ ML is defined here as the maximum observed packing density within the first layer of 0.42 molecules·nm^{-2}. This packing is 20% smaller, expressed in terms of areal density, than that observed on Ag(111), see Figure 4.18 (e) [116, 178]. The mobility of the molecules is sufficiently high for surface diffusion, as concluded from visible substrate step edge decoration (not shown), however, no nucleation is observed. The molecules remain isolated and roughly equally spaced on the terraces of the Cu(111) (Figure 4.18 (b - c)). They appear to be aligned along the three $\langle 111 \rangle$ crystallographic directions of the surface, concluded from the observed angles of multiples of $120°$ between the major axes of any two molecules. It can be seen by comparing Figure 4.18 (b) and (c) that molecules are added to the first monolayer even if the gaps between the molecules are significantly smaller than the size of the molecules itself. This requires rearrangement of all molecules in the layer during deposition. Self-organization of the 2H-TPPs into networks, as found for the same molecules on Ag(111) in Figure 4.18 (a) and Au(111) [116, 178, 119], was not observed on Cu(111) at any coverage and sample temperature in the rage between 77 K and 500 K. We do observe, however, by inspection of Figure 4.18 (c, d) that an alignment of the molecules with respect to each other sets in as the areal density of the molecules increases. Upon reaching saturation coverage within the first layer, molecules nucleate into islands on top of the first layer. The architecture of this arrangement is a porous 2D network apparently dominated by $\pi - \pi$ bonds, and is a different architecture than the

densely packed arrangement observed for the same molecules on Ag(111) in Figure 4.18 (a). We conclude from these observations that the net force between the molecules within the first layer is repulsive, while it is attractive for the molecules within the second layer.
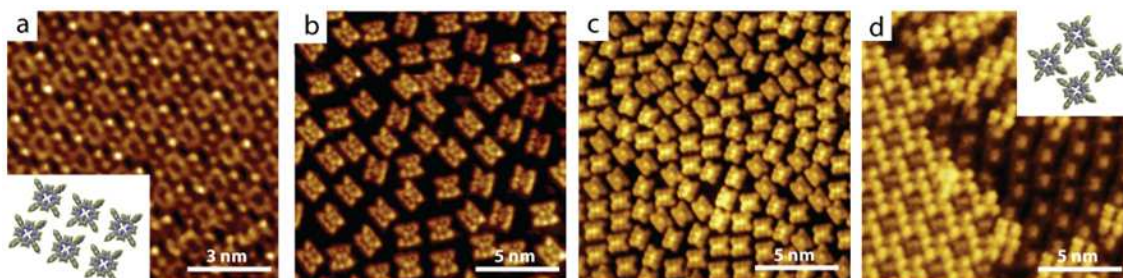

Figure 4.18: STM images of 2H-TPP on Ag(111) (a) and Cu(111) (b-d). The molecule coverage is 0.6 ML (b), 0.7 ML (c) and 1.2 ML (d). $I_t = 0.4$ nA, $U_b = +0.8$ V.

The occupied and unoccupied electronic structure of the adsorbate-substrate system has been studied in detail with tunneling spectroscopy and combined photoemission and inverse photoemission spectroscopies, as seen in Figure 4.19. The combined photoemission spectra of the 2H-TPP covered Cu(111) shows characteristic peaks that are not observable in the spectra of the pristine Cu(111). One feature, at +2 eV, is in reasonable agreement with the lowest unoccupied molecular orbital (LUMO) of calculated and measured spectra for similar TPP systems [211]. Also the spectra of the occupied states resemble those reported for 2H-TPP adsorbed on other noble-metal systems [212], with the highest occupied molecular orbital (HOMO) at approximately -2 eV. Within this HOMO-LUMO gap we observe an additional characteristic peak at +0.65 eV at sub-monolayer coverage, which is observed to decay rapidly in intensity with increasing coverage and is not apparent in the spectra at 3 ML coverage or more.

Complementary to the combined photoemission and inverse photoemission spectroscopy measurements, point spectroscopy measurements have been taken locally with STS over a similar energy range, see bottom panel in Figure 4.19. Single point dI/dV spectra were taken over the molecules themselves, as well as the surrounding Cu surface at successively increasing distance from the molecule center. The observed HOMO and LUMO of the molecules are aligned well
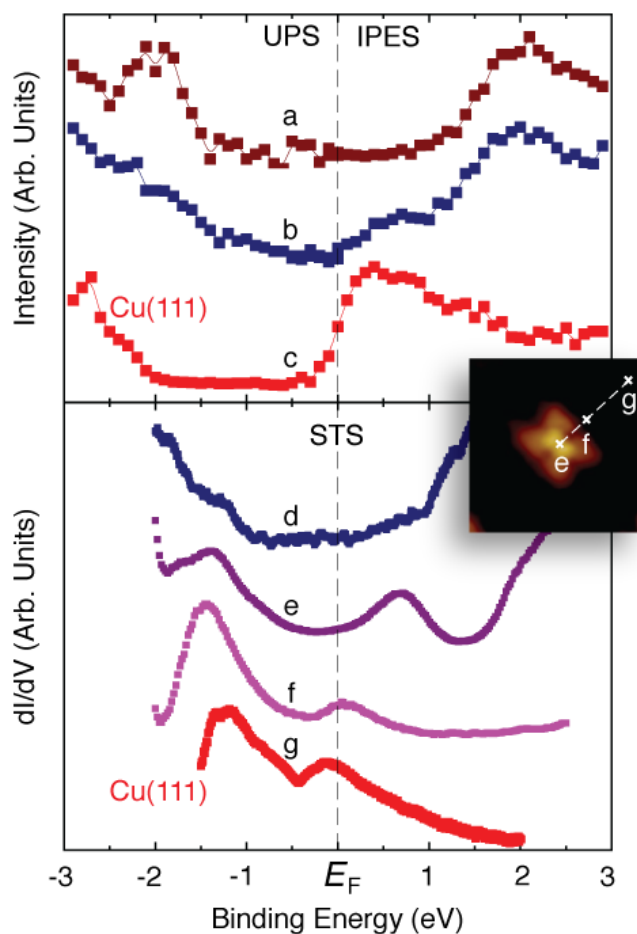
Figure 4.19: Upper panel: Photoemission (UPS) and inverse photoemission (IPES) spectra of 2H-TPP on Cu(111). (a) 3 ML 2H-TPP; (b) 1 ML 2H-TPP; (c) bare Cu(111). Lower panel: STS point spectra taken on or near lone TPP molecules. (d) on top of a molecule in the second layer; (e) on top of a molecule in the first layer; (f) on Cu, at a distance of 1 Angstrom from the molecule edge; (g) on Cu, several Angstroms away from a molecule. Inset: STM image showing the positions where spectra (e-g) were taken. Binding energies are denoted as $E - E_F$, making occupied state energies negative and unoccupied states positive.

with those observed using photoelectron spectroscopy; the LUMO is seen at approx. 1.5 eV above the Fermi level, contained with the LUMO + 1 peak. The spectra taken on the bare Cu show the well-known Shockley surface state at -0.4 eV [213, 214], which is not resolved in the photoelectron spectra. This surface state is suppressed on the Cu surface covered with $\Theta > 0.7$ ML 2H-TPP. At lower coverage, this surface state is shifted towards the Fermi level in the direct vicinity of the

molecule. The spectra shown in Figure 4.19 (f) was taken at a distance of 6 Åfrom the molecule center and shows this surface state shifted upward in energy by $\Delta E = 0.2$ eV. Also within the HOMO-LUMO gap at +0.7 eV an electronic state, already known from the IPES measurements, is observed at the molecules. This peak is only observed for spectra taken of molecules in the first monolayer. Spectra taken on molecules in the second layer do not show this substrate surface state feature, and yet the characteristic LUMO and HOMO remain undisturbed.

The molecules of the second layer appear in the STM images under the same tunneling conditions with dark center and bright phenyl arms, while in the first layer the opposite is observed, the centers are bright and the phenyl arms are dark. This change in contrast is due to an electronic level rearrangement at the interface [124]. We again exploit the local nature of tunnel spectroscopy to identify local differences in the DOS. In STS point spectra taken at the center of a molecule in the second layer the new peak at +0.65 eV, observed over the molecules in the first layer, does not appear. This allows us to attribute the physical origin of this state to the 2H-TPP/Cu interface. The electronic states in this energy range have been observed previously for other porphyrin-based surface systems on Ag(111) as well as Cu(111) with photoelectron spectroscopy [124, 215, 128], and have been heretofore ascribed to the shifted LUMO of the porphyrin macrocycle. However, the absence of the energy state at +0.65 eV in the second monolayer provides now evidence that this state is an interface state.

Measurements of the local work function, Φ, have also been made using the STM. We have characterized and measured the local work function to evaluate the local surface dipoles, following a procedure similar to that published in reference [15] and described in the supplementary material. The so measured work function of the Cu(111) is $\Delta\Phi = (4.9 \pm 0.2)$ eV. With 2H-TPP deposited, we find a decrease of the work function by $\Delta\Phi \sim (-2.0 \pm 0.5)$ eV over the center of TPP molecules, and an increase of $\Delta\Phi \sim (+1.0 \pm 0.4)$ eV at the boundary of the molecules macrocycle. While these data are in quantitative agreement with the net work function shift of 0.84 eV found for 1 ML 2H-TPP on Ag(111) [124], the particular advantage of these local measurements is that they

reveal a significant amount of spatial variance. For clarification of the spatial variance, a map of the work function has been measured in a square area across the molecule and its surrounding from 100×100 separately performed point spectra. This Φ-map is shown together with an STM image of a lone 2H-TPP on Cu(111) in Figure 4.20. By comparing both results in this manner the spatial dependence of the work function can be associated with local chemical components of the adsorbed molecule, and with the locally measured density of states. The Φ drops significantly over the location of the central pyrolines while increasing relative to the bare Cu(111) over the surrounding hydrogen edges and phenyl ligands. Surrounding the molecule in a narrow band there is a slight drop in the Cu(111) work function. This band corresponds to the area where the upward shift in the surface state was observed, too.
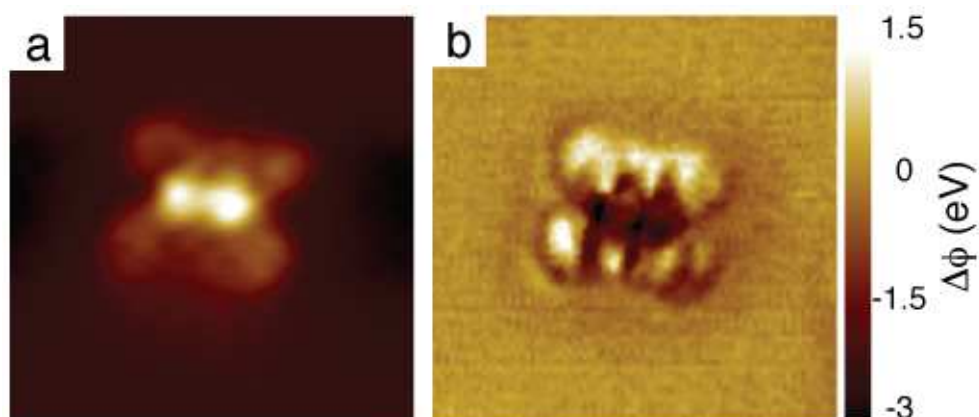

Figure 4.20: (a) STM image of a lone 2H-TPP molecule on Cu(111). $I_t = 0.4$ nA, $U_b = +0.8$ V; image size 4 nm $\times$ 4 nm. (b) Work function map of the same molecule, showing lowered work function at the center of the molecule and increased work function at the boundary of the molecule, relative to the substrate.

The electronic interactions at the 2H-TPP/Cu(111) and the 2H-TPP/Ag(111) interfaces can be understood using the results of density functional theory calculations, undertaken as described in the supplementary material. The computational results, summarized in Table 4.2, show that the binding energy of the molecules to the substrate is significantly larger on Cu(111) (3.96 eV) than on Ag(111) (0.42 eV), resulting in a much shorter distance between the molecule and the substrate

and significant distortion of the molecule on Cu(111) (Figure 4.21). In particular, the dihedral angle of the phenyl ligands changes and the ligands become nearly planar to the surface. For comparison, we calculate the free 2H-TPP molecule as having a dihedral angle of 62.7 degrees, in agreement with refs [125, 126, 120, 116]. This distortion is also visible in the STM images in Figure 4.18 (b). As a result of the rotation of the phenyl arms, the pyrrole rings containing the N-H motifs distort downwards and those containing the lone nitrogen atoms distort upwards. The composition of the molecular orbitals of the metal-adsorbate system was decomposed into contributions from occupied and unoccupied orbitals of the finite copper cluster and of the 2H-TPP. The resulting interaction diagram revealed a state at about 1.1 eV below the Fermi level, which contains character from the 2H-TPP HOMO (57%) and various copper slab MOs (43%) (see supplement), indicating a strong overlap and interaction (hybridization) between these two states. A similar calculation for Ag(111)-TPP showed a much weaker interaction between silver slab MOs (10%) and the 2H-TPP HOMO (90%). The distance between the silver slab and the 2H-TPP is large, so the resulting overlap between these two orbitals is small, and the bond is weak. Our findings are in agreement with the increase in nobleness of a metal descending down Group 11 from Cu to Ag to Au. [206] The interaction of the 2H-TPP HOMO with the Cu states results in a deep-lying filled bonding state, with almost equal contribution from the Cu and the molecule and a concomitant transfer of charge to the copper surface. The build of charge surrounding the copper-molecule interface (the red isovalue in Figure 4.21 (c), along with the charge on the molecules themselves, both which are much larger for the 2H-TPP Cu system than for 2H-TPP - Ag, prevents the adsorbate molecules from interacting with one another due to electrostatic repulsion, thereby impeding self-assembly on the Cu(111) surface.

The charge density difference plots in Figure 4.21 reflect strong variations in the charge density at the interface upon adsorption: there is charge depletion directly under the center of the molecules and an increase in the charge density along the edges of the molecule and under the phenyl ligands. The underlying mechanism here is Pauli repulsion, which follows from the quantum mechanical

Table 4.2: The binding energy (Eb), charge and structure of 2H-TPP on top of Cu(111) and Ag(111). The surface distances, d_{Cu} and d_{Ag}, are the average calculated distances of the central nitrogen atoms of the 2H-TPP to the metal. The dihedral angle is defined in the supplemental material.

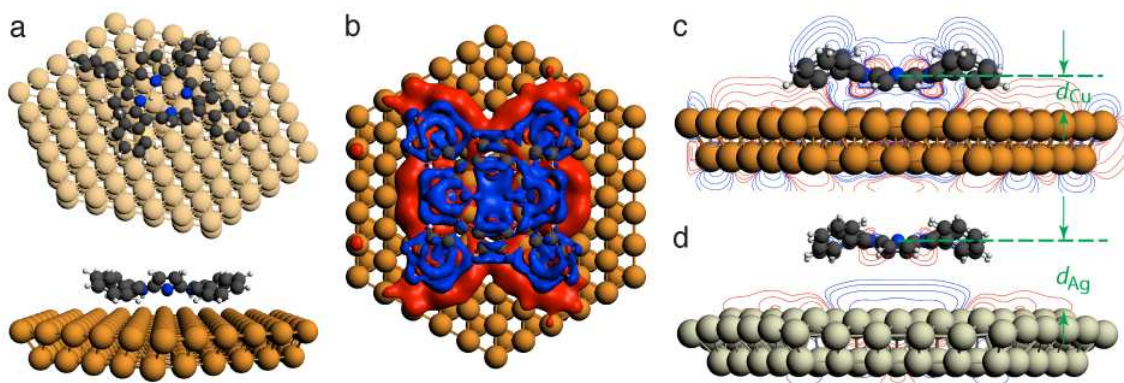| System	E_b (eV)	Surface charge	Adsorbate charge	Dihedral angle (deg)	Surface distance d (Å)
Cu(111)	3.96	-1.69	1.69	40.4	3.04
Ag(111)	0.42	0.02	-0.02	49.2	7.02

Figure 4.21: (a) Top and side view of the optimized geometry of 2H-TPP on top of a Cu(111) slab. (b, d) The calculated differences between the charge density of the metal-organic systems and that of the isolated, distorted fragments illustrates how the charge density changes upon adsorption of the molecule to the metal surface, with blue being a decrease and red an increase. (b) 2H-TPP on Cu(111) with an isovalue of $\pm$ 0.0003 au. (c, d) Contour diagrams for 2H-TPP on top of Cu(111) (c) and Ag(111) (d). The same settings were employed to obtain the contours. The values dCu, dAg, are listed in Table 4.2

requirement that overlapping electronic states must be orthogonal to each other. This drives up the energy and as a result pushes charge away at the surface of the Cu in an area directly under the center of the molecule. This effect has been described as the "pillow effect" [65, 206, 83, 66], The redistribution and exchange of charge also changes drastically the surface dipole of the Cu and is at the origin of the observed spatial variation of the work function. By comparison, the negligible charge transfer from Ag to the adsorbate is in line with a weaker binding energy, a longer metal-adsorbate distance and a negligible pillow effect occurring on the metal's surface.

Besides the electrostatic repulsion between the molecules there are also attractive interactions,

mainly van-der-Waals and dispersive interactions. Additional bonding contributions come from CH-π and $\pi - \pi$ interactions between the phenyl ligands. For a freestanding 2H-TPP dimer, the total binding energy was estimated to be 0.3 eV. The net effect is thus dependent on the competition between Coulomb repulsion and the mainly van der Waals attraction. The net force is attractive for 2H-TPP on Ag(111) and Au(111) [128, 116, 216] and repulsive on Cu(111), owing to the discussed differences in charge transferred and Coulomb repulsion. A similar dominance of the electrostatic repulsion has been reported earlier for other organic-metallic interface systems [199, 201, 116, 10, 70]. In addition here, the distorted phenyl arms of the molecules impede the formation of $\pi - \pi$ bonds, thereby further decreasing the propensity of binding between two 2H-TPP molecules.

The observed differences in the interactions of 2H-TPP on Ag and Cu surfaces were exploited to actually control the inter-molecular forces, between the repulsive and attractive limits by engineering the metal-organic interface. The trick is to deposit the molecules on the Cu(111), which was pre-covered by an Ag buffer layer of variable thickness. The STM images of 2H-TPP adsorbed on 1 to 3 monolayers of Ag on Cu(111) are shown in Figure 4.22. Clearly, the molecules remain, more or less, statistically distributed on 1 ML Ag/Cu, while islands of extended networks, identical in architecture to that found on Ag(111) in Figure 4.18 (a), are observed for the 2H-TPP adsorbed on 3 ML Ag/Cu. At the intermediate Ag buffer layer thickness of 2 ML, clusters of 2H-TPP adsorbed molecules are commonly observed but with noticeable degree of disorder within such clusters. On Ag layers on Cu, the 2H-TPP molecules appear in 2 distinctively different symmetries: the symmetry labeled (i) which is usually observed on Cu(111), and the symmetry labeled (ii) which is typical for TPP on Ag(111). With increasing Ag layer thickness, the occurrence of 2H-TPP molecules in configurations of type (i) decreases while at the same time the occurrence of the 2H-TPP adsorbed molecules in the arrangement of type (ii) increases. It appears as if clusters of molecules, ordered or disordered, are mostly formed by 2H-TPP adsorbed molecules of type (ii).

Tunneling spectroscopy was again employed to elucidate the local electronic structure of the
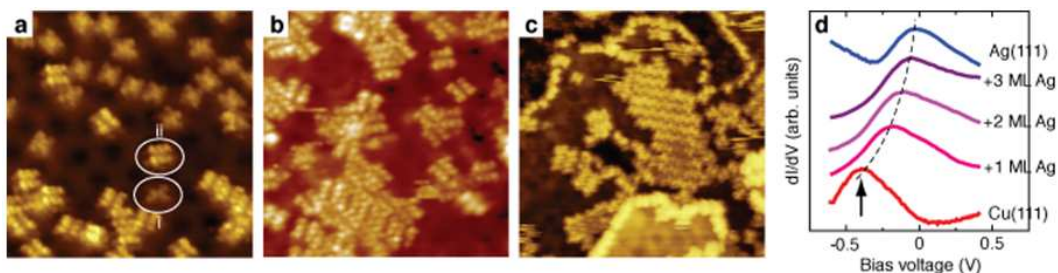
Figure 4.22: STM images of 2H-TPP on Ag buffer layers of θ_{Ag} on Cu(111), where $\theta_{Ag} = 1$ ML (a), $\theta_{Ag} = 2$ ML (b), $\theta_{Ag} = 3$ ML (c). Two different shapes of the molecules are observed, labeled (i) and (ii), see text for explanation. Image size 15 nm × 15 nm. (d) STS point spectra on Cu, Ag films on Cu, and Ag substrates showing the Shockley surface state.

interface. While the spectrum of electronic states taken on top of the molecules does not show significant differences for all samples in Figure 4.22, the Shockley surface state of the substrate on the other hand shifts upward in energy with increasing thickness of the Ag buffer layer, from -400 meV for clean Cu(111) to -50 meV for Ag(111) (Figure 4.22 (d)). The energy of this Shockley state is thus a precise indicator for the Ag layer thickness. Key is that the energy of the Shockley state can be adjusted by the Ag buffer layer thickness between the two extremes of pure Ag(111) and Cu(111) surfaces, and that has profound consequences for the molecular self-assembly as just demonstrated.

4.4.3 Conclusions

It is has been already established that the electronic level alignment at the metal-organic interface and frontier orbital symmetry determines the hybridization of levels and the amount of charge transferred across the interfaces [14, 62]. Based on the results shown here, we find it reasonable to assume that the Shockley state plays a crucial role for the interaction strength. Depending on the exact energetic position of this state, more or less overlap with the corresponding molecule levels is possible, thereby facilitating (Cu) or impeding (Ag) charge transfer across the interface. By controlling the exact energetic position of the surface state by the choice of thickness of Ag

buffer layers on Cu(111), the degree of electronic level hybridization can thus be finely tuned, to adjust the amount of charge transferred and the strength of the Coulomb repulsion. Since the van der Waals interaction remains unaffected by this, the net effect can thus be chosen to be repulsive or attractive. The ability to control inter-molecular forces for a particular type of molecule between both extremes in this manner opens new possibilities to steer molecular self-assembly, especially if patterned buffer layers are used. It is thus an important new milestone in establishing rational design principles for organics in contact with surfaces. Specifically, we demonstrated the potential of using substrates to build organic structures and frameworks of potentially greater complexity than currently possible, exhibiting pre-defined and desired functionality.

4.4.4   Experimental

The experiments were carried out using a Omicron low temperature scanning tunneling microscope in a ultrahigh vacuum system with a base pressure of 8×10^{-11} mbar. Single crystalline substrates have been cleaned in UHV by Ar+ ion sputtering and annealing. TPP molecules have been deposited by thermal evaporation from a home-build Knudsen cell, with the substrate held at room temperature. The combined photoemission and inverse photoemission spectroscopy measurements have been performed in a second UHV system[32] but using the same substrates and Knudsen cells.

The DFT-D calculations were carried out using the ADF software package [217, 218]. The revPBE gradient density functional [219] was employed, and Grimmes latest dispersion corrected functional [220] was used to account for the dispersion forces. Tests were performed to determine the effect of the basis set on the binding energy of benzene to an Ag(111) slab. For the results given in the main text, the basis functions on all of the atoms consisted of a valence triple-ξ Slater-type basis set with polarization functions (TZP) from the ADF basis-set library. The core shells up to 1s, 1s, 3p and 4p of carbon, nitrogen, copper and silver, respectively, were kept frozen. In

situations where SCF convergence issues arose, the steepest decent method was employed. A Mulliken charge analysis was used to determine the magnitude of the charge transferred between the adsorbate and the metal surface. More computational details and complementary results are provided in the supplementary material.

Author contributions

All authors contributed extensively to the work.

Acknowledgements

4.4.5 Supporting Information

4.4.5.1 Experimental Details

Ag(111) and Cu(111) single crystals used for sample surfaces were prepared by three repeated cycles of Ar+ ion sputtering and annealing to 650 K in ultrahigh vacuum (10^{-10} Torr) to remove defects. Ag buffer layers were deposited on the Cu(111) surface at 300 K using an e-beam evaporator and 99.999% pure Ag beads at a consistent rate of 0.013 ML·s^{-1} for all samples. Following annealing, the Ag/Cu(111) samples were imaged to ascertain the surface coverage. 5, 10, 15, 20-tetraphenyl-21-H, 23-H-porphine (2H-TPP) molecules of >97% purity purchased from Frontier Scientific were deposited on the Ag/Cu(111) buffer layer system using a homebuilt Knudsen Cell evaporator at a rate of approximately 0.03 ML·s-1. The system was then transferred in situ for measurement. Data were obtained using an Omicron low-temperature scanning tunneling microscope (LT-STM), operated at 80 K using a W tip.

The work function was determined from measurement of the tunnel current, *I*, as a function of tip-sample separation, *z*, following the well-known relationship

$$\Phi = \frac{\hbar^2}{8m_e}\left(\frac{d}{dz}lnI\right)^2 \tag{4.5}$$

where m_e is the electron mass and $\Phi = \frac{1}{2}\left(\Phi_{tip} + \Phi_{sample}\right)$ [15]. The separation was varied from 100 picometers above the apparent surface to 400 picometers with the tip-sample potential held constant at +400 meV, and the resulting tunneling current was measured. Numerous scans were first taken over the bare surface to verify the stability and reliability of the tip-surface interface. Multiple loops were performed over each point to provide an averaged single set of data for final analysis. The derivative of the natural logarithm of the resulting spectra were then analyzed according the prescription given by Yoshitake [46].

Scanning tunneling spectra were obtained by connecting the system to a Princeton Scientific lock-in amplifer and holding the tip at a constant separation distance, z, while modulating the DC voltage around a set voltage bias *V* by an amplitude between 10 to 20 meV and at a frequency of ∼3 kHz. By then measuring the resulting modulation in current, *dI*, the differential in current was obtained as a function of the bias voltage and the local density of states was measured.

4.5   Summary

This thesis has demonstrated that the self-assembly of the organic/metal surface system of 2H-TPP on Ag(111) and Cu(111) is limited by the energetic barriers created by the interaction with the metal surface and that this interaction is controllable. The long-range interactions which limit self-assembly of the 2H-TPP/Cu(111) system are due to a combination of energy level hybridization and surface state restructuring as outlined in Chapter 4.4. The energy level hybridization results in charge exchange between the metal and the adsorbed molecule, predicted to be +1.69 e (Table 4.2). The close surface separation and large d_{z^2} orbitals of the Cu electrons causes an overlap of molecular orbitals and surface DOS, resulting in significant shifts in the surface electrons due to Pauli exclusion. This, combined with the charge exchange, results in a very strong surface dipole that prevents inter-molecular binding despite observed mobility at the temperatures deposited (Chapter 4.3).

The molecules on Ag(111) and Au(111) exhibit a much weaker interaction, and little or no hybridization. This results in a much greater surface separation and no significant charge exchange or perturbation of the underlying surface electrons. This lack of surface dipole presents no observed long-range interaction acting in opposition to the weak inter-molecular bonding of the free molecule, unlike the 2H-TPP/Cu(111) system. The molecules move freely and are able to therefore form self-assembled, close-packed, inter-molecular networks. The lattice arrangement of the networks is unique to the individual molecules because of the unique symmetry of the molecule and anisotropy of the hydrogen bonds.

The growth dynamics of the 2H-TPP/Ag(111) surface system occurs according to the same energetic hierarchy of barriers as that of metal heteroepitaxy. The barriers affecting the geometry of the resulting surface structure are those of the inter-molecular attractive potentials described as due to a combination of van der Waal and CH-π bonds. Using the same energetic hierarchy models as inorganic systems, and approximation for the inter-molecular bond is found to be 130 eV ∼

160 eV. This is consistent with the models of the bond between free 2H-TPP dimers, giving further evidence of the weak binding of the underlying surface.

The energy level of the interacting metal surface state is controlled through the addition of atomically thin Ag buffer layers to the Cu(111) surface. This allows for the tuning of the metal/organic interface states and surface electron suppression, thereby adjusting the Coulomb potential and inter-molecular repulsion to levels lower than the inter-molecular attractive potentials, which remain unaffected as they are inherent to the physical makeup of the molecule. This shows the ability to control the self-ordering of organic adsorbates on metal surfaces using a new dimension to material design: surface engineering. By understanding the physical origin of the surface interaction, the chemistry of the underlying metal may be manipulated to control the self-assembly and growth of the adsorbate, rather than changing the structure of the pre-defined molecule. While done here using the surface dipoles and charge transfer, other mechanisms including surface states, patterned surfaces, and band structure alignment may be further used to control the self-assembly of organic molecules.

Bibliography

[1] J. Hwang, A. Wan, and A. Kahn, Mat. Sci. Eng. R **64**, 1 (2009). 1, 3.1.3, 4.2.1

[2] J. C. Bernéde, J. Chil. Chem. Soc. **53**, 1549 (2008). 1

[3] J. Weickert, R. B. Dunbar, H. C. Hesse, W. Wiedemann, and L. Schmidt-Mende, Adv. Mater. **23**, 1810 (2011). 1

[4] G. Horowitz, Adv. Mater. **10**, 365 (1998). 1

[5] J. S. Miller and A. J. Epstein, Ang. Chem. **33**, 385 (1994). 1

[6] H. Wende, M. Bernien, J. Luo, C. Sorg, N. Ponpandian, J. Kurde, P. M. Miguel, J., X. Xu, P. Eckhold, W. Kuch, et al., Nature Materials **6**, 516 (2007). 1, 4.3.1

[7] X. Lin, J. Jia, P. Hubberstey, M. Schrder, and N. R. Champness, CrystEngComm **9**, 438 (2007). 1

[8] Y. Okamoto and W. Brenner, *Polymers* (1965), chap. Organic Semiconductors, p. 125. 1

[9] C. Deibel and V. Dyakonov, Rep. Prog. Phys. **73**, 906401 (2010). 1

[10] Z. G. Soos and B. J. Topham, Org. Elec. **12**, 39 (2011). 1, 3.1.5, 4.1, 4.1, 4.4.2

[11] E. V. Tsiper, Z. G. Soos, W. Gao, and A. Kahn, Chem. Phys. Lett. **360**, 47 (2002). 1

[12] V. Coropceanu, J. Cornil, D. A. "da Silva Filho", Y. Olivier, R. Silbey, and J.-L. Brédas, Chem. Rev. **107**, 926 (2007). 1

[13] W. Brütting, *Physics of Organic Semiconductors* (Wiley, 2005). 1

[14] H. Ishii, K. Sugiyama, E. Ito, and K. Seki, Advanced Materials **11**, 605 (1999). 1, 3.1, 3.1.4, 4.4.1, 4.4.3

[15] L. Vitali, G. Levita, R. Ohmann, A. Comisso, A. D. Vita, and K. Kern, Nature Mater. **9**, 320 (2010). 1, 2.2.3, 4.4.2, 4.4.5.1

[16] P. Avouris and R. Wolkow, Appl. Phys. Lett. **55**, 1074 (1989). 2.2

[17] R. J. Hamers, R. M. Tromp, and J. E. Demuth, Phys. Rev. Lett. **56**, 1972 (1986). 2.2, 2.2.2

[18] J. A. Stroscio, R. M. Feenstra, and A. P. Fein, Phys. Rev. Lett. **57**, 2579 (1986). 2.2, 2.2.2

[19] S. D. Kevan and R. H. Gaylord, Phys. Rev. B **38**, 5809 (1987). 2.2

[20] C. J. Adkins and W. A. Philips, J. Phys. C: Sol. State **18**, 1313 (1985). 2.2, 2.2.2

[21] G. Binnig and H. Rohrer, Surf. Sci. **126**, 236 (1983). 2.2

[22] G. Binnig, N. García, H. Rohrer, J. M. Soler, and F. Flores, Phys. Rev. B **30**, 4816 (1984). 2.2

[23] R. Wiesendanger, L. Eng, H. R. Hidber, P. Oelhaffen, L. Rosenthaler, U. Staufer, and H.-J. Güntherodt, Surf. Sci. **189/190**, 24 (1987). 2.2, 2.2.3

[24] R. Wiesendanger, G. Güntherodt, R. J. Gambino, R. Ruf, and H.-J. Güntherodt, Phys. Rev. Lett. **65**, 247 (1990). 2.2

[25] E. Schrödinger, Physical Review **28**, 1049 (1926). 2.2.1

[26] G. Binnig, H. Rohrer, C. Gerber, and E. Weibel, App. Phys. Lett. **40**, 178 (1982). 2.2.1, 2.2.3

[27] G. Binnig, H. Rohrer, C. Gerber, and E. Weibel, Phys. Rev. Lett. **49**, 57 (1982). 2.2.1, 2.2.3

[28] J. Frenkel, Phys. Rev. **36**, 1604 (1930). 2.2.2, 2.2.2, 2.2.3, 2.2.3

[29] J. G. Simmons, J. Appl. Phys. **34**, 1793 (1963). 2.2.2, 2.2.3

[30] J. Bardeen, Phys. Rev. Lett. **6**, 57 (1961). 2.2.2, 2.2.2

[31] J. Tersoff and D. R. Hamann, Phys. Rev. Lett. **50**, 1998 (1983). 2.2.2, 2.2.2, 2.2.3, 2.2.3

[32] A. Selloni, P. Carnevali, E. Tosatti, and C. D. Chen, Phys. Rev. B **31**, 2602 (1985). 2.2.2, 2.2.2

[33] C. J. Chen, *Introduction to Scanning Tunneling Microscopy* (Oxford University Press, 2008). 2.2.2

[34] J. Tersoff and D. R. Hamann, Phys. Rev. B **31**, 805 (1985). 2.2.2, 2.2.3

[35] A. L. Vázquez de Parga, O. S. Hernán, R. Miranda, A. Levy Yeyati, A. Martin-Rodero, and F. Flores, Phys. Rev. Lett. **80**, 357 (1998). 2.2.2, 2.2.2

[36] G. Binnig, K. H. Frank, N. Garcia, B. Reihl, H. Rohrer, F. Salvan, and A. R. Williams, Phys. Rev. Lett. **55**, 991 (1985). 2.2.2

[37] J. Lambre and R. Jaklevic, Phys. Rev. **165**, 821 (1968). 2.2.2

[38] J. Klein, A. Léger, M. Berlin, D. Défourneau, and M. J. L. Sangster, Phys. Rev. B **7**, 2336 (1973). 2.2.2

[39] J. P. Pelz, Phys. Rev. B **43**, 6746 (1991). 2.2.2

[40] L. Bartels, G. Meyer, and K. H. Rieder, App. Phys. Lett. **71**, 213 (1997). 2.2.2

[41] J. R. Hahn and W. Ho, Phys. Rev. Lett. **87**, 196102 (2001). 2.2.2

[42]   P. K. Hansma, Phys. Rep. **30**, 145 (1966). 2.2.2

[43]   B. C. Stipe, M. A. Rezaei, and W. Ho, Science **280**, 1732 (1998). 2.2.2

[44]   L. J. Lauhon and W. Ho, Phys. Rev. B **18**, R8525 (1999). 2.2.2

[45]   C. O. N. Garcia and F. Flores, Phys. Rev. Lett. **50**, 2002 (1983). 2.2.3

[46]   M. Yoshitake and S. Yagyu, Surf. Interface Anal. **36**, 1106 (2004). 2.2.3, 4.4.5.1

[47]   J. F. Jia, K. Inoue, Y. Hasegawa, W. S. Yang, and T. Sakurai, J. Vac. Sci. B. **15**, 1861 (1997). 2.2.3

[48]   S. Hüfner, *Photoelectron Spectroscopy* (Springer Verlag, 1995). 2.3

[49]   S. C. Khandewal and J. L. Roebber, Chem. Phys. Lett. **34**, 355 (1975). 2.3, 2.16, 4.3.6

[50]   R. E. Ballard, *Photoelectron Spectroscopy & Molecular Orbital Theory* (Oxford University Press, 1978). 2.3

[51]   U. Höffer and E. Umbach, J. Elec. Spec. Rel. Phenom. **54/55**, 591 (1990). 2.3, 2.17

[52]   J. W. Gadzuk, Phys. Rev. B **5458**, 14 (1976). 2.3

[53]   J. V. Barth, G. Costantini, and K. Kern, Nature **437**, 671 (2005). 3.1, 3.2.3, 3.3, 4.2.1

[54]   B. G. ans H. Nienhaus, W. H. Weinberg, and E. W. McFarland, Science **294**, 2521 (2001). 3.1

[55]   P. Sautet and M.-L. Bocquet, Phys. Rev. B **53**, 4910 (1996). 3.1

[56]   A. Hauschild, K. Karki, B. C. C. Cowie, M. Rohlfing, F. S. Tautz, and M. Sokolowski, Phys. Rev. Lett **94**, 036106 (2005). 3.1

[57]   G. D. Billing, *Molecule Surface Interactions* (Wiley, 2000). 3.1

[58] H. Ibach, *Physics of Surfaces and Interfaces* (Springer, 2006). 3.1

[59] D. A. King, Crit. Rev. Mater. Sci. **7**, 167 (1978). 3.1

[60] H. Vázquez, R. Oszwaldowski, P. Pou, J. Ortega, R. Pérez, Tejedor, F. Flores, and A. Kahn, Europhys. Lett. p. 802 (2004). 3.1, 3.1.5

[61] M. Eichberger, M. Marschall, J. Reichert, A. Weber-Bargioni, W. Auwärter, R. L. C. Wang, H. J. Kreuzer, Y. Pennec, A. Schiffrin, and J. V. Barth, Nano Lett. **8**, 4608 (2008). 3.1, 3.12, 3.3, 4.1, 4.3.3.2

[62] H. Vázquez, R. Oszwaldowski, P. Pou, J. Ortega, R. Pérez, Tejedor, F. Flores, and A. Kahn, Europhys. Lett. **65**, 802 (2004). 3.1, 3.1.5, 4.4.3

[63] K. Wandelt and J. E. Hulse, J. Chem. Phys. **80**, 1340 (1984). 3.1.1

[64] P. Bagus, K. Hermann, and C. W. Bauschlicher, J. Chem. Phys. **81**, 1966 (1984). 3.1.2

[65] P. S. Bagus, V. Staemmler, and C. Wöll, Phys. Rev. Lett. **89**, 096104 (2002). 3.1.2, 4.4.2

[66] P. C. Rusu, G. Giovannetti, C. Weijtens, R. Coehoorn, and G. Brocks, Phys. Rev. B **81**, 125403 (2010). 3.1.2, 3.1.4, 4.4.2

[67] P. S. Bagus, K. Hermann, and C. Wöll, J. Chem. Phys. **123**, 184109 (2005). 3.1.2, 4.4.1

[68] R. Caputo, B. P. Prascher, V. Staemmler, P. S. Bagus, and C. Wöll, J. Phys. Chem A **111**, 12778 (2007). 3.1.2, 3.1.2

[69] E. Kawabe, H. Yamane, R. Sumii, K. Koizumi, Y. Ouchi, K. Seki, and K. Kanai, Org. Elec. **9**, 783 (2008). 3.1.2

[70] C. Wagner, D. Kasemann, C. Golnik, R. Forker, M. Esslinger, K. Müllen, and T. Fritz, Phys. Rev. B **81**, 035423 (2010). 3.1.2, 4.4.2

[71] S. Z. Sze, *Physics of Semiconductor Devices, 2nd ed.* (Wiley, New York, 1981). 3.1.3

[72] A. Zangwill, *Physics at Surfaces* (Cambridge University Press, 1988). 3.1.3

[73] J. Hwang, E. G. Kim, J. Liu, J. L. Brédas, A. Duggal, and A. Kahn, J. Phys. Chem. **111**, 1378 (2007). 3.1.3

[74] H. Peisert, M. Knupfer, and J. Fink, Appl. Phys. Lett. **81**, 2400 (2002). 3.1.3

[75] C. Rogero, J. I. Pascaul, J. Gómez-Herrero, and A. M. Baró, J. Chem. Phys. **116**, 832 (2002). 3.1.4

[76] J. Bardeen, Phys. Rev. **71**, 717 (1947). 3.1.5

[77] S. Louie and H. Cohen, Phys. Rev. B **13**, 2461 (1976). 3.1.5

[78] C. Tejedor, F. Flores, and E. Louis, J. Phys. C: Solid State Phys. **10**, 2163 (1977). 3.1.5

[79] S. Narioka, H. Ishii, Y. Ouchi, T. Yokoyama, T. Ohta, and K. Seki, J. Phys. Chem. **99**, 1332 (1995). 3.1.5, 4.3.1

[80] D. Yoshimura, H. Ishii, S. Narioka, M. Sei, T. Miyazaki, Y. Ouchi, S. Hasegawa, Y. Harima, K. Yamashita, and K. Seki, Synth. Met. **86**, 2399 (1997). 3.1.5, 4.3.6

[81] S. Guo, D. P. Fogarty, P. M. Nagel, and S. A. Kandel, J. Phys. Chem. B **108**, 14074 (2004). 3.1.5

[82] J. Ziroff, P. Gold, A. Bendounan, F. Forster, and F. Reinert, Surf. Sci. **603**, 354 (2009). 3.1.5

[83] H. Vázquez, Y. J. Dappe, J. Ortega, and F. Flores, Appl. Surf. Sci. **254**, 378 (2007). 3.1.5, 4.4.2

[84] M. Schunack, L. Petersen, A. Kühnle, E. Laegsgaard, I. Stensgaard, I. Johanssen, and F. Besenbacher (????). 3.1.5

[85] Y. Yang and C. Wang, Chem. Soc. Rev. **38**, 2576 (2009). 3.2, 3.2.1

[86] M. Scarselli, P. Castrucci, D. Monti, and M. D. Crescenzi", Surf. Sci. **601**, 5526 (2007). 3.5, 3.2

[87] S. B. Lei, C. Wang, S. X. Yin, H. N. Wang, F. Xi, H. W. Liu, B. Xu, L. J. Wan, and C. L. Bai, J. Phys. Chem. B **105**, 10838 (2001). 3.5, 3.2

[88] H. Margenau, Rev. Mod. Phys. **11**, 1 (1939). 3.2.1

[89] D. M. Cyr, B. Venkataraman, G. W. Flynn, A. Black, and G. M. Whitesides, J. Phys. Chem. **100**, 13747 (1996). 3.7

[90] Y. Ye, W. Sun, Y. Wang, X. Shao, X. Xu, F. Cheng, J. Li, and K. Wu, J. Phys. Chem. C **111**, 10138 (2007). 3.7

[91] M.-C. Blüm, E. Ćavar, M. Pivetta, F. Patthey, and W.-D. Schneider, Angew. Chem. **117**, 5468 (2005). 3.7

[92] L. Grill, M. Dyer, L. Lafferentz, M. Persson, M. V. Peters, and S. Hecht, Nature Nanotechnology **2** (2007). 3.7, 3.2.3, 4.3.6

[93] Y. Li and N. Lin, Phys. Rev. B **84**, 125418 (2011). 3.7

[94] K. Morokuma, Acc. Chem. Res. **10**, 294 (1977). 3.2.2

[95] H. Umeyama and K. Morokuma, J. Am. Chem. Soc. **99**, 1316 (1977). 3.2.2

[96] G. R. Desiraju, Acc. Chem. Res. **29**, 441 (1999). 3.2.2

[97] C. A. Hunter and J. K. M. Sanders, J. Amer. Chem. Soc. **112**, 5225 (1990). 3.2.2, 3.2.2

[98] S. Tsuzuki and A. Fujii, Phys. Chem. Chem. Phys. **10**, 2584 (2008). 3.2.2, 3.2.2

[99] M. Nishio, Phys. Chem. Chem. Phys. (2011), advance Article. 3.2.2, 3.2.2

[100] J. C. Ma and D. A. Dougherty, Chem. Rev. **97**, 1303 (1997). 3.2.2

[101] S. L. James, Chem. Soc. Rev. **32**, 276 (2003). 3.2.3

[102] A. Dmitriev, H. Spillmann, N. Lin, J. V. Barth, and K. Kern, Angew. Chem. Int. Ed. **42**, 2670 (2003). 3.9, 3.2.3

[103] J.-H. Chou, M. E. Kosal, H. S. Nalwa, N. A. Rakow, K. S. Suslick, K. Kadish, K. Smith, and R. Guilard, *Porphyrin Handbook*, vol. 6 (Eds. and Academic Press: New York, 2000). 3.2.3, 4.3.1

[104] K. S. Suslick, P. Bhyrappa, J. H. Chou, M. E. Kosal, S. Nakagaki, D. W. Smithenry, and S. R. Wilson, Acc. Chem. Res **38**, 283 (2005). 3.2.3, 4.3.1

[105] I. Goldberg, Chem. Commun. p. 1243 (2005). 3.2.3, 4.3.1

[106] I. Goldberg, CrystEngComm **10**, 637 (2008). 3.2.3, 4.3.1

[107] J. A. Theobald, N. S. Oxtoby, M. Phillips, N. R. Champness, and P. H. Beton, Nature **424**, 1029 (2003). 3.2.3

[108] J. V. Barth, Annu. Rev. Phys. Chem. **58**, 375 (2007). 3.3

[109] H. Brune, Surf. Sci. Rep. **31**, 121 (1998). 3.3

[110] A. Enders, P. Gambardella, and K. Kern, *The Handbook ofMagnetism and Advanced Magnetic Materials Fundamentals and Theory*, vol. 1 (Chichester: Wiley, 2007). 3.3, 4.2.1

[111] A. Enders, R. Skomski, and J. Honolka, J. Phys: Condens. Matter **22**, 433001 (2010). 3.3, 3.3, 4.2.1

[112] G. S. Bales and D. C. Chrzan, Phys. Rev. B **50**, 6057 (1994). 3.3

[113] T. Mitsui, M. K. rose, E. Fomin, D. F. Ogletree, and M. Salmeron, Science **297**, 1850 (2002). 3.3

[114] C. Stadler, S. Hansen, I. Kröger, C. Kumpf, and E. Umbach, Nat. Phys. **5**, 153 (2009). 4.1, 4.1

[115] N. Knorr, H. Brune, M. Epple, A. Hirstein, M. A. Schneider, and K. Kern, Phys. Rev. B **65**, 115420 (2002). 4.1

[116] G. Rojas, X. Chen, C. Bravo, J.-H. Kim, J.-S. Kim, J. Xiao, P. A. Dowben, Y. Gao, X.-C. Zeng, W. Choe, et al., J. Phys. Chem. C **110**, 9408 (2010). 4.1, 4.2.1, 4.2.3, 4.2.4, 4.4.2, 4.4.2, 4.4.2

[117] F. Buchner, V. Schwald, K. Comanici, H. P. Steinrück, and H. Marbach, Chem. Phys. Chem. **8**, 241 (2007). 4.1, 4.3.6

[118] A. Kretschmann, M.-M. Walz, K. Flechtner, H.-P. Steinrück, and J. M. Gottfried, Chem. Comm. **43**, 568 (2007). 4.1

[119] F. Buchner, K. Flechtner, Y. Bai, E. Zillner, I. Kellner, H.-P. Steinrück, H. Marbach, and J. M. Gottfried, J. Phys. Chem C **112**, 15458 (2008). 4.1, 4.1, 4.2.1, 4.3.3.1, 4.3.6, 4.4.2

[120] F. Buchner, K.-G. Warnick, T. Wölfle, A. Görling, H.-P. Steinrück, W. Hieringer, and H. Marbach, J. Phys. Chem. C **113**, 16450 (2009). 4.1, 4.1, 4.1, 4.3.1, 4.3.5, 4.4.2

[121] A. Weber-Bargioni, J. reichert, A. P. Seitsonen, W. Auwärter, A. Schiffrin, and J. V. Barth, J. Phys. Chem. C. **112**, 3453 (2008). 4.1, 4.3, 4.1

[122] K. Fletchner, A. Kretschmann, H. P. Steinrück, and J. M. Gottfried, J. Am. Chem. Soc. **129**, 12110 (2007). 4.1, 4.1, 4.3.1

[123] F. Buchner, K. Seufert, W. Auwärter, D. Heim, J.-V. Barth, K. Fletchner, J. M. Gottfried, H.-P. Steinrück, and H. Marbach, ACS Nano **3**, 1789 (2009). 4.1

[124] T. Lukasczyk, , K. flechtner, L. R. Merte, N. Jux, F. Maier, J. M. Gottfried, and H.-P. Steinrück, J. Phys. Chem. C **111**, 3090 (2007). 4.1, 4.1, 4.3.6, 4.4.1, 4.4.2

[125] W. Auwärter, A. Weber-Bargioni, A. Riemann, A. Schiffrin, O. Gröning, R. Fasel, and J. V. Barth, J. Chem. Phys. **124**, 194708 (2006). 4.1, 4.3, 4.2.1, 4.3.1, 4.3.5, 4.4.2

[126] W. Auwärter, A. Weber-Bargioni, S. Brink, A. Riemann, A. Schiffrin, M. Ruben, and J. V. Barth, Chem. Phys. Chem. **8**, 250 (2007). 4.1, 4.3.3.1, 4.3.5, 4.3.6, 4.4.2

[127] T. Yokoyama, T. Kamikado, S. Yokoyama, and S. Mashiko, J. Chem. Phys. **121**, 11993 (2004). 4.1

[128] K. Comanici, F. Buchner, K. Flechtner, T. Lukasczyk, J. M. Gottfried, H.-P. Steinrück, and H. Marbach, Langmuir **24**, 1897 (2008). 4.1, 4.2.1, 4.2.3, 4.4.2, 4.4.2

[129] F. Buchner, E. Zillner, M. Röckert, S. Gläßel, H.-P. Steinrück, and H. Marbach, Chem. Eur. J. (2011). 4.1, 4.1

[130] L. Scudiero, D. E. Barlow, U. Mazur, and K. W. Hipps, J. Am. Chem. Soc. **123**, 4073 (2001). 4.1

[131] L. G. Teugels, L. G. Avila-Bront, and S. J. Sibener, J. Phys. Chem. C **115**, 2826 (2011). 4.1, 4.3, 4.2.1, 4.2.3

[132] K. W. Hipps, L. Scudiero, D. E. Barlow, and J. Cooke, M. P., J. Am. Chem. Soc. **124**, 2126 (2002). 4.1, 4.1, 4.3.6

[133] L. Scudiero, D. E. Barlow, and K. W. Hipps, J. Phys. Chem. B **104**, 11899 (2000). 4.1, 4.1, 4.3.6

[134] F. Klappenberger, A. Weber-Bargioni, W. Auwärter, M. Marschall, A. Schiffrin, and J. V. Barth, J. Chem. Phys. **129**, 214702 (2008). 4.3, 4.1, 4.3.5

[135] L. A. Zotti, G. Teobaldi, W. A. Hofer, W. Auwärter, A. Weber-Bargioni, and J. V. Barth, Surf. Sci. **601**, 2409 (2007). 4.1, 4.3.6

[136] T. Kamikado, T. Sekiguchi, S. Yokoyama, Y. Wakayama, and S. Mashiko, Thin Solid Films **499**, 329 (2006). 4.4, 4.1, 4.3.1, 4.3.3.1

[137] Y. Bai, M. Sekita, M. Schmid, T. Bischof, H.-P. Steinrück, and J. M. Gottfried, Phys. Chem. Chem. Phys. **12**, 4336 (2010). 4.1

[138] M. Zinke-Allmang, L. C. Feldman, and M. H. Grabow, Surf. Sci. Rep. **16**, 377 (1992). 4.2.1, 4.2.4

[139] H. Brune, *Metal Clusters at Surfaces* (Springer, Berlin, 2000), chap. Growth of Metal Clusters at Surfaces, pp. 67 – 105. 4.2.1, 4.2.4

[140] W. Auwärter, F. Klappenberger, A. Weber-Bargioni, A. Schiffrin, T. Strunskus, C. Wöll, Y. Pennec, A. Riemann, and J. V. Barth, J. Am. Chem. Soc. **129**, 11279 (2007). 4.2.1, 4.3.6

[141] G. Rojas, X. Chen, D. Kunkel, J. Xiao, P. A. Dowben, S. Simpson, E. Zurek, and A. Enders (2011), arXiv:1107.0306. 4.2.1

[142] T. A. Widden and L. M. Sander, Phys. Rev. Lett. **47**, 1400 (1981). 4.2.4

[143] J. Yang, T. Wang, H. Wang, F. Zhu, G. Li, and D. Yan, J. Phys. Chem. B **112**, 7816 (2008). 4.2.4

[144] R. Q. Hwang, J. Schröder, C. Gunther, and R. J. Behm, Phys. Rev. Lett. **67**, 3279 (1991). 4.2.4

[145] H. Brune, H. Roder, C. Boragno, and K. Kern, Phys. Rev. Lett. **73**, 1955 (1994). 4.2.4, 4.2.4

[146] M. Zinke-Allmang, L. C. Feldman, and S. Nakahara, Appl. Phys. Lett. **28**, 975 (1987). 4.2.4, 4.2.4

[147] J. G. McLean, B. Krishnamachari, D. R. Peale, E. Chason, P. Sethna, and B. H. Cooper, Phys. Rev. B **55**, 1811 (1997). 4.2.4

[148] W. W. Pai, A. K. Swan, Z. Zhang, and J. F. Wendelken, Phys. Rev. Lett. **79**, 3210 (1997). 4.2.4

[149] S. Kodambaka, V. Petrova, A. Vailionis, P. Desjardins, D. G. Cahill, I. Petrov, and J. E. Greene, Thin Solid Films **392**, 164 (2001). 4.2.4

[150] S. Kodambaka, V. Petrova, S. Khare, D. Gall, A. Rockett, I. Petrov, and J. E. Greene, Phys. Rev. Lett. **89**, 176102 (2002). 4.2.4

[151] G. Ehrlich, Surf. Sci. **246**, 1 (1991). 4.2.4

[152] G. W. Jones, J. M. Marcano, J. K. Nrskov, and J. A. Venables, Phys. Rev. Lett. **65**, 3317 (1990). 4.2.4

[153] C. L. Chen and T. T. Tsong, Phys. Rev. Lett. **66**, 1610 (1991). 4.2.4

[154] K. Kyuno, A. Gölzhäuser, and G. Ehrlich, Surf. Sci. **397**, 191 (1998). 4.2.4

[155] H. Brune, G. S. Bales, J. Jacobsen, C. Boragno, , and K. Kern, Phys. Rev. B **60**, 5991 (1999). 4.2.4

[156] H. Marchetto, U. Groh, T. Schmidt, R. Fink, H.-J. Freund, and E. Umbach, Chem. Phys. **325**, 178 (2006). 4.2.4

[157] J. V. Barth, H. Brune, B. Fischer, J. Weckesser, and K. Kern, Phys. Rev. Lett. **84**, 1732 (1994). 4.2.4, 4.2.4

[158] G. S. Kottas, L. I. Clarke, D. Horinek, and J. Michl, Chemical Reviews **105**, 1281 (2005). 4.3.1

[159] D. M. Vriezema, M. C. Aragones, J. Elemans, J. Cornelissen, A. E. Rowan, and R. J. M. Nolte, Chemical Reviews **105**, 1445 (2005). 4.3.1

[160] H. L. Anderson, Chem. Commun. p. 2323 (1999). 4.3.1

[161] T. Suzuki, M. Kurahashi, and Y. Y. Ju, X., J. Phys. Chem. B **106**, 11553 (2002). 4.3.1

[162] I. Mochida, K. Suetsugu, H. Fujitsu, and K. Takeshita, J. Phys Chem. **87**, 1524 (1983). 4.3.1

[163] E. Brulè and X. R. d. Miguel, Org. Biomol. Chem. **4**, 599 (2006). 4.3.1

[164] E. C. Zampronio, M. Gotardo, M. D. Assis, and H. P. Oliveira, Catal. Lett. **104**, 53 (2005). 4.3.1

[165] C. M. Drain, I. Goldberg, I. Sylvain, and A. Falber, **245**, 55 (2005). 4.3.1

[166] L. D. DeVries and W. J. Choe, Chem. Crystallogr. **39**, 229 (2009). 4.3.1

[167] Y. Zhou, B. Wang, and H. J. G. Zhu, M., Chem. Phys. Lett. **403**, 140 (2005). 4.3.1

[168] C. M. Drain, F. Nifiatis, A. Vasenko, and J. D. Batteas, Angew. Chem. Int. Ed. **42**, 2670 (2003). 4.3.1

[169] C. M. Drain, J. D. Batteas, G. w. Flynn, T. Milic, N. Chi, D. G. Yablon, and H. Sommers, PNAs **99**, 6498 (2002). 4.3.1

[170] J. Zhang, C. Sessi, C. H. Michaelis, I. Brihuega, J. Honolka, K. Kern, R. Skomski, X. Chen, G. Rojas, and A. Enders, Phys. Rev. B. **78**, 165430 (2008). 4.3.1

[171] N. T. M. Hai, B. Gasparovic, K. Wandelt, and P. Brökmann, Surf. Sci. **601**, 2597 (2007). 4.3.1

[172] S. Yoshimoto, N. Yokoo, T. Fukuda, N. Kobayashi, and K. Itaya, Chem. Commun. p. 500 (2006). 4.3.1, 4.3.6

[173] T. Yokoyama, S. Yokoyama, T. Kamikado, and S. Mashiko, J. Chem. Phys. **115**, 3814 (2001). 4.3.1

[174] L. Ramoino, M. von Arx, S. Schintke, A. Baratoff, H.-J. Güntherodt, and T. Jung, Chem. Phys. Lett. **417**, 22 (2006). 4.3.1

[175] H. Spillman, A. Kiebele, M. Stöhr, T. A. Jung, d. Bonifazi, and D. F. Cheng, F., Adv. Mater. **18**, 275 (2006). 4.3.1

[176] W. Deng, O. T. Y. S. Fujita, D., K. Kamikado, and S. Mashiko, J. Chem. Phys. **117**, 4995 (2002). 4.3.1

[177] D. Bonifazi, A. Kiebele, M. Stöhr, F. Cheng, T. Jung, F. Diederich, and H. Spillmann, Adv. Func. Mater. **17**, 1051 (2007). 4.3.1

[178] J. Brede, M. Linares, S. Kuck, J. Schwöbel1, A. Scarfato, S.-H. Chang, G. Hoffmann, R. Wiesendanger, R. Lensen, P. H. J. Kouwer, et al., Nanotechnology **20**, 275602 (2009). 4.3.1, 4.3.3.1, 4.3.6, 4.3.6, 4.4.2

[179] J. Zhang, D. McIlroy, P. Dowben, H. Zeng, G. Vidali, D. Heskett, and M. J. Onellion, Phys. Cond. Matt. **7**, 7185 (1995). 4.3.2

[180] F. A. Hamprecht, A. Cohen, D. J. Tozer, and N. C. Handy, J. Chem. Phys. **109**, 6264 (1998). 4.3.2

[181] A. D. Boese, N. L. Doltsinis, N. Handy, , and M. Sprik, J. Chem. Phys. **112**, 1670 (2000). 4.3.2

[182] A. Boese, , and N. Handy, J.Chem. Phys. **114**, 5497 (2001). 4.3.2

[183] B. Delley, J. Chem. Phys. **92**, 508 (1990). 4.3.2

[184] B. Delley, J. Chem. Phys. **113**, 7756 (2000). 4.3.2

[185] S. Silvers and A. Tulinsky, J. Am. Chem. Soc. **89**, 33311 (1967). 4.3.3.1

[186] M. J. Hamor and H. T. A., J. Am. Chem. Soc. **86**, 1938 (1964). 4.3.3.1

[187] K. Kano, K. Fukuda, H. Wakami, and R. Nishiyabu, J. Am. Chem. Soc. **122**, 7494 (2000). 4.3.3.1

[188] J. Brede, M. Linares, R. Lensen, A. E. Rowan, M. Funk, M. Bröring, G. Hoffmann, and R. Wiesendanger, J. Vac. Sci. Technol. B **29**, 799 (2009). 4.3.3.2, 4.3.6

[189] *Spartan 8.0*, URL http://www.wavefun.com. 4.3.4

[190] B. Sridevi, S. Jeyaprakash Narayanan, A. Srinivasan, M. V. Reddy, and T. K. Chandrashekar, J. Porphyrins Phthalocyanines **2**, 69 (1998). 4.3.4

[191] J. F. Dobson, K. McLennan, A. Rubio, J. Wang, T. Gould, H. M. Le, and B. P. Dinte, Aust. J. Chem. **54**, 513 (2001). 4.3.5

[192] M. Pitoǒá, P. Neogrády, J. Rezáč, P. Jurečka, M. Urban, and P. Hobza, J. Chem. Theo. Comp. **4**, 1829 (2008). 4.3.5

[193] T. Wölfle, A. Görling, and W. Hieringer, Phys. Chem. Chem. Phys. **10**, 5739 (2008). 4.3.5

[194] H. Marchetto, U. Groh, T. Schmidt, R. Fink, H. J. Freund, and E. Umbach, Chem. Phys. **325**, 178 (2006). 4.3.5

[195] Y. Zidon, Y. Shapira, H. Shaim, and T. Dittrich, Appl. Surf. Sci. **254**, 3255 (2008). 4.3.6

[196] W. Deng and K. W. Hipp, J. Phys. Chem. B **107**, 10736 (2003). 4.3.6

[197] K. Suto, S. Yoshimoto, and K. Itaya, Langmuir **22**, 10766 (2006). 4.3.6

[198] J. Repp, G. Meyer, F. E. Olsson, and M. Persson, Science **305**, 493 (2004). 4.3.6

[199] D. Wegner, R. Yamachika, Y. Wang, V. W. Brar, B. M. Bartlett, J. R. Long, and M. F. Crommie, Nano Lett. **8**, 131 (2008). 4.3.6, 4.4.2

[200] F. E. Olsson, M. Persson, N. Lorente, L. J. Lauhon, and W. Ho, J. Phys. Chem. B **106**, 8161 (2002). 4.3.6

[201] I. Fernandez-Torrente, S. Monturet, K. J. Franke, J. Fraxedas, N. Lorent, and J. I. Pascual, Phys. Rev. Lett. **99**, 176103 (2007). 4.3.6, 4.4.2

[202] D. E. Barlow, L. Scudiero, and K. Hipps, Langmuir **20**, 4413 (2004). 4.3.6

[203] X.-L. Zhang, L.-G. Chen, P. Lv, H.-Y. Gao, S.-J. Wei, Z.-C. Dong, and J. G. Hou, Appl. Phys. Lett. **92**, 223118 (2008). 4.3.6

[204] Z. C. Dong, X. L. Zhang, H. Y. Gao, C. Zhang, L. G. Chen, R. Zhang, X. Tao, Y. Zhang, J. L. Yang, and J. G. Hou, Nature Photonics **4**, 50 (2009). 4.3.6

[205] H. Peisert, T. Schwieger, M. Knupfer, M. S. Golden, and J. Fink, J. Appl. Phys **88**, 1535 (2000). 4.3.6

[206] B. Hammer and J. K. Noerskov, Nature **376**, 238 (1999). 4.4.1, 4.4.2, 4.4.2

[207] R. Temirov, S. Soubatch, A. Luican, and F. Tautz, Nature **444**, 350 (2006). 4.4.1

[208] L. Romaner, G. Heimel, J. L. Brédas, A. Gerlach, and F. Schreiber, Phys. Rev. Lett. **11**, 256801 (2007). 4.4.1

[209] S. Bedwani, D. Wegner, M. F. Crommie, and A. Rochefort, Phys. Rev. Lett. **99**, 216105 (2008). 4.4.1

[210] W. Shockley, Physical Review **56**, 317 (1939). 4.4.1

[211] R. Thorpe, R. A. Bartynski, J. Rochford, S. Rangan, S. Katalinic, and E. Galoppini, J. Phys. Chem. C **114**, 1139 (2010). 4.4.2

[212] M. S. Liao and S. Scheiner, J. Chem. Phys. **117**, 205 (2002). 4.4.2

[213] S. D. Kevan, Phys. Rev. Lett. **50**, 526 (1983). 4.4.2

[214] O. Jeandupeux, L. Bürgi, A. Hirstein, H. Brune, and K. Kern, Phys. Rev. B **59**, 154926 (1999). 4.4.2

[215] W. Auwärter, K. Sufert, F. Klappenbeger, J. Reichert, A. Weber-Bargioni, A. Verdini, D. Cvetko, M. Dell' Angela, L. Floreano, A. Cossaro, et al., Phys. Rev. B **81**, 245403 (2010). 4.4.2

[216] Z. C. Dong, X. L. Zhang, H. Y. Gao, Y. Luo, C. Zhang, L. G. Chen, R. Zhang, X. Tao, Y. Zhang, J. L. Yang, et al., Nature Photonics **4**, 50 (2010). 4.4.2

[217] G. te Velde, F. M. Bickelhaupt, E. J. Baereneds, C. Fonseca Guerra, S. J. A. van Gisbergen, J. G. Snijders, and T. Ziegler, J. Comput. Chem. **22**, 931 (2001). 4.4.4

[218] E. J. Baerends, J. Autschbach, A. Bérces, F. M. Bickelhaupt, C. Bo, P. M. Boerrigter, L. Cavallo, D. P. Chong, L. Deng, and R. M. D. et al., *Theoretical chemistry* (2006), URL http://www.scm.com. 4.4.4

[219] J. P. Perdew, K. Burke, and Y. Wang, Phys. Rev. B **54**, 16533 (1996). 4.4.4

[220] S. Grimme, J. Antony, S. Ehrlich, and H. Krieg, J. Chem. Phys. **132**, 154104 (2010). 4.4.4